Politecnico di Milano
Department of Electronics, Information and Bioengineering
Doctoral Program in Bioengineering

Enhancing Human Robot Interaction in Teleoperated Tasks

Doctoral Dissertation of:
Jacopo Buzzi
10306537

Supervisors:
Elena De Momi Ph.D.
Prof. Giancarlo Ferrigno

Tutor:
Prof. Linda Pattini

The Chair of the Doctoral Program:
Prof. Andrea Aliverti

2018 - XXX Cycle

“It’s a dangerous business, Frodo, going out your door. You step onto the road, and if you don’t keep your feet, there’s no knowing where you might be swept off to”

[Bilbo Baggings - *The Fellowship of the Ring, Chapter 3*]

Politecnico di Milano
Department of Electronics, Information and Bioengineering
Doctoral Program in Bioengineering

Abstract

Enhancing Human Robot Interaction in Teleoperated Tasks

by Jacopo BUZZI

Human-robot interaction (HRI) has gained growing importance over the last decades, becoming a leading topic in many research field. Robots are employed in many aspects of everyday life, from assembly lines to therapeutic tools in rehabilitation and Autistic Spectrum Disorders treatments, as well as in surgery. When Human and Robots physically interact (Physical Human-robot Interaction - pHRI), a non-verbal, implicit, form of communication takes place through the exchange of forces and torques, sometimes mediated and modified by the environment and the common shared task.

In recent years, among the other applications of pHRI, teleoperation has seen a remarkable growth, thanks to the substantial advantages that it offers in dealing with hazardous or disadvantageous workspaces. In teleoperation, users control a master device, a robotic device whose movements are transmitted to a remote slave robot, which directly manipulates the task environment. Therefore, in this type of pHRI, teleoperators must successfully control the master device, whose dynamic and kinematic characteristics should allow for the most intuitive, transparent and stable interaction. Multiple studies focused on the master devices' mechanical optimization in order to obtain high dexterity (which allows teleoperators to freely manipulate the master device without being limited), large workspaces and high positional and rotational accuracy.

Although successful, these works didn't take into consideration the high kinematic and dynamic variability that characterize human motor control: while performing a task, users modify the arm's joint configuration as well as muscular activations to increase task performance and achieve high stability against internal and external noise. Therefore, master devices should not only allow users to preserve these motor strategies, but also they should adapt to the changes in the arm's characteristics in order to offer an advantageous interaction dynamic.

The overall goal of this thesis is to explore those aspects of the motor control that influence pHRI in teleoperation, in order to obtain insights on which are the kinematic and dynamic characteristics that allow for the most profitable interaction, as well proposing controllers able to adapt to the changes in the arm's dynamics. In particular, the research has been focused on the following topics:

(I) *Arm's joint variability analysis during virtual teleoperation.* Using the Uncontrolled Manifold Analysis, the effects of different master device's designs as well as different tasks constraints over teleoperator capability in exploiting arm redundancy is investigated. The tasks, that were developed in a virtual environment, included the control of position only or position-orientation of a tool. The results show that users were capable of exploiting higher levels of arm redundancy when dealing with the tool orientation. Moreover, the different master designs didn't significantly affect users' redundancy exploitation capabilities or performances.

(II) *Analysis of hand impedance during teleoperation and free-hand task execution.* A comparison of arm end-point stiffness modulation while teleoperating with two master devices and in free-hand is presented. A suturing mimicking task was physically realized and developed within a virtual environment. User arm's kinematic was acquired using optoelectronic cameras and electromagnetic markers and used with a musculoskeletal model to obtain an estimation of the users' arm end-point stiffness. Results show a significant difference between master devices and the free-hand as well as a directional modulation of arm stiffness during task execution.

Through the use of an Electromyography informed inverse dynamic toolbox, the arm end-point stiffness estimation is refined, ad it's used to evaluate the dynamic differences in the execution of two tasks with different constraints with two master devices. The results show that the arm impedance modulation is affected by the task characteristics and by the hand speed and acceleration. Although mechanically different, the two master devices allow for similar stiffness modulations, proving the arm capabilities in coping with different dynamic systems while maintaining consistent results.

(III) *Development of a biomimetic adaptive impedance controller.* Based on the estimation of the arm end-point stiffness modulation during the execution of a virtual teleoperation targeting task, a biomimetic adaptive impedance controller for the robotic master device is developed. The master device's damping coefficient matrix is adapted to the arm stiffness changes in magnitude and direction while approaching the target. The results show that users' performances in terms of positional accuracy increased under the effect of the biomimetic variable damping field.

The overall results presented demonstrate the potential of studying the effects induced by the interaction with a robotic master device on the motor strategies; moreover, the results showed the benefits of achieving a higher level of mutual awareness between human and robot's by sharing users' arm stiffness within the teleoepration framework. In the future perspective, this work represents a step forward in the direction of actively including human factors within the robot control paradigm, which will allow master device's to become a natural extension of the users' arm.

Contents

1 **Introduction** **1**
- 1.1 Human-Robot Interaction 1
- 1.2 HRI applications 1
- 1.3 Human-Robot interactive communication 4
- 1.4 Physical Interaction control in HRI 6
- 1.5 Thesis motivation 7
- 1.6 Aim of the thesis 8
- 1.7 Outline 9

2 **UCM Analysis in planar position and orientation tele-manipulation** **11**
- 2.1 Introduction 11
- 2.2 Methods 14
  - 2.2.1 Tasks design 14
  - 2.2.2 Master devices 16
  - 2.2.3 Acquisition framework 17
  - 2.2.4 Experimental protocol 17
  - 2.2.5 Joint angle estimation 17
  - 2.2.6 Uncontrolled Manifold Analysis 19
  - 2.2.7 Jacobian estimation 21
  - 2.2.8 Data Analysis 22
    - Redundancy Exploitation 22
    - Error metrics 23
- 2.3 Results 24
  - 2.3.1 Redundancy Exploitation 24
  - 2.3.2 Error metrics 26
- 2.4 Discussion 27
  - 2.4.1 Redundancy Exploitation 29
  - 2.4.2 Error metrics 31
  - 2.4.3 Limitations and future work 32
- 2.5 Conclusion 33

3 **Hand impedance in teleoperation and free-hand task** **35**
- 3.1 Introduction 35
- 3.2 Materials and methods 37
  - 3.2.1 Task 37

3.2.2 Experimental protocol . . . 39
3.2.3 Master devices . . . 40
3.2.4 Acquisition architecture . . . 40
3.2.5 The musculoskeletal model . . . 41
3.2.6 Stiffness computation . . . 42
3.2.7 Results analysis . . . 43
Error . . . 43
Stiffness ellipsoids - Main axis length . . . 44
Stiffness ellipsoids - Angular displacement . . . 45
3.3 Results . . . 45
3.3.1 Error . . . 45
3.3.2 Stiffness Ellipsoids - Main axis length . . . 45
3.3.3 Stiffness Ellipsoids - Angular displacement . . . 46
3.4 Discussion . . . 47
3.5 Future developments . . . 49
3.6 Acknowledgements . . . 49

4 Evaluation of arm stiffness during virtual teleoperation 51
4.1 Introduction . . . 51
4.2 Materials and methods . . . 53
4.2.1 Tasks design . . . 53
4.2.2 Experimental setup . . . 55
Master devices . . . 55
Acquisition framework . . . 56
Experimental Protocol . . . 57
4.2.3 Stiffness computation . . . 58
Kinematic Analysis . . . 58
Dynamic Analysis . . . 59
EMG-informed torque estimation . . . 59
Stiffness computation . . . 60
4.2.4 Metrics and statistical analysis . . . 61
Analysis performed and hypothesis tested . . . 62
4.3 Results . . . 63
4.3.1 Maximal Stiffness through the trajectory . . . 63
4.3.2 Stiffness against hand speed and acceleration . . . 67
4.3.3 Distance metric . . . 69
4.4 Discussion . . . 69
4.4.1 Future developments . . . 71

5 Biomimetic adaptive impedance control in physical Human Robot Interaction 73
5.1 Introduction . . . 73
5.2 Materials and Methods . . . 75

5.2.1 Task design . . . 76
5.2.2 Master Device . . . 76
5.2.3 Stiffness Estimation . . . 77
5.2.4 Biomimetic adaptive impedance controller . . . 77
Enhancing damping field . . . 79
Isotropic damping field . . . 79
5.2.5 Visco-elastic Plane . . . 80
5.2.6 Experimental protocol . . . 81
Arm stiffness estimation . . . 81
Variable impedance controller . . . 81
5.2.7 Performance Indexes . . . 81
5.2.8 Results analysis . . . 82
Stiffness Estimation . . . 82
Variable impedance control performances . . . 83
5.3 Results . . . 83
5.3.1 Stiffness Estimation . . . 83
5.3.2 Variable impedance control performances . . . 85
5.4 Discussion . . . 86
5.5 Conclusions . . . 88

6 Conclusions **89**
6.1 Thesis Contributions . . . 90
6.2 Future Perspective . . . 92

Bibliography **95**

List of Figures

1.1 Different applications of HRI: **A.** KuKa Light Weight Robot cooperating with a human in an assembly task **B.** User catching a ball teleoperating a Light Weight Robot under tele-impedance control **C.** Robovie-IV from ATR IRC Laboratories, carrying a bag and interacting with humans **D.** Surgeon performing teleoperation using the Da Vinci single-site surgical robot from Intuitive Surgical, Sunnyvale, CA. 4
1.2 Motor control paradigms in teleoperation. The interaction between user and task is mediated by the master device, whose kinematic (see Chapter 2) and dynamic (see Chapters 3 and 4) characteristics influence the motor strategies adapted to perform tasks (see Chapter 5). . . 9

2.1 The two virtual tasks that were developed. In T_{2D} (A) users were required to follow an eight-shaped path controlling a virtual stylus tip. In T_{3D} (B), users were also required to control the tool's orientation throughout the path 15
2.2 **A.** The experimental setup: user performs the tasks while looking at a flat screen (1) and teleoperating with the hybrid parallel/serial link master device (Sigma - 2) or using the serial link master device (Omni - 3). The thorax movements are recorded using an optic camera (4) with three retroreflecting markers (5) while the arm kinematics is acquired with an electromagnetic tracker (6) and 6DoFs markers (7). The shoulder reference frame (8) is grossly aligned with the VR one (9). **B.** Task space dimensions for T_{2D} and T_{3D}. **C.** The OpenSim model used for the inverse kinematics. In blue the seven degrees of freedom (1, 2 … 7) and in red the virtual markers set-up: Left and Right Acromium (LA, RA), Breast Bone (BB) for the thorax, Lateral and Medial Elbow (LE, ME) for the arm, Lateral and Medial Wrist for the forearm (LW, MW), Lateral and Medial Hand (LH, MH) for the hand orientation. In the magnifying box: T_{2D} and T_{3D} task spaces. 18
2.3 *(HP1)* A. The curvature regions in the two tasks. B. Mean positional R_v and standard deviations through the trajectories while teleoperating with Sigma (in red) and Omni (in blue) 24

2.4 *(HP2 & HP3)* R_v distribution among the experiments: T_{2D} and T_{3D} performed with the hybrid parallel/serial link robot and with the serial link one, computed using the analytical Jacobian ($J_{2D,A}$) and with the Least Squares Jacobian ($J_{2D,LSQ}$). The boxplots represent median values, first and third quartiles and minimal and maximal values. The statistical differences are depicted using lines and stars. 26
2.5 *(HP3)* Differences in the R_v distribution among users between different master devices and task space variables considered. In red the results obtained considering the positional only task variables (J_{2D}) and in green when also the tool rotation is accounted (J_{3D}). 27
2.6 Error metrics (d and ψ) mean and standard deviations for T_{2D} and T_{3D}. In red the hybrid parallel-serial link master device (Sigma) and in blue the serial link master device (Omni). 28

3.1 The complete setup: (a)The virtual reality trajectory. (b) The free-hand task: 1. Base 2. Metal wire trajectory 3. EMT Pointer 4. 3D Printed ring end-effector (c) The serial link master device (SL). (d) The parallel link master device (PL). 38
3.2 The acquisition framework: each hatched box represents a ROS component that is responsible of streaming or monitoring a specific kind of signal. The arrows depict the ROS topic connecting each component and the acquisition frequencies are reported into the overlying circles 39
3.3 Markers setup: gray points represent EMT markers position, i.e. arm, forearm and hand; black points are the virtual markers created during the calibration phase during which the EMT pointer tool was used to touch two recognizable bony landmarks on each arm segment, while a custom ROS component acquired the transformation that mapped the touched point in the EMT marker reference frame of the corresponding segment (${}^{Real}\mathbf{T}_{Virt}$). Arm and forearm sensors were connected to lateral and medial repere point of elbow and wrist respectively; the hand virtual sensors were placed on the index and little finger's knuckle. 42
3.4 The computed ellipsoid (in blue) is overlapped to the muscoloskeletal model at a specific point on the trajectory (in red). (a) The main axis dimension K_{max} and its angle with the tangent to the trajectory φ are monitored through the different users task repetitions. (b) The six points along the trajectory 44
3.5 The error metric in PL, SL, and FH are reported as 25^{th} and 75^{th} percentiles and median values. The statistical difference between the control modalities is reported using horizontal lines. Three stars indicate $p < 0.001$ 45

3.6 The maximal hand stiffness in the six points of the trajectory for the parallel link robot, for the serial link robot and for free-hand. Boxes indicate the 25^{th} and 75^{th} percentiles, vertical dashed lines indicate the maximal values and the horizontal dashed lines represent the median values of the three populations. The horizontal lines at the top of the graph describe the statistical difference between the control modalities when all the six points are considered together, as in Table I. One star correspond to $p < 0.05$, two stars to $p < 0.01$ 46
3.7 The angle between the maximal hand stiffness direction and the tangent to the desired trajectory in the six points for the three control modalities. The points represent the median values, while the vertical lines represent the 25^{th} and 75^{th} percentiles. The dotted line represents the second order polynomial regression, with the corresponding R^2 values associated. 47

4.1 The figure represents the two trajectories designed. Task 1. A line following task shaped as an half cloverleaf (HC). The aim to to finely follow the trajectory starting from the green dot and moving anticlockwise. Task 2. In the task, shaped as a thicker half cloverleaf (SFHC), the users have to orient the tool's cylindrical end-effector along the trajectory (2.1 to 2.4) 54
4.2 Experimental setup: the user performs the task looking at a monitor laid flat on a table (1) while teleoperating using either a parallel link haptic device PL (2) or a serial link haptic device SL (3) while the thorax and arm kinematic are acquired with an optical camera (4) and reflective markers (5) and with electromagnetic tracker (6) and markers (7). The EMG activation is also acquired with bipolar electrodes (8).The virtual reference frame (9) and the shoulder reference frame (10) are grossly aligned in the setup phase. 55
4.3 Surface electromyography electrodes placement: 1-2-3 for the anterior, lateral and posterior deltoids, 4-5 for the long and lateral trisceps brachii, 6 for the biceps, 7-8-9 for the brachioradialis, flexor carpi radialis and ulnaris respectively and 10 for extensor digitorum 57
4.4 Maximal stiffness (K_{max}) distribution in the four experiments for the four increasing levels of curvature. The results are presented using boxplot indicating median, first and third quartile, minimal and maximal values. Horizontal lines over the boxes indicate statistical difference while the number of stars indicate different levels of significance (** = p<0.01) 64

4.5 Variance of maximal stiffness (K_{max}) in the four experiments for the four increasing levels of curvature. Horizontal lines over the boxes indicate statistical difference while the number of stars indicate different levels of significance (** = $p<0.01$) 65

4.6 Maximal stiffness K_{max} from all the users and trials in each point along the trajectory is presented: the height and color of each column indicates the corresponding point median. To account for the difference in terms of median values from experiments PL1 and SL1 compared with PL2 and SL2, a custom color-map was designed. K_{max} values from 0 to 4 N/m are plotted with colors from light blue to purple, while K_{max} values from 4 to 40 N/m range from a dark red to bright yellow. 65

4.7 Stiffness with respect to curvature analysis. 1. Normalized curvature through the trajectory. 2. Definition of the four regions of normalized curvature. 3. Box-plot comparing the maximal stiffness value K_{max} for the PL master device, on the left, and for the SL master device on the right. The boxes represent the first and third quartile, while the whiskers represent the minimal and maximal values. 66

4.8 Distribution of speed (in blue, solid line) and acceleration (in red, dashed line) in the four experiments. Horizontal lines over the boxes indicate statistical difference while the number of stars indicate different levels of significance (*** = $p<0.0001$) 67

4.9 End-point stiffness distribution with respect to four increasing levels of hand speed (in blue) and acceleration (red). The levels of speed and acceleration correspond to each experiment distribution quartiles. . . . 68

4.10 Wrist flexion-extension patterns during the execution of HC and SFHC for a single user: in gray the single normalized task repetitions, red and blue lines represent the mean joint angle signal for HC and SFHC, while red and blue areas represent the standard deviation interval. . . 70

5.1 Starting from the central Home, the user has to reach every single target point T_i (arranged along the sides of a square), positioning the end effector point ($\mathbf{P}_{VE}$) as precisely as possible in the center of the target for *1s* and come back to the Home. Circular targets with a radius $r = 50$mm are are distributed on a square with semi-side $L_T = 300$mm. The virtual reference frame (x-y) is centered on the Home position. 76

5.2 Schematic of the biomimetic adaptive impedance controller: using joint angles (ϑ) and EMG signals combined with an EMG informed inverse dynamic algorithm, users' stiffness is estimated. Mean stiffness modulation ($\bar{K}_{max}$) and orientation ($\hat{\theta}$, with respect to the virtual plane x axis) are used to generate the adaptive damping modulation (c_x, c_y). The master device's speeds on the x-y plane ($\dot{P}_{x,MD}$,$\dot{P}_{y,MD}$) are used to compute the corresponding damping forces ($F_{x,C}$,$F_{y,C}$). Similarly, a viscoelastic virtual plane produces forces along the Z axis ($F_{z,MD}$) obtained from the sum of the elastic (k_z) and damping (c_z components) 78

5.3 **A**. c_{max} and c_{min} as function of d. **B**. Subject posture during task execution. The main axis of the stiffness ellipse (red dash-dot line), corresponds to the shoulder-hand direction. In green: the *Enhancing* damping coefficient field, in blue, the *Isotropic* one. 80

5.4 Mean stiffness modulation profile and stiffness ellipsoid orientation. **A.** the solid black line represents the mean stiffness $\bar{K}_{max}$(d) over the different targets, while the dashed black lines represent the first and third quantiles. The solid red line shows the linear regression, whose significance (p) and ρ values are also reported. **B.** The main axis of the mean stiffness ellipsoid is represented with a dashed line along the shoulder-hand direction. $\bar{\theta}$ is the angle between the task's x-axis and the direction of maximal stiffness. The shaded area represents $\bar{\theta}$ variability around the mean 84

5.5 Statistical distributions for the three force conditions throughout the six indexes analyzed. Statistical significance (evaluated with one way-ANOVAs and post-hoc tests) is indicated with lines and stars (* for $p < 0.05$, ** for $p < 0.01$) 85

List of Tables

2.1 Effects of Task, Master device and Jacobian computation method on $\bar{R}_v$ associated with the positional task dimensions 25

2.2 Effects of Master device and Task Space dimension on $\bar{R}_v$ associated with T_{3D} 26

2.3 Pearson's correlations coefficients between R_v and d or ψ. All the ρ are significant ($p < 0.001$) 28

3.1 Maximal stiffness K_{max} in the three control modalities 47

4.1 Experiments list and description 58

Chapter 1

Introduction

1.1 Human-Robot Interaction

Over the last decades, robots have started to permeate multiple aspects of everyday life, from manufacturing [1] to assistance [2, 3], including automotive [4], home automation [5] and surgery [6]. Although carrying undeniable advantages, robots not only have to operate efficiently but also, more often, they need to achieve high levels of cooperation and interaction with humans. In this sense, sophisticated and efficient Human-Robot Interaction (HRI) represents a challenge of paramount importance towards the development and employment of the next generation of robotic devices [7].

To testify the complexity of HRI studies and the multiple interdisciplinary topics that are involved in a HRI application, as well as to propose an organic classification, Yanco et al. [8] published an updated taxonomy that includes multiple categories, spanning from task type and robot morphology to levels of shared interactions, time-space relations with the user and physical proximity. Each category is characterized by sometimes substantial differences in the nature of the HRI involved, but overall, the research community's interest has been recently focused on finding innovative ways of implementing intuitive and seamless human-robot-task interactions capable of preserving human's cognitive and decision making capabilities while taking advantage of the extreme power, precision and repeatability that robotic actuators allow.

Due to the intrinsic complexity of human and robotic systems, as well as due to the vast range of possible application scenarios, the design of cooperative and interactive robots requires an interdisciplinary cooperation between classical robotics, cognitive sciences and physiology.

1.2 HRI applications

Based on its application, Human Robot Interaction can be divided into four main areas, each characterized by different forms of interaction and challenges [9].

1. ***Human supervised tasks:*** The use of robots within industrial assembly lines has been a reality since the third industrial revolution, when robotic arms have

been employed to perform a large variety of tasks such as welding [10], painting [11] or picking and placing parts [12]. Robots are required to perform repetitive and highly standardized tasks with different levels of autonomy under human supervision.

In these applications, HRI aims to obtain a safe cooperation between robot and human, characterized by high adaptability and robustness: robots need to change and modify their behavior based on the task as well as reacting to different external inputs. Among the multiple design and control solutions that have been implemented, the introduction of compliant robotic arms allowed to narrow the physical gap between human and robots [13]. In fact, thanks to the high compliance, robots can maneuver closer to humans, without the risk of hurting them, and operators can hold and guide robots to teach specific tasks [14].

2. ***Social interactions:*** A socially assistive robot is a system that employs contactless interaction strategies such as speech, facial expressions, and communicative gestures, to provide assistance in accordance with a particular healthcare or social context. Therefore, robotic assistants are programmed to interact with humans, giving informations [15] or acting as useful tools for therapies. The necessity of establishing a relation with humans defines multiple design requirements, ranging from robots' shape and human-like appearance to the ability of tracking humans' gaze, interpreting gestures and the possibility of engaging in realistic conversations [16, 17, 18, 19, 20].

   While robots employment showed encouraging results in improving social skills in children with Autistic Spectrum Disorders [21, 22] as well as in providing health-care services to elders [23, 24], most of the findings are exploratory and have methodological limitations [25].

   With the aim of establishing more natural Human-Robot relations, researches are focusing on the feasibility for robot to learn different behaviors from human approval or disapproval feedbacks [26], assessing robot's capabilities in eliciting trust [27] and evaluating the level of engagement generated by robotic coaches [28].

3. ***Automated Vehicles:*** Over the last decade, the interest in the autonomous vehicle research field has undergone tremendous growth, thanks to its multiple successful implementations [29, 30]. Autonomous vehicles are currently developed by over 14 companies, implementing different aids for navigation, collision avoidance, adaptive speed control and automated lane following systems.

   While these features are provided to help drivers and to increase transportation's safety and comfort, they also introduced new forms of human-robot interactions: although being most of the time idle to the vehicle's autonomous decisions, humans are required to maintain situational awareness in order to face unpredictable problems. Considerable research is being, therefore, directed at the challenge of human-automation showing that a driver's ability to intervene and take over from automation when needed depends on the user's level of attention and trust [31], the level of engagement and workload [32], and the user's mental model representation of the autonomous system [33].

4. ***Teleoperation and telerobotics:*** In the last years an exponentially growing number of applications unveiled the great potentiality of physical Human-Robot Interaction (pHRI), where humans, robots and the task environment are in contact with each other, creating a complex coupled kinematic and dynamic system [34, 35, 36, 37, 38]. Those applications in which human commands directly drive robots, fall within the teleoperation branch of HRI.

   In teleoperation, the system is composed of two elements: a master side, directly controlled and manipulated by the user, and a slave side, a robot that performs the task. While it is possible to control slave robots through direct track of the user movements (by means of optoelectronic camera, or magnetic tracking [39]), the master side is usually a device whose aim is to fill the mechanical gap between the users' hand and the remote teleoperated objects. In the ideal case, the teleoperator should be able to feel present and immersed in the environment as well as being able to perform the task in the most natural way [40, 41]. Teleoperation has seen a substantial growth over the last twenty years, especially thanks to its multiple applications in handling hazardous materials, working in dangerous conditions, manufacturing and in the medical field [42, 43, 44].

   Being the connection between the user and the task performed, particular attention has been recently given to the design of master devices, both in the development of control schemes able to restore the sense of touch, as well as in their mechanical construction in order to reach higher levels of dexterity and transparency. Transparency is a key aspect of tele-manipulation and telerobotics which reflects the capability of the master robotic system to tightly follow users' command, without impairing or downgrading hand movements while allowing natural perception of interaction forces [45].

   System transparency is often linked to its stability which is directly dependent on the type of control employed in the communication between master device and slave robot. In fact, in order to achieve complete transparency with respect to the slave-environment interactions, perfect models of the master and slave robot dynamics, the absence of time delay in the transmission and information processing, as well as perfect force sensing are required [46, 47]. Without this in-depth knowledge, the transmission of haptic feedbacks to the user's hand could cause unacceptable oscillations and instability. Therefore, since these

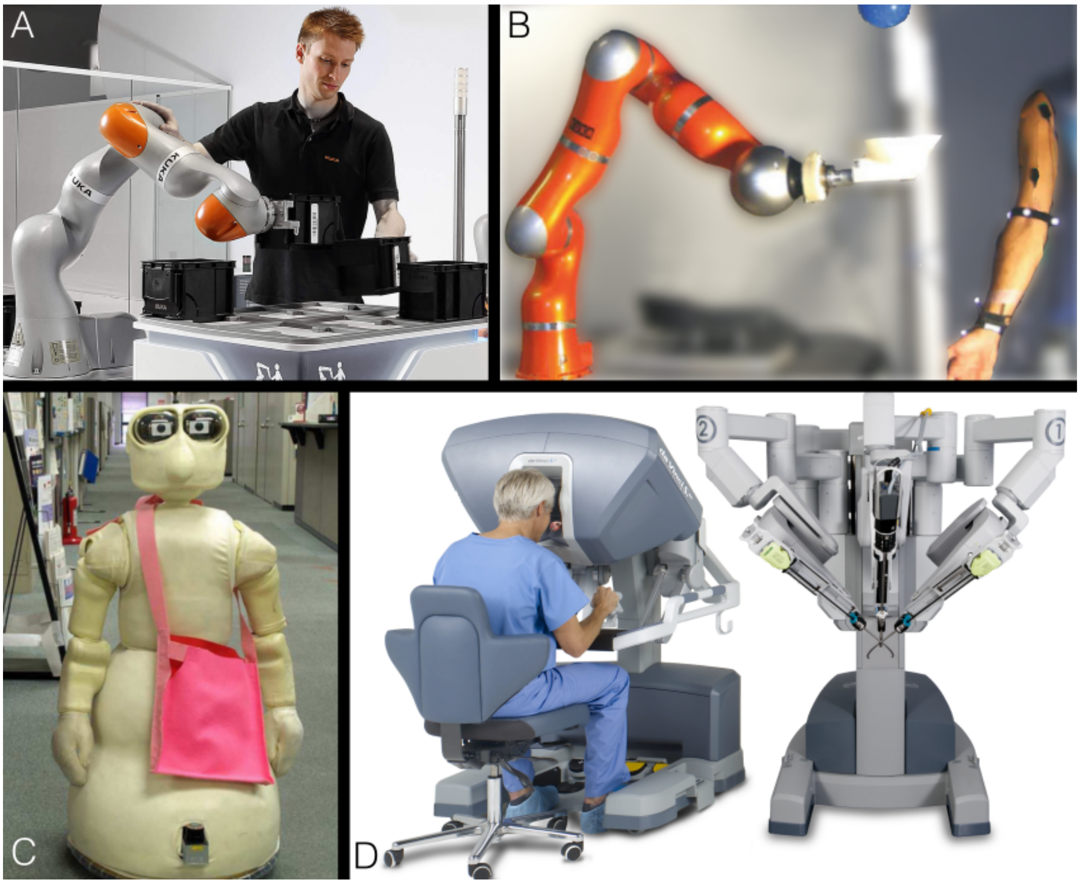

FIGURE 1.1: Different applications of HRI: **A.** KuKa Light Weight Robot cooperating with a human in an assembly task **B.** User catching a ball teleoperating a Light Weight Robot under tele-impedance control **C.** Robovie-IV from ATR IRC Laboratories, carrying a bag and interacting with humans **D.** Surgeon performing teleoperation using the Da Vinci single-site surgical robot from Intuitive Surgical, Sunnyvale, CA.

conditions can't be met in real word applications, a trade-off between transparency and stability must be adopted.

Many studies focused on the identification of the best mechanical characteristics that would allow for the easiest interaction between users and the master console. Recent works focused on the overall ergonomics and users' posture during teleoperation [48, 49], while others focused on the master device handle design [50]. The results stressed the necessity of a deeper understanding of the kinematic and kinetic characteristics of human hand and arm motion in teleoperation in order to understand which are the key elements that must be considered in the design of future master devices.

1.3 Human-Robot interactive communication

Regardless of the application and the form of communication established between human and robot, multiple studies [51] identified the necessity of achieving mutual awareness between the systems involved in HRI by continuously sharing and updating mutual models.

In fact, in order to establish an efficient and safe cooperation between human and robots, it's mandatory that both the active components of the coupled system are able to communicate and observe each other. An enhanced sensory information exchange should therefore not only allow users to be aware of how robots are interacting with them and with the environment but also to let robots *observe* and acquire new knowledge from humans [52, 53, 54, 55].

One aspect of this bilateral exchange of information is represented by the different natures of sensory interactions that could be established between human and robots: thanks to the possibilities offered by sensor fusion and the development of advanced algorithms, different means of communications have been tested, ranging from acoustic feedbacks and vocal commands [56, 52], to visual clues recognition [57, 58]. Regardless of the means of communication, the common aim of these different approaches is the necessity of making the robot aware of human intentions and needs during the various phases of the task, i.e. by receiving direct commands [59], or observing users' kinematics [60, 61].

Although these methods have been used to communicate or to predict the various subtasks performed by users, their use is often limited to the activation of high level robotic task, rather than a continuous, time varying adaptation to the user specific behavior. A promising approach in this direction, is represented by the possibility of exchanging and acquiring, through force sensing, the implicit informations that are carried with manipulative gestures. Although a partner (either human or robotic) doesn't voluntarily use gestures to communicate, but rather to perform tasks, intention can be derived by the other cooperators nevertheless. This haptic communication, that occurs in all the cases where user and robot directly or indirectly physically interact (pHRI), can be expressed through forces and torques as well as joint angle and orientation variations [62, 63]. Examples of these kind of interactions range from carrying heavy objects [64] to industrial assembly processes [65] and dancing [66, 67]. In this approach, the acquired interaction forces are used to drive the controllers that regulate the robot dynamics. Anyway, due to the impossibility of distinguishing between the forces exchanged with the users and the one arisen from the interaction with the environment, the use of these feedback based control paradigms is often limited to simple scenarios.

A solution for this limitation comes from multi-modal sensory information sensing which takes advantage of biological signals recording to infer additional informations about the user's activity while cooperating with the robot. Multiple biological signals have been studied: i.e. eye gaze [68] has been used to understand where human operators were focusing during complex tasks. Recently, the study of pupil widening along with heart rate variability and skin electrical conductivity, has been adopted to estimate the level of user's cognitive load during the execution of teleoperated tasks [69, 70]. Moreover, EMG recordings have been proven as a relatively easy to access yet powerful tool to estimate muscular fatigue and arm dynamic proprieties in multiple fields [71, 72, 73]. Moreover, recent studies [74, 75] adopted simplified model based approaches, combined with surface EMG recordings to obtain an online evaluation of human arm's impedance characteristics during human-robot cooperative tasks, enabling the possibility of achieving real-time human mimicking impedance control [39, 76].

1.4 Physical Interaction control in HRI

Different control schemes have been proposed through the years to achieve the control of slaves robots with master devices. Early teloeperation system's prototypes used position measurements from the human operator arm and hand to produce corresponding scaled movements of the slave side. Although conceptually simple, this type of control can't be safely implemented when energy is exchanged between the robot and the environment through dynamic interactions: in this case, in fact, the interaction generates unknown and potentially dangerous forces that can harm both the robot and the environment.

To solve this issue, hybrid position/force controllers have been developed [77]. In this approach, since both position and force cannot be controlled along any given direction, the task space is divided into position-controlled and force-controlled subspaces. For each manipulation task, a *n-DoFs* generalized surface can be defined in a constrained space and its used to define position constrains, normal to the surface, and force constrains, parallel to it. When turning a screwdriver, for example, force constraints are aligned with the direction of the screw, while position constraints are parallel to the surface in which the screw is inserted. Therefore, for the hybrid position/force control scheme, the only force that must be regulated is the one exerted against the screw, while precise and accurate control of the screwdriver tip position must be achieved. Although sometimes successful, these control methods failed in providing an accurate control of the commanded position or force [78].

To address this problem, Hogan firstly proposed the Impedance Control [79, 80], wherein the mechanical impedance of the manipulator is regulated to that of a target model. Impedance control aims at obtaining a stable interaction between robots and the environment during contact tasks by measuring the exchanged force and adapting the robot impedance correspondingly [81, 82]. In impedance control, the dynamic interactions between the robot and its workspace are recognized as fundamental aspects of the task, not as a source of disturbance. Obliviously, this control paradigm finds many applications in HRI, where robots interact not only with often unknown task's mechanical characteristics, but also with adaptive human arm's dynamics.

Two implementations of impedance control have been proposed and are usually referred as Impedance Control and Admittance Control in the literature. In Impedance Control the controller is modeled as an impedance and the master device as an admittance, while vice versa in Admittance control. As a result, robotic systems with Impedance Control are generally more stable when interacting with stiff environments but show poor accuracy in unconstrained movements. On the other hand, Admittance Control systems can show instability when interacting with stiff environments. Since its theoretical definition, many researches tried to combine Admittance and Impedance control, proposing control schemes that seamlessly switch between the two approaches [83].

In teleoperation, impedance control allows to acquire and feed back to the teleoperator the force interactions between the slave robots and the workspace as haptic feedback. To assure system stability, avoiding unwanted hand oscillations introduced by the master device force generation, high damping coefficients are imposed to the master device dynamics. Therefore, if high slave-environment interaction forces are suddenly acquired, the resulting haptic feedback won't generate disturbances on the teleoperator's hand. On the other hand, although assuring system stability, this solution limits the system transparency, impairing the possibility of rendering small interaction forces.

To avoid this limitation, variable adaptive impedance control has been proposed in which multiple sensor inputs are used to obtain a dynamic model of the environment [84, 85]. The master device's damping coefficient is raised when the slave robot is interacting with stiff environments, and lowered when facing compliant structures.

In other applications of variable impedance control, the dynamic parameters of the slave robot, instead, are adapted to match an estimated model of the user's arm dynamics, implementing biomimetic controllers [86, 72, 87]. In these approaches, the user arm stiffness is estimated using a combination of acquired arm kinematics and biosignals (such as EMG recordings) along with simplified musculoskeletal models of the upper limbs. Estimating the dynamic changes that occur during the execution of complex task, such as the *peg-in-hole*, it has been possible to replicate these fine motor control strategies adapting the robots parameters. In this way, the performances of the teleoperated system, as well as in cooperative tasks, improved significantly [88, 89, 76].

Recently, models of the arm impedance were also used to modify the robot's damping coefficient in cooperative pHRI [90, 91]. In these works, users interacted with a robotic handle's whose damping coefficients were modulated based on the estimated users arm stiffness. These works, as well as other similar studies [92, 93], proved the potentiality of creating dynamic models of the human arm to implement controllers that improve task performance.

1.5 Thesis motivation

Even though researchers have started to tackle the problem of enhancing the level of human-robot interaction in multiple ways and for many different applications, an unneglectable gap is still preventing humans to easily and fully take advantage of robots in complex tasks. Rather than mechanical limitations in the design of robotic actuators, a reason for this limitation seems to lie in the inability to fully transfer human motor control strategies in robotic applications.

Therefore, future robotic interfaces should not only be able to allow for an intuitive and transparent control, but should also be able to achieve higher levels of awareness of users' internal status. Master devices should accommodate to the operators' characteristics, aiding users in maintaining natural motor commands and guiding them to take full advantage of their intrinsic arm capabilities rather than forcing them to adapt to complicated inverse dynamic models.

In this sense, understanding differences in the arm kinematics generated by different master interface design, as well as understanding how the mechanical proprieties of the human arm change during task execution, should guide decisions regarding the software and hardware design of robotic master devices. In order to fully consider the human factors and peculiarities inside the teleoperation loop, a better understanding of the user kinematic and dynamic strategies must be, therefore, achieved. This improved knowledge of the users' internal models can be, therefore, shared with the robot and exploited to design interfaces able to mimic and enhance natural abilities as well as to accommodate for the arm limits with the final goal of achieving better results with a faster learning curve.

1.6 Aim of the thesis

The overall goal of this dissertation is to study the HRI in master-slave teleoperation, with the aim of narrowing the gap between the teleoperator's hand and master devices. Through the analysis presented, the central role of human arm kinematics and dynamics and their relation with the tasks performed is studied. The study aims at obtaining insights that would help in developing more intuitive and human-like master devices as well as improved control paradigms able to preserve and enhance users' motor control strategies.

To do so, the analysis first focuses on the study of two master devices: an hybrid parallel-serial robot, and a serial link manipulandum. The two master devices have been chosen as different mechanical solutions used to acquire the movements of the human hand. In the first case, the hybrid parallel-serial master device presents a structure in which the translational components of motion are mechanically decoupled from the rotations: the robot end-effector, held in the users' hand, allows for hand centered rotations that don't affect the gripper position. This mechanical solution should allow for easier control in those tasks where a fine control over orientation is required. On the other hand, the serial link master device is characterized by a kinematic structure in which translational and rotational elements are interconnected with its end-effector shaped as a stylus. Being shaped as a pen, this master device should allow for the easiest interaction with untrained users, who might find

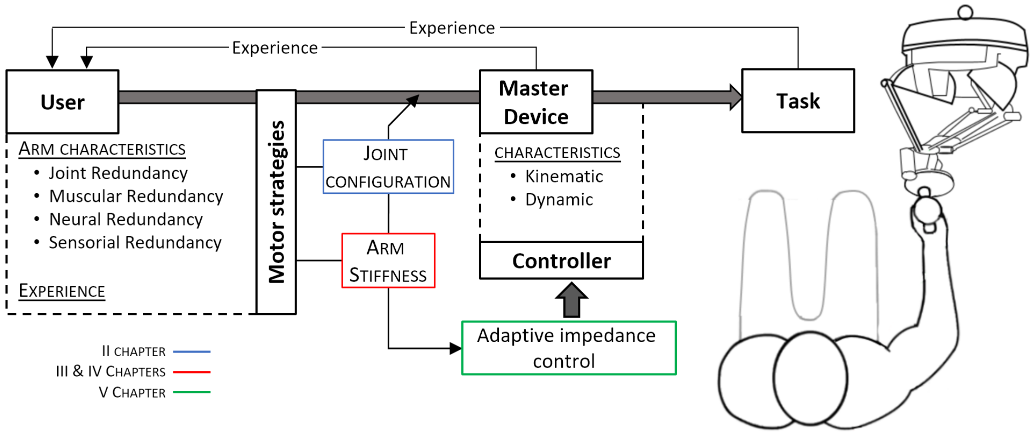
Experience
Experience
User
Master
Device
Task
Motor strategies
Arm characteristics
• Joint Redundancy
• Muscular Redundancy
• Neural Redundancy
• Sensorial Redundancy
Experience
Joint
configuration
Arm
Stiffness
characteristics
• Kinematic
• Dynamic
Controller
Adaptive impedance
control
II chapter
III & IV Chapters
V Chapter

FIGURE 1.2: Motor control paradigms in teleoperation. The interaction between user and task is mediated by the master device, whose kinematic (see Chapter 2) and dynamic (see Chapters 3 and 4) characteristics influence the motor strategies adapted to perform tasks (see Chapter 5).

it more intuitive with respect to the unfamiliar gripper of the hybrid parallel-serial link manipulandum. The different hand grip as well as the mechanical and kinematic differences between the two master devices should induce differences in the control strategies adopted by users.

The main objectives of the PhD research are summarized in the following topics:

I Understanding how two master devices and different tasks' constraints influence the kinematic strategy that allows users to exploit arm redundancy (Chapter 2).

II Study of the arm impedance control in teleoperation with two master devices as expression of the dynamic motor strategies that affect human robot interaction (Chapters 3 and 4).

III Improving task performance in virtual teleoperation through the design of a stiffness-based biomimetic variable impedance controller (Chapter 5).

1.7 Outline

This dissertation is organized in 6 chapters:

- Chapter 1 - *Motivation and Background:* in the first chapter the research context, motivations and thesis aim are presented. An overview of HRI is presented.

- Chapter 2 - *Arm redundancy analysis:* in the second chapter an uncontrolled manifold analysis of joint variability applied to two different virtual teleoperation tasks is presented. Users capabilities in exploiting arm redundancy are tested in positional and positional/orientational tasks with two master devices and the changes in arm redundancy exploitation levels are related to the task constraints and to the teleoperation performance (see Fig. 1.2 in blue).

- Chapter 3 - *Quasi-stiffness analysis:* in the third chapter, arm impedance modulation is studied during the execution of a surgical stitching mimicking task. An off-line non disruptive musculoskeletal model based technique for the estimation of quasi-stiffness is presented and used to evaluate the differences between free-hand motion and two teleoperation devices. Arm stiffness variations in magnitude and direction are correlated to the progression along the task.

- Chapter 4 - *Arm Stiffness Analysis:* In the fourth chapter, the algorithm to evaluate arm stiffness presented in chapter 3 is refined: through the acquisition of 10 muscle signals an EMG-informed inverse dynamic computation is employed to better evaluate the effects of muscular co-contraction on the arm impedance modulation. Arm stiffness variations during the execution of two virtual teleoperation tasks are estimated and the stiffness magnitude modulation is correlated with the task trajectory curvature and the hand speed and acceleration (see Fig. 1.2 in red).

- Chapter 5 - *Adaptive impedance control:* The arm stiffness modulation during a virtual teleoperation targeting task is evaluated through the non-disruptive EMG-driven musculoskeletal model based algorithm presented. Two implementations of a biomimetic impedance controller are designed to adapt the master device damping coefficients to the changes in the stiffness' magnitude and direction during task execution. The controller's performances in terms of positional accuracy, overshoots, normalized travel lengths and execution time are compared to the non-adaptive master device controller (see Fig. 1.2 in green).

- Chapter 6 - *Conclusions*: In the last chapter the dissertation's conclusion are drawn, highlighting scientific contributions, future perspectives and limits.

Chapter 2

An uncontrolled manifold analysis of arm joint variability in virtual planar position and orientation tele-manipulation

In this chapter the investigation of how master devices with different kinematics structures and how different task constraints influence users' capabilities in exploiting arm redundancy is presented. A virtual teleoperation workbench was designed and the arm kinematics of seven users was acquired during the execution of two planar virtual tasks, involving either the control of position only or position-orientation of a tool. Using the UnControlled Manifold Analysis of arm joint variability we estimated the logarithmic ratio between task irrelevant and the task relevant manifolds ($\mathbf{R_v}$). The results showed that users exploited additional portions of arm redundancy when dealing with the tool orientation. The $\mathbf{R_v}$ modulation seems influenced by the task constraints and by the users' possibility of reconfiguring the arm position.

This work is under second review (major) as: Buzzi, J., De Momi, E. & Nisky, I., "An uncontrolled manifold analysis of arm joint variability in virtual planar position and orientation tele-manipulation", *Transaction on Biomedical Engineering*

2.1 Introduction

Nowadays, teleoperated robotic systems are employed in many different fields, ranging from handling of hazardous materials, dangerous area explorations, precise manufacturing and surgery. Among the other applications of this technology, teleoperated Robot-Assisted Minimally Invasive Surgery (RAMIS) has seen a substantial growth over the last decade thanks to its several advantages with respect to standard minimally invasive surgery (MIS) [94]. While teleoperating, users (i.e. surgeons) interact with master devices to control slave instruments that directly interact with the environment (i.e. tissue). This architecture offers improvements compared to open and standard techniques, such as high precision thanks to hand motion scaling and tremor filtering. In addition, it provides teleoperators with an ergonomic and comfortable setup, and wristed robotic tools allow for high dexterity and an intuitive mapping of hand to end-effector movements [95, 96, 6, 97].

Multiple studies focused on the analysis of the relation between teleoperators and master devices, and explored different control methods ranging from keyboards, robotic devices, and optical hand tracking; these studies monitored clinically relevant performance metrics [98, 99, 100]. However, teleoperation represents a complex motor control task, and forces the users to acquire new skills to fully take advantage of this technology [101, 102, 103]. The human motor control system is characterized by multiple degrees of redundancy (kinematic, kinetic, sensory and neuronal). This redundancies allow for one of the characteristics of a healthy human movement: variability, which translates into multiple unique neural and motor patterns to solve the same motor task [104]. Instead of freezing the arm joints in the same solutions, experts exploit this redundancy, and use this variability in their arm joints to increase performance. To develop intuitive teleoperation systems and controllers, and to further understand redundancy exploitation in the human arm, it is beneficial to model the exploitation of arm kinematic and kinetic redundancy in different teleoperation and manipulation conditions [105, 106].

Multiple studies tried to assess how the Central Nervous System (CNS) solves the ill-posed problems of inverse kinematics and inverse dynamics by reducing degrees of freedom [107]. The most common approach to solve the redundancy has been the definition of kinematic and kinetic cost functions that guide the CNS in planning the best joint trajectories [108, 109, 110]. In these models, the inherent redundancy is solved by replacing the behavioral goal with the specific desired trajectory that better fits the cost function. These models require as input a detailed description of the unique and planned joint trajectories predefined by the CNS. However, the existence of variable equally valid solutions to multiple tasks involving motor redundancy, exposed the limit of these models [111].

To account for this variability in the kinematic solutions, Todorov and Jordan proposed optimal feedback control as a theory of movement coordination. In this framework, the optimal solution is achieved online with a feedback control that uses all the time-varying feedback available to correct only those deviations that interfere with the task goals [112]. A goal-oriented performance criterion together with a regularization term that minimizes control effort is defined, and the movement details are automatically filled by searching the control policy that achieves the best performance [113]. Similarly, Gelfand and Latash defined the principle of abundance for which families of solutions are generated by the CNS by covarying elemental variables so that no differences are induced in the output task space [114]. , Instead of being considered as a burden they proposed the role of motor redundancy in achieving high performance while minimizing the control effort [115].

Several methods were proposed to quantify the level of redundancy exploitation by evaluating the variability distribution in geometrically defined subspaces [116, 117, 118]. The Tolerance Noise Covariation (TNC) principle describes how humans cope with the neuromotor noise and decompose variability into exploitation of task tolerance, stochastic noise, and covariation between variables. In the TNC, the Task

Irrelevant Subspace, or Manifold (TIM), is entirely defined in the task space and, therefore, it requires an analytical model of the task dynamics. Thanks to the task dependent definition of the TIM, the TNC has been used to estimate how the three components of variance change during the learning process [116]. Another performance analysis of redundancy exploitation is represented by the Goal Equivalent Manifold (GEM) [117, 118]. The GEM is presented as the set of possible task solution strategies that arise from the theoretical definition of a goal function. Through this analysis, the sensitivity of task space errors to joint space perturbations can be estimated along with the degree of alignment between body variability and the GEM. Similarly to the TNC, the GEM is defined in the task space, thus requiring an in-depth knowledge of the task dynamics.

A powerful tool for the estimation of redundancy exploitation when the task dynamics is unknown and an analytical model that describes the task space is absent, is the Uncontrolled Manifold (UCM) analysis [119]. In this framework, the TIM definition is based on the average experimental control variables trajectories, allowing the extension of performance evaluation to those fields where there is no a-priori knowledge of the task goal. Within the UCM framework, in accordance with the Minimum Intervention Principle (MIP) [112], humans control and limit the variability aligned with the task related manifold (TRM) while leaving unrestrained the task-irrelevant (TIM) variability that has no effect on the task performance. For linear systems, the TIM can be computed as the null space of the matrix that relates control variables to task variables. For nonlinear systems, an approximation of the TIM can be computed as the null space of the linearized relation between control variables and task variables. Instead of analytical linearization, a linear relation can also be estimated from sampled data by means of linear regression approximation [120].

Recently, Sternad et al. [121] demonstrated that the UCM analysis is sensitive to the choice of the coordinates that are used to define the task related and unrelated manifolds. An elegant solution to this problem was recently proposed [122], but it was only applied to static tasks to date. In this study, we focus on dynamic tasks in which the structure of the GEM is not well-defined. Therefore, in spite of its limitations, we chose to employ the UCM, and we discuss the limitations in depth in the discussion section.

The UCM analysis was adopted to study a large variety of tasks such as reaching movements [119], bimanual pointing [123], stone knapping [124] and isometric finger force exertion [125]. Recently, it was employed in robotic teleoperation [126] to discriminate between expert and novice teleoperators and investigate the effect of teleoperation manipulator dynamics on redundancy exploitation. Nisky et al. showed how expert teleoperators exploited their arm kinematic redundancy more than novices and especially when teleoperating.However, this study only focused on simple point-to-point reach movements, and compared a single teleoperation manipulator to freehand.

In RAMIS, many tasks involve movement along curved paths and a control of the orientation of the master manipulator and the surgical instruments [127, 128, 129]. Quantifying the control of orientation was recently shown to be promising for assessment of surgical skills [128, 129]. Only few previous studies analyzed how tasks that require control of orientation affected motor redundancy exploitation using the UCM approach, [130, 131]. For example, Morrison et al. recently showed how golfers used different levels of redundancy exploitation through the golf swing execution, and that they favored the control of the golf clubhead orientation rather than its position. The control of orientation during fine manipulation tasks is yet to be fully understood, and in the studies that focused on orientation, the redundancy exploitation that is associated with the position or orientation are analyzed in isolation [123, 131, 130, 129, 132, 133]

In this study, to address the aforementioned gaps, we employ the UCM framework to analyze how the characteristics of the task, in form of different levels of curvature, may influence the coordination of variability in the control variables throughout the tasks execution. We also seek to understand how users prioritized the control of position and orientation in a combined path and orientation tracing task. We designed two tracing in virtual teleoperation. The tasks involve different task space dimensions and natures: we compared the exploitation of redundancy during the execution of a two-dimensional planar position tracing with the exploitation of redundancy during the execution of a three-dimensional planar task, in which both the position and the orientation of a virtual tool had to be controlled.

Our hypotheses are the following:

(HP1) Users may maximize the task redundancy exploitation in face of high complexity portions of the trajectory.

(HP2) The mechanical, dynamic and work space differences between a hybrid parallel/serial link (Sigma) and a serial link (Omni) master device would modify novice users' capabilities of exploiting the arm redundancy.

(HP3) Mixed position-orientational task constraints may influence users capabilities in exploiting arm redundancy.

2.2 Methods

2.2.1 Tasks design

Two tasks were developed in a virtual reality scenario (Vrep, Coppelia Robotics, Zurich, Switzerland) to challenge users with different task goals and complexities. Users were asked to precisely follow a path at a self defined comfortable speed (tracing task) and, for both tasks, an eight-shaped path was chosen. The path was modeled as half of the cloverleaf motions presented by Levit-Binnun et al. [134].

1. ***Task 2D*** (T_{2D}): Users were requested to follow the path with a virtual stylus tool (Fig. 2.1.A). They started from an initial position (green dot in Fig. 2.1.A) and moved first counter-clockwise, then straight crossing the intersection in

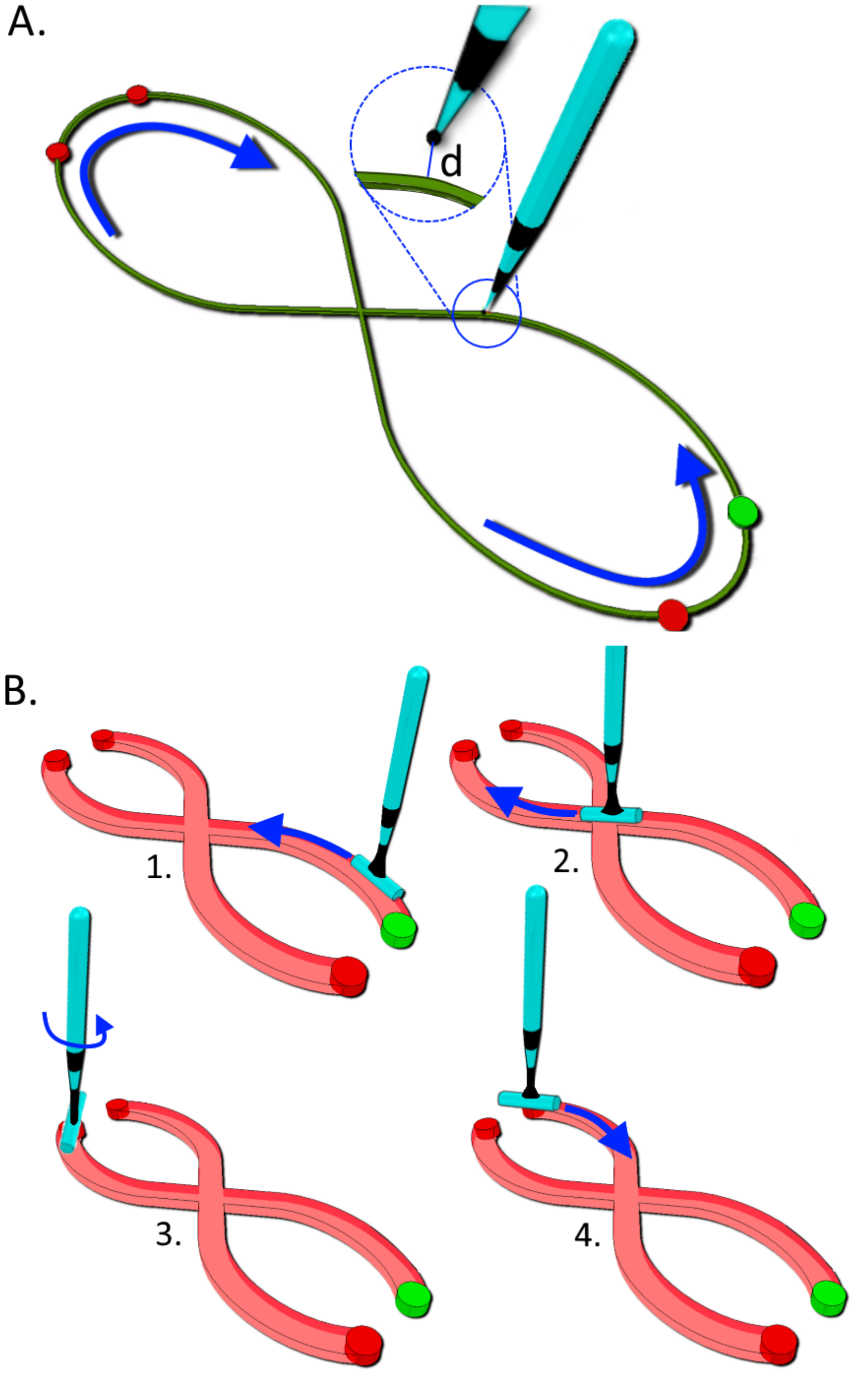

FIGURE 2.1: The two virtual tasks that were developed. In T_{2D} (A) users were required to follow an eight-shaped path controlling a virtual stylus tip. In T_{3D} (B), users were also required to control the tool's orientation throughout the path

the middle, finally in a clock-wise direction to return to the starting position. To compensate for the absence of tridimensional depth perception, the path color turned green when the tool-tip of the stylus was within ± 20mm from the plane where the trajectory lied or red otherwise. Users were required to precisely minimize the x-y distance between the tool tip and the path while avoiding to excessively stray way from the task plane. Since an intuitive and immediate visual feedback was present for the x-y errors only, due to the lack of 3D perception, only these task dimensions were considered in the UCM analysis ($d_{task,T_{2D}}$ = 2 , see Fig. 2.2.B).

2. ***Task 3D (T_{3D})***: Users were required to follow the same path while also orienting the cylindrical tool tip along the path, as shown in Fig. 2.1B. The tool end-effector had to slide over the shape fitted path starting from the green dot (Fig. 2.1.B.1). Due to the structure of the master devices (see Section **??**), to twist the virtual tool, users had to rotate their wrist while maintaining fingers' grip over the handle of the devices fixed. After flexing the wrist until the central intersection was reached (Fig. 2.1.B.2), users had to extend it to reach the top left. At the upper open end of the path (red dot in (Fig. 2.1.B.2), the users had to reposition the tool end-effector on the shape fitted path (see Fig. 2.1.B.3). Similarly, the users had to reach the lower open end (Fig. 2.1.B.4) to complete the task. The same color feedback as in T_{2D} was adopted. In T_{3D} the task space is composed of two positional (x,y) and one rotational (α) element, therefore $d_{task,T_{3D}}$ = 3 (see Fig. 2.2.B).

2.2.2 Master devices

The virtual teleoperation tasks were implemented using two master devices: a 6+1 DoFs hybrid parallel/serial link haptic interface (Sigma) and a 6 DoFs serial links haptic interface (Omni).

1. Hybrid Parallel/Serial master device (Sigma): The Force Dimension Sigma7 (Force Dimension, Nyon, Switzerland) was used as Sigma and it's characterized by six degrees of freedom plus an active grasping control (see Fig. 2.2.A.2). The master device is gravity compensated, has a resolution of *0.0015 mm* and *0.013 deg* and its workspace can be approximated to an elliptical dome with radiuses of *190x130 mm*. The master device controller, based on a Linux API, sampled the gripper position and orientation at *1kHz*.

2. Serial Link master device (Omni): A Phantom Omni (3D Systems, South Carolina, USA) was used as Omni (see Fig. 2.2.A.3). Controlled by a stylus end effector, within the parallelepipedal workspace of *160x120x70 mm*, the device is characterized by a resolution of *0.055 mm*. Omni's position and orientation not gravity compensated controller ran at *500Hz*.

2.2.3 Acquisition framework

The kinematics of the user was acquired using two localization devices: the thorax position was acquired using an optical localization system (see Fig. 2.2.A.4) (Vicra, Northern Digital, Ontario, Canada, 20Hz sampling rate, *0.25 mm* position Root Mean Squared Error) using three passive retroreflective markers attached to the right and left acromions and next to the jugular notch (see Fig. 2.2.A.5).

The arm, forearm and hand positions were acquired using an electromagnetic localization system (see Fig. 2.2.A.6) (Aurora, Northern Digital, Ontario, Canada, 30Hz sampling rate, *0.48 mm* and *0.3 deg* position and orientation RMSE, dome shaped field with a radius of approximately 500mm) and three 6-DoF 1.8×9 *mm* electromagnetic sensors (see Fig. 2.2.A.7).

The electromagnetic 6-DoF markers were used to generate 2 virtual markers for each body segment and they were placed at recognizable body landmarks calibrated on the users' elbow, wrist and hand in a pre-acquisition phase. The two acquisition systems were then registered to the same reference frame using an Hand Eye calibration approach [135].

2.2.4 Experimental protocol

Seven healthy right handed users were recruited (4 female and 3 male, mean age 23 ± 1.5 y.o.) and provided informed written consent in accordance with the Declaration of Helsinki.

The users were sitting in front of a desk, where a 2D monitor (see Fig. 2.2.A.1) was laid as flat as possible to be approximately parallel to the plane in which the tasks were performed (see Fig. 2.2.A.9). The seat position and height was adjusted for each subject to achieve the best personal comfort and interface with the master devices. Subjects were instructed to find their own trade-off between precision and execution speed during the execution of the tasks, that were performed with both master devices for each user.

For each subject, the experiment order was randomized so that users performed 10 repetitions of a randomly selected experiment before moving to the next one.

2.2.5 Joint angle estimation

The users' arm was modeled as three rigid segments and 7 degrees of freedom. The shoulder joint was modeled as a ball and socket joint, comprising abduction-adduction, flexion-extension and external-internal rotation of the forearm. The elbow was modeled as a single flexion-extension DoF while the wrist joint consists in three DoFs: pronation-supination, flexion-extension, abduction-adduction [136].

To estimate the arm joint configuration, OpenSim's inverse kinematics and a widely adopted upper limb musculoskeletal model were adopted [137, 138, 139]. Raw marker movements were filtered (recursive 2nd order Butterworth filter with cut-off frequency *6Hz*) and static acquisitions were used to scale the model to fit the

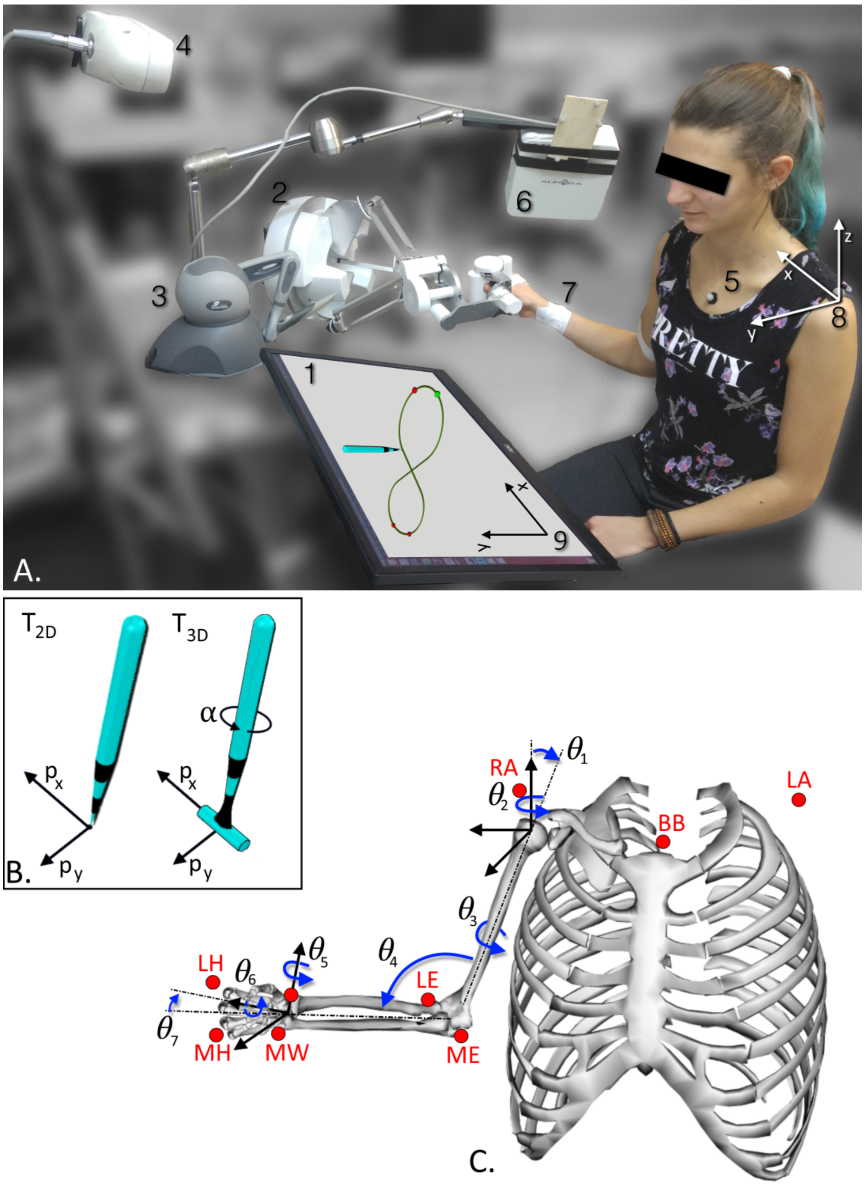

Figure 2.2: **A.** The experimental setup: user performs the tasks while looking at a flat screen (1) and teleoperating with the hybrid parallel/serial link master device (Sigma - 2) or using the serial link master device (Omni - 3). The thorax movements are recorded using an optic camera (4) with three retroreflecting markers (5) while the arm kinematics is acquired with an electromagnetic tracker (6) and 6DoFs markers (7). The shoulder reference frame (8) is grossly aligned with the VR one (9). **B.** Task space dimensions for T_{2D} and T_{3D}. **C.** The OpenSim model used for the inverse kinematics. In blue the seven degrees of freedom (1, 2 . . . 7) and in red the virtual markers set-up: Left and Right Acromium (LA, RA), Breast Bone (BB) for the thorax, Lateral and Medial Elbow (LE, ME) for the arm, Lateral and Medial Wrist for the forearm (LW, MW), Lateral and Medial Hand (LH, MH) for the hand orientation. In the magnifying box: T_{2D} and T_{3D} task spaces.

users' arm and thorax dimensions. The offline inverse kinematics algorithm takes as input each frame of the acquired markers positions and finds the best joint vector q that minimizes the error between the experimental and virtual marker positions:

$$\min_{\mathbf{q}}[\sum_{k=1}^{K}\|\mathbf{p}_k^{acq} - p_k^{virt}(\mathbf{q})\|^2] \tag{2.1}$$

With $\boldsymbol{q}$ vector of joint angles, $\mathbf{p}_k^{acq}$ is the acquired 3D position of the k^{th} marker, $\mathbf{p}_k^{virt}(\mathbf{q})$ is the position of the corresponding virtual marker on the model that depends on the vector of joint angles $\boldsymbol{q}$ and K is the number of markers.

2.2.6 Uncontrolled Manifold Analysis

To analyze the coordination between the arm joint angles and the task execution, we adopted the Uncontrolled Manifold Analysis (UCM) [140]. To evaluate the stability of joint angles around the time-varying reference path, we first computed the trial-to-trial variability around an average path. We assume that, for each user, task, and master device, the same arm state is defined by the CNS as a kinematic strategy to follow the space-normalized path [141]. While we do not know what the real reference path is, and whether such reference exists in the motor system, for the sake of the analysis, these reference joint and task space trajectories were estimated from the between-trials average path.

First, to account for the between-user and between-trial variability in the task execution speed, the kinematic data from the inverse kinematic algorithm ($\theta_{u,n,m,r}$) was space-normalized using the curvilinear abscissa of the path $[s]$. All the task trials among the different users were re-sampled at the same number of equally-spaced samples that was equal to the number of frames of the shorter trial. Then, the between-trials average trajectories and the variability around them could be computed. Therefore, the total joint-space variance $V_{\theta_{u,n,m}}$ is defined as:

$$V_{\theta_{u,n,m}}[s] = \sum_{r=1}^{N}\|\theta_{u,n,m,r}[s] - \bar{\theta}_{u,n,m}[s]\|^2 d_{joints}^{-1} N^{-1} \tag{2.2}$$

where $\theta_{u,n,m,r}$[s] represents the joint angles vector for the u^{th} user $(u = 1 : U, U = 7)$, n^{th} task $(n = T_{2D}, T_{3D})$, m^{th} master device $(m = Sigma, Omni)$, r^{th} trial $(r = 1 : N, N = 10)$ at the s^{th} space-normalized sample (s = 0:1) solution of the inverse kinematics algorithm, and $\bar{\theta}_{u,n,m}$[s] represents the average (across the N repetitions of the same task) joint angles vector at the s^{th} space-normalized sample. The joint-space dimension $d_{joints} = 7$ is the number of joints in our model of the arm.

For small deviations from the average path, the joint kinematics can be linearized using the Jacobian matrix $J(\theta[s])$ that relates joint velocities $\dot{\theta} = [\dot{\theta_1}, \dot{\theta_2}, \ldots, \dot{\theta_n}]$ to the end-effector Cartesian (x, y, z) and angular (γ, β, α) velocities $\dot{x}$:

$$\dot{\mathbf{x}} = \mathbf{J}(\boldsymbol{\theta})\dot{\boldsymbol{\theta}} \tag{2.3}$$

To obtain a linear approximation of the TIM, the null space of the Jacobian at each average configuration was computed.

$$J(\bar{\boldsymbol{\theta}}_{u,n,m}[s]) \cdot \boldsymbol{\epsilon} = 0 \tag{2.4}$$

Where $\boldsymbol{\epsilon}$ is the basis vectors matrix, whose dimension is $d_{TIM} = d_{joints} - d_{task}$ and $\bar{\boldsymbol{\theta}}_{u,n,m}[s]$ is the mean joint trajectory defined as follows.

$$\bar{\boldsymbol{\theta}}_{u,n,m}[s] = \frac{1}{N}\sum_{r=1}^{N} \boldsymbol{\theta}_{u,n,m,r}[s] \tag{2.5}$$

Using the null space basis vector matrix ϵ it's possible to project the deviations from the average joint path onto the null space:

$$\boldsymbol{\theta}_{TIM_{u,n,m,r}}[s] = \boldsymbol{\epsilon}\boldsymbol{\epsilon}^T(\boldsymbol{\theta}_{u,n,m,r}[s] - \bar{\boldsymbol{\theta}}_{u,n,m}[s]) \tag{2.6}$$

and onto the orthogonal task-relevant manifold (TRM):

$$\boldsymbol{\theta}_{TRM_{u,n,m,r}}[s] = (\boldsymbol{\theta}_{u,n,m,r}[s] - \bar{\boldsymbol{\theta}}_{u,n,m}[s]) - \boldsymbol{\theta}_{TIM_{u,n,m,r}}[s] \tag{2.7}$$

In the tracing task presented, the TRM can be visualized as a combination of joint angle variations that affect task performance, generating movements of the tool's end-effector. The TIM is composed of joint angle variations that will leave task performance unaltered by leaving the position of the tool end-effector unchanged. Importantly, while geometrical orthogonality is not defined between joint angle variations, if the linearization holds true, a mathematical orthogonal manifold can always be extracted.

Similarly to Eq. 2, it's possible to obtain the variance associated to the two projections:

$$V_{TIM_{u,n,m}}[s] = \sum_{r=1}^{N} \|\theta_{TIM_{u,n,m,r}}[s]\|^2 d_{TIM}^{-1} N^{-1} \tag{2.8}$$

$$V_{TRM_{u,n,m}}[s] = \sum_{r=1}^{N} \|\theta_{TRM_{u,n,m,r}}[s]\|^2 d_{task}^{-1} N^{-1} \tag{2.9}$$

Where d_{task} is the task space dimension which represents the number of Cartesian and angular degrees of freedom that the users are required to control to perform the task and depends on the task type. To estimate the users' capabilities in exploiting the arm redundancy, without being biased by the overall joint-space variance, the logarithmic ratio between the two variances $R_v[s]$ is computed:

$$R_v[s] = \log\left(\frac{V_{TIM}[s]}{V_{TRM}[s]}\right) \tag{2.10}$$

When R_v is positive, users' variability along the TIM is higher than V_{TRM}, showing that users' are exploiting arm redundancy.

2.2.7 Jacobian estimation

When the model of the arm is available, the Jacobian matrix can be obtained from the concatenation of the homogeneous matrices that define the forward kinematics and their derivation. In this study, we use the user specific scaled model obtained through OpenSim to obtain the analytical expression of the Jacobian. To apply the UCM analysis, it is necessary to reduce the dimension of the full rank Jacobian to account for the task space dimensions that users were trying to control.

The Jacobian is computed with respect to the shoulder reference frame, which is aligned with the task space frame. Therefore, to extract the task space positional components in the x-y plane (see Fig. 2B), it's possible to extract the corresponding Jacobian rows. On the other hand, the α rotation that users were required to control (see Fig. 2B) is defined in the end effector reference frame and corresponds to the tool pitch angle. With respect to the shoulder reference frame, depending on the arm configuration, this angle might have components in all the three rows of the Jacobian rotational part, consequently, it would be less intuitive to extract the α angle only. The Jacobian was therefore also estimated with a regression method from the joint angle variations and the tasks space variables variations, accounting for the positional and rotational components of T_{3D}, as presented by De Freitas and Scholz [142]. To validate the numerical estimation, for T_{2D}, we computed the logarithmic ratio of the variances on both the analytical and numerical estimation of the Jacobian. For T_{3D}, only the numerical computation was adopted.

1. ***Task 2D** (T_{2D})*:The task space was planar ($x - y$ coordinates) with $d_{task,T_{2D}} = 2$, and therefore, only the first two rows of the Jacobian are considered. The Jacobian matrix associated with this task can be expressed as follows:

$$\mathbf{J}_{2D,A} = \begin{bmatrix} \frac{\partial\theta_1}{\partial x} & \frac{\partial\theta_2}{\partial x} & \dots & \frac{\partial\theta_{d_{joint}}}{\partial x} \\ \frac{\partial\theta_1}{\partial y} & \frac{\partial\theta_2}{\partial y} & \dots & \frac{\partial\theta_{d_{joint}}}{\partial y} \end{bmatrix} \tag{2.11}$$

   where the subscript 2D indicates the positional task space dimensions considered and A refers to the Analytical computation of the Jacobian.

   In addition, the Jacobian associated with the positional task space (2D) was also estimated with the regression method $\mathbf{J}_{2D,LSQ}$.

2. ***Task 3D** (T_{3D})*: In T_{3D}, the elements of the Jacobian matrix were estimated with independent linear regressions between across-trial joint configurations and the end-effector tip positions and pitch angle (see Fig. 2B). Each row of the Jacobian matrix ($J_{3D,LSQ}$) was computed separately for each task space dimension and for each path-normalized sample as follows:

$$\Delta px_{u,n,m,r}[s] = \mathbf{J}_x \Delta\boldsymbol{\theta}_{u,n,m,r}[s] \tag{2.12}$$

$$\Delta py_{u,n,m,r}[s] = \mathbf{J}_y \Delta\boldsymbol{\theta}_{u,n,m,r}[s] \tag{2.13}$$

$$\Delta\alpha_{u,n,m,r}[s] = \mathbf{J}_{\alpha}\Delta\boldsymbol{\theta}_{u,n,m,r}[s] \tag{2.14}$$

Where px, py and α are the user controlled task space variables, J_x, J_y and J_α are the 1×7 separate rows of $\mathbf{J}_{3D,LSQ}$, $\boldsymbol{\Delta\theta}_{u,n,m,r}$ is the displacement from the mean joint configuration and $\{px, py, \alpha\}_{u,n,m,r}$ are the displacements from the task space variables for the u^{th} user, n^{th} task, m^{th} master device and r^{th} repetition.

Under the assumption that the same arm state is defined for the same path position for each user and repetition, a system of ten equations corresponding to the 10 task repetitions can be defined for each line in Eq.2.12,2.13,2.14. Therefore, for each user, task, normalized frame and task space dimension, an overdetermined system of 10 equations with 7 unknowns has to be solved to obtain the corresponding Jacobian row. To improve the conditioning of the regression, the space-normalized signals were binned such that bins of 5 normalized samples were used to estimate each set of unknowns, thus solving systems of 50 equations with 7 unknowns using a Least Square Method (LSQ). Similarly, removing the J_α row, the LSQ method can be used to estimate the $J_{2D,LSQ}$.

2.2.8 Data Analysis

Redundancy Exploitation

We used the R_v value to measure the joint redundancy exploitation for each experiment and user in each normalized frame.

To analyze the possible modulation of the level of redundancy exploitation *(HP1)*, and to test if the capability of efficiently partitioning joint variability in the task relevant and irrelevant manifolds was influenced by the path characteristics, we evaluated the R_v along the normalized path. The trajectories of the two tasks were divided into eight parts, characterized by three levels of absolute curvature (Fig. 3.1) that were analytically obtained for each point along the bi-dimensional trajectories as in Buzzi et al. [105].

We used the Liellefors test ($\alpha = 0.05$) to evaluate the normality of the R_v distributions for each normalized sample *[s]* in each experiment among the seven users. Since the distributions were normal, the mean R_v trajectories and the corresponding standard deviations in the four experimental conditions were obtained at each s^{th} space normalized sample.

No significant trends were found in the R_v throughout the path, and therefore, the R_v mean values ($\bar{R}_{vu,n,m}$) were extracted and grouped among users.

$$\bar{R}_{v\,u,n,m} = \frac{1}{T_{norm}} \sum_{t=0}^{1} R_{vu,n,m}[s] \tag{2.15}$$

To test differences between master devices *(HP2)* and tasks *(HP3)*, as well as evaluating the differences between the two Jacobian computation methods, we fitted a 3-way repeated-measures ANOVA model with mean R_v as dependent variable, task type, master device, and Jacobian computation method as fixed-effect within-user main independent factors; the interaction effects between the main factors were also evaluated. In this analysis, we compared the mean R_v for all the experiments when a 3D task space is considered.

Focusing on T_{3D}, the $\bar{R}_v$ was computed considering both the 2D positional task space (*x*-*y*) and considering the additional tool orientation (*x*-*y*-α). To evaluate the differences in the R_v introduced by the task space dimension, a follow up analysis was conducted on T_{3D}. Using the LSQ Jacobian estimation method only, a 2-way repeated measures ANOVA was used to describe the data distributions in T_{3D} in which master device and task space dimension as well as their interaction are the fixed effect independent within users factors.

Error metrics

During the tasks execution, we evaluated the following metrics:

- *Positional error (d):* for both T_{2D} and T_{3D}, we computed the planar Euclidean distance ($x - y$) between the tool's end-effector tip and the closest point along the central line of the path (Fig. 2.1.A).

$$d_{u,n,m,r}[s] = \sqrt{\begin{aligned}&(px_{u,n,m,r}[s] - tx_{u,n,m,r}[s])^2\\ &+ (py_{u,n,m,r}[s] - ty_{u,n,m,r}[s])^2\end{aligned}} \tag{2.16}$$

  With tx and ty x and y coordinates of the closest point on the path center line in the *[s]* space normalized frame.

- *Angular error (ψ):* for T_{3D} only, the angular displacement between the tool end effector pitch angle and the tangent to the path pitch angle in the closest point along the path was evaluated (Fig. 2.1.B).

$$\psi_{u,n,m,r}[s] = p\alpha_{u,n,m,r}[s] - t\alpha_{u,n,m,r}[s] \tag{2.17}$$

  Where $t\alpha$ is the pitch angle of the tangent to the curve.

The normality of the distribution of d and ψ for each space normalized stamp among users and repetitions was tested (Liellefors test $\alpha = 0.05$). Since the distributions were normal, the median $\bar{d}$ and $\bar{\psi}$ curves were extracted for each experiment.

To test the correlation between R_v and the error metrics (d for T_{2D} and T_{3D} and ψ for T_{3D}) through the path, the Pearson linear correlation coefficient was computed for each experiment and user. Moreover, as a measure of the general correlation, we computed the Perason linear correlation between the mean R_v and the mean position (d) and orientation error (ψ) throughout all the users acquired.

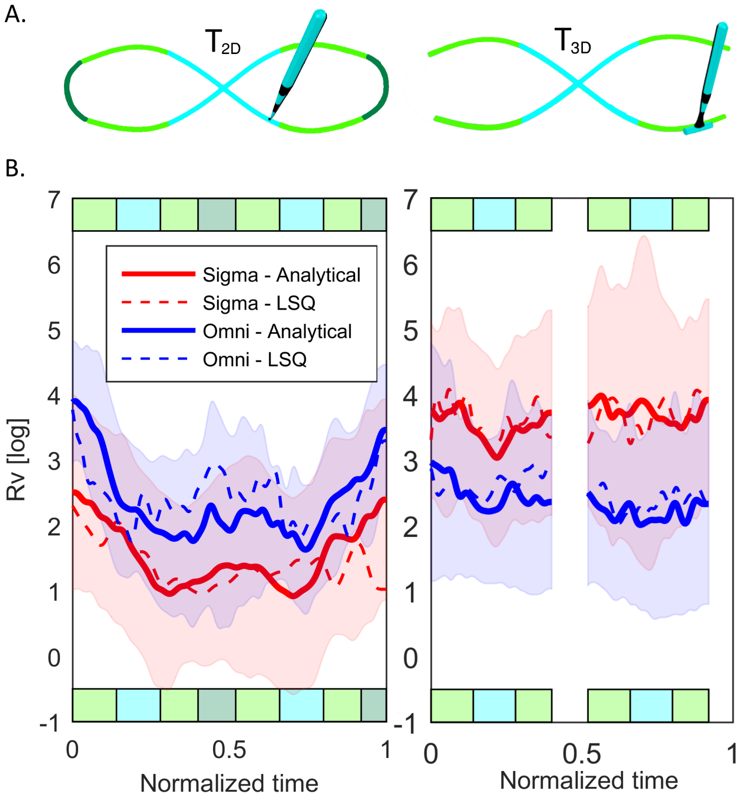

FIGURE 2.3: *(HP1)* A. The curvature regions in the two tasks. B. Mean positional R_v and standard deviations through the trajectories while teleoperating with Sigma (in red) and Omni (in blue)

The mean d and ψ values among the ten repetitions and users were extracted for each experiment to test differences between master devices and tasks for d and between master devices only for ψ. Therefore, for the positional error d we fitted a 2-way repeated-measures ANOVA model with task type and master device as fixed effect within users independent factors. For the orientation error ψ, we used a 1-way repeated-measures ANOVA model with master device as fixed effect withing user independent factor.

2.3 Results

2.3.1 Redundancy Exploitation

We first focused on the analysis of the redundancy exploitation associated with the bi-dimensional tool position only, for both tasks, regardless of differences in the task space dimension. Fig. 2.3 shows the R_v modulation throughout the trajectories for the different master devices in the two tasks. For T_{2D}, the R_v was computed using $J_{2D,A}$ and $J_{2D,LSQ}$ (dashed line), while for T_{3D} only $J_{2D,A}$ is presented. The color bars at the top and bottom of the graphs correspond to the levels of curvature. Since the highest curvature part of the path (dark green) was missing from T_{3D}, the corresponding parts of the graphs were left empty. A modulation of R_v can be seen

TABLE 2.1: Effects of Task, Master device and Jacobian computation method on $\bar{R}_v$ associated with the positional task dimensions

Source	df	F	P
Tasks	1	**12.06**	**0.0009**
Master Devices	1	2.10	0.154
Jacobian type	1	1.53	0.225
Tasks*Master Devices	1	1.09	0.303
Tasks*Jacobian type	1	0	0.988
Master Devices*Jacobian type	1	0.01	0.913
Tasks*Master Devices*Jacobian type	1	0.58	0.452
Total	54		

in T_{2D}, where at the beginning and at the end of the path, users generally showed higher values with respect to other sections. Moreover, R_v slightly increased in the central part of the path. On the other hand, in T_{3D}, users did not show any noticeable change in their exploitation of the arm redundancy; in fact, in this case, the R_v did not change throughout the path.

From the comparison between the two Jacobian computation methods that is presented in Fig. 2.3.B, in T_{2D}, the LSQ method seems able to follow the Analytical computation within the variability range.

Fig. 2.4 shows the R_v for T_{2D} and T_{3D} performed with the different master devices. The graph shows a comparison between the R_v values for the positional task variables only (2D) obtained using the two Jacobian estimation methods: Analytical (A) and Least Square regression (LSQ). The results of the three-way ANOVA analysis performed are reported in Table 2.1. Users showed higher $\bar{R}_v$ values associated with the positional aspects of the task execution while performing the second task and this difference was statistically significant ($p < 0.001$). No differences were found between the R_v values obtained using the Analytical and the Least Square Jacobian estimation or between master devices.

In the second part of the analysis we focused on T_{3D}, studying the contribution of the tool end-effector orientation (α) to the redundancy exploitation. Fig. 2.5 shows the $\bar{R}_v$ distributions for T_{3D}, computed considering the positional task space variables only (2D) and with the additional rotational task space variable (3D). When accounting for the rotational task space variable, users showed higher $\bar{R}_v$ values with respect to the 2D case, and this difference was significant ($p < 0.05$). Users showed roughly the same capability of exploiting the arm redundancy while teleoperating with the two master devices (Sigma/Omni) and no interaction effect was found either (see Table 2.2).

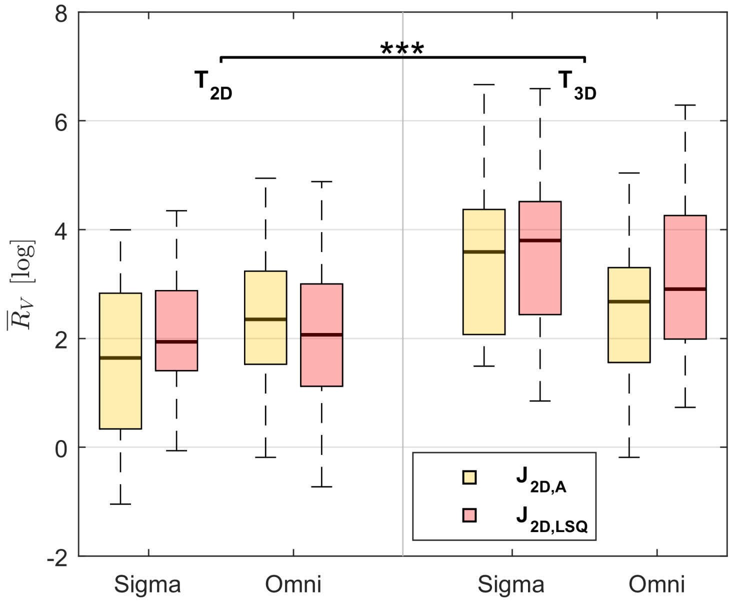

FIGURE 2.4: *(HP2 & HP3)* R_v distribution among the experiments: T_{2D} and T_{3D} performed with the hybrid parallel/serial link robot and with the serial link one, computed using the analytical Jacobian ($J_{2D,A}$) and with the Least Squares Jacobian ($J_{2D,LSQ}$). The boxplots represent median values, first and third quartiles and minimal and maximal values. The statistical differences are depicted using lines and stars.

TABLE 2.2: Effects of Master device and Task Space dimension on $\bar{R}_v$ associated with T_{3D}

Source	**df**	F	**P**
Master Devices	1	0.01	0.910
Task Space Dimension	1	**4.31**	**0.048**
Tasks Dimension *Master Devices	1	0.67	0.420
Total	27		

2.3.2 Error metrics

Fig. 2.6 shows the mean positional error changes though the path for T_{2D} and T_{3D}. The orientation error, described by ψ is reported for T_{3D} only. For the positional error, a clear trend can be seen in T_{2D} for both master devices: the error decreases in correspondence with the high curvature parts of the path and increases when moving along the straight parts, almost symmetrically with respect to the normalized progression along the path. Similar behavior can be seen for the positional error in T_{3D}, in which users showed minimal error when re-engaging the path after the open ends.

For ψ in T_{3D}, trends are less evident, but, as expected, the angular displacement between the end-effector direction and the tangent to the path was minimal on the straight portions of the trajectory.

Table III shows the correlation indexes (ρ) between R_v and d and ψ in the four experiments among the users as well as the correlations between the mean R_v values and the mean d and ψ curves. Although users' performance was characterized by different levels of correlation, the mean curves suggest that the positional error (d) correlates negatively with the R_v changes in T_{2D} for both master devices. Regarding T_{3D}, both $\bar{d}$ and $\bar{\psi}$ showed very little correlation with the $\bar{R}_v$ modulation, but this is very likely due to the absence of modulation in the R_v and error values in T_{3D}.

Finally, regarding the positional error d, the ANOVA results showed no statistical difference between T_{2D} and T_{3D} ($F_{1,22} = 1$, $p = 0.33$) nor between Sigma and Omni ($F_{1,22} = 0.04$, $p = 0.84$). In the same way, for ψ, the 1-way ANOVA showed no statistical difference between Sigma and Omni ($F_{1,22} = 1.5$, $p = 0.25$).

2.4 Discussion

We used the UCM analysis to investigate how different task constraints and master devices influence users' exploitation of arm redundancy. We found a significant modulation in the level of redundancy exploitation throughout the path in the positional task but less significant in the mixed position-orientation one. We used two Jacobian estimation methods (analytical and least square regression) and found that they were equally able to estimate the R_v values in the positional task. During the execution of the position-orientation task, users achieved higher values of redundancy exploitation. Surprisingly, no significant differences were found between the two master devices tested in both tasks. We also analyzed task performance: no

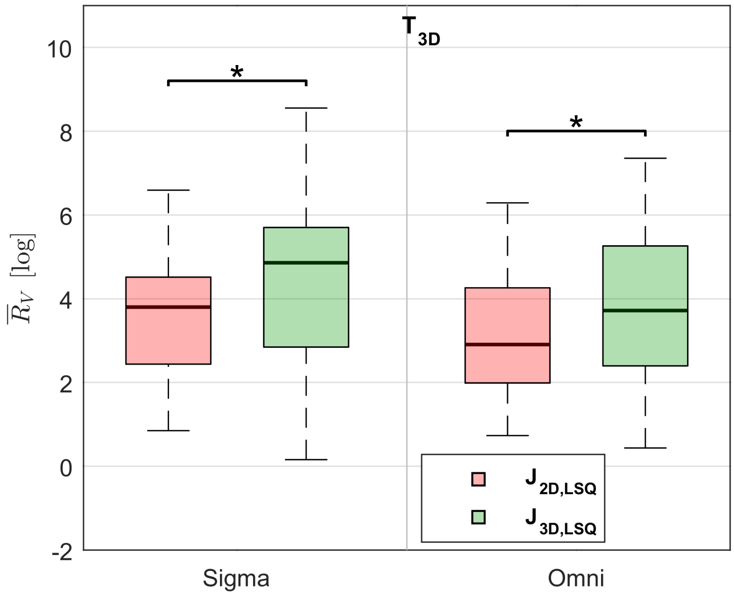

FIGURE 2.5: *(HP3)* Differences in the R_v distribution among users between different master devices and task space variables considered. In red the results obtained considering the positional only task variables (J_{2D}) and in green when also the tool rotation is accounted (J_{3D}).

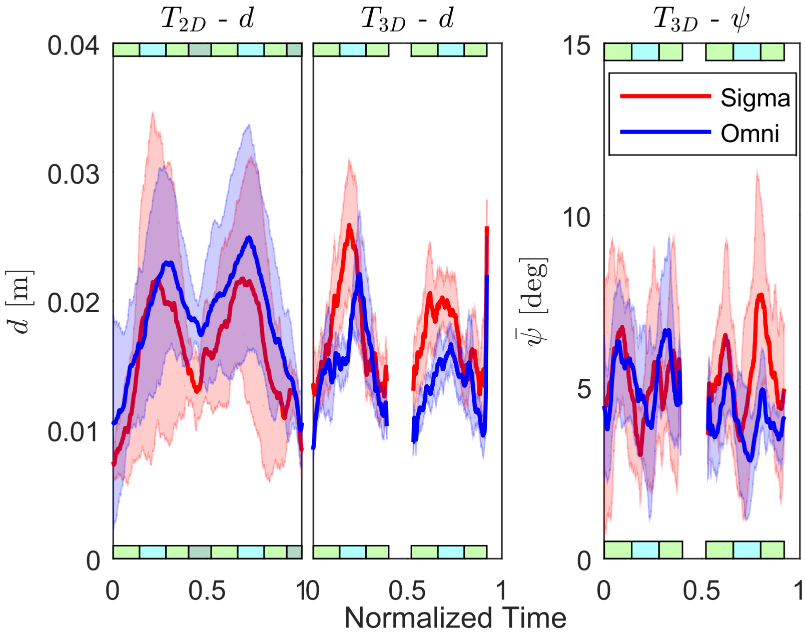

FIGURE 2.6: Error metrics (d and ψ) mean and standard deviations for T_{2D} and T_{3D}. In red the hybrid parallel-serial link master device (Sigma) and in blue the serial link master device (Omni).

TABLE 2.3: Pearson's correlations coefficients between R_v and d or ψ. All the ρ are significant ($p < 0.001$)

	T_{2D} - d		T_{3D} - d		T_{3D} - ψ	
User	Sigma	Omni	Sigma	Omni	Sigma	Omni
1	-0.18	-0.46	0.35	-0.14	0.35	-0.09
2	-0.75	0.58	-0.51	0.11	-0.51	0.36
3	-0.18	0.11	0.07	-0.26	0.07	0.14
4	-0.79	-0.86	-0.01	-0.12	-0.01	0.42
5	-0.52	-0.14	-0.22	0.18	-0.22	0.30
6	-0.49	-0.67	-0.45	0.18	-0.45	-0.28
7	-0.85	-0.77	-0.13	0.21	0.20	-0.16
Median	-0.81	-0.91	-0.45	-0.05	0.11	0.46

significant difference was found between the master devices, and users achieved the best performance in the positional task while maximizing the arm redundancy exploitation.

2.4.1 Redundancy Exploitation

HP1: *R_v modulation* - We first analyzed the R_v modulation through the two tasks paths, and found a significant modulation of R_v for T_{2D}, but a constant level of redundancy exploitation for T_{3D}. While no modulation in the redundancy exploitation was found for free-hand reaching movements [140, 123], more recent studies showed significant changes in the mean R_v values with respect to the movement direction during planar teleoperated reaching task [126]. Nisky et al. observed a small reduction in the level of redundancy exploitation in the central part of reaching movements, and this trend is particularly clear for novices in free-hand and teleoperated task execution. Expert teleoperators, instead, showed flatter R_v profiles, especially while teleoperating similarly to what was observed in T_{3D}. However, the substantial differences between the traditional tasks and the eight-shaped path that we investigated in the current study, make it very difficult to compare our results with the existing literature. The task that we analyzed is more complex with respect to traditional reaching movements, and following each point along the path requires continuous changes in the direction of movement. Moreover, during the eight-shaped task execution, users relied on visual feedback, and the task required precision along the entire path, rather than just the endpoint in reaching. This required and allowed for on-line adjustments and corrections that are absent during faster goal-oriented reaching and pointing tasks.

The results of T_{2D}, showed that users were maximizing the redundancy exploitation especially around the task's starting point rather than trying to compensate for the path's different movement directions or curvatures. It seems that, in T_{2D}, users weren't capable of maintaining high levels of arm redundancy exploitation adapting to the different part of the path, instead, freezing to the initial kinematic solution, their redundancy exploitation performance decreased as they moved away from the starting point [143]. A reason that could explain this behavior can be found in the fact that, at the beginning of each repetition, users were able to freely reconfigure their arm position and orientation to adopt the kinematic solution that best fitted the starting position. As users moved away from the starting point, their capabilities in exploiting the arm redundancy decreased.

On the other hand, the R_v modulation in T_{3D} is flatter: in this task, users were allowed to reconfigure their arm position as well as the end effector orientation after the first half of the path. This could have contributed to the increase in the users' capabilities in maximizing R_v. While performing T_{3D}, users were able to maximize the ratio between the task irrelevant manifold and the task relevant manifold associated with the end-effector x-y position to a higher extent with respect to T_{2D}. On the other hand, analyzing the differences between the $\bar{R}_v$ profiles within the first half of the path, it is clear that the the possibility of reconfiguring the arm pose in correspondence with the path's open ends can't be the only factor that modified the users' redundancy exploitation. Reasons to explain the $\bar{R}_v$ flatness in the first half of T_{3D} must, therefore, lie in the task constraints and characteristics.

HP2: *Differences between master devices* - Regarding the hypothesis of differences in the R_v modulation introduced by the two master devices architectures, apart from an offset between the two profiles, in both T_{2D} and T_{3D}, Sigma and Omni allowed for very similar trends. This result suggests that the variation in the redundancy exploitation through the path isn't affected by the different master devices dynamics that are eventually even-out by the CNS. Looking at the mean distributions, the differences in the R_v between the two master devices tested are non-significant. Nevertheless, trends can be seen in both tasks and, interestingly, while in T_{2D} the Omni master device shows higher values of $\bar{R}_v$, in T_{3D} the difference direction is opposite; in both cases, the differences in the mean values are hidden by large between users' variability. Previous studies showed that the manipulators' dynamic proprieties can influence performance and control strategies with respect to free-hand and unconstrained motion [126], [144]. Despite the mechanical and dynamical differences between Sigma and Omni, our results suggest that the differences in the kinematic solution adopted by users may require higher statistical power to be investigated. On the other hand, differences in the master devices could also be evened out by dynamic adaptation (as described in [105]) that would allow for similar R_v modulations and mean values. Further analysis should focus on the possibility of testing users' capabilities in adapting to multiple different master device's dynamics, trying to understand which differences can are compensated.

HP3: *Influence of task constraints* - We showed that no significant differences were found between the mean R_v estimated with the Analytical Jacobian ($J_{2D,A}$) and the one obtained with the least square regression ($J_{2D,LSQ}$) when the same task space dimension is compared (x-y end-effector position). This result confirms that the two Jacobian estimations are similar [142].

Significant differences between task space dimensions were found in the mean R_v in T_{3D} when the end-effector orientation is considered in the task space. $J_{3D,LSQ}$ is therefore capable of accounting for the additional portion of joint variability that users were employing to minimize the angular displacement between the tool end-effector direction and the tangent to the path. Similar results were observed in pistol shooting [130] and golf swing [131] experiments: users were utilizing part of the joint variability to finely control the tools orientation rather than its sole position. On the other hand, contrary to previous studies [131, 133], the level of redundancy exploitation is constant through the task execution. This is likely because our tracing task requires a continuous control over the tool orientation, whereas golf and table-tennis players must coordinate their arm kinematics especially when the club/racket hits the ball.

Comparing the $\bar{R}_v$ between T_{2D} and T_{3D}, it appears that users were able to elicit higher levels of redundancy exploitation when performing the most challenging task. This surprising result may have several explanation: it is possible that users, being more challenged by the second task, were also more inclined to explore a higher number of possible kinematic solutions. This difference in the level of task redundancy exploitation could be also related with the higher intrinsic motivation that users experience when challenged with a more complex motor task [145, 146, 147].

2.4.2 Error metrics

The results of the error metric analysis showed that users performance changed through the path. These changes are especially evident in the positional error, that shows similar behaviors for both master devices. Similarly to R_v, the positional error increases while moving away from the initial point, reaching its peaks in the straight and low curvature parts of the path. Regarding the orientation error (ψ), as expected, users committed the smallest errors when teleoperating in the straight parts of the task where the changes in the tangent to the path are limited.

Interestingly, no significant differences were found between the errors, both positional and orientational, that users committed using the hybrid parallel-serial master device (Sigma) and the serial one (Omni). Although being characterized by significantly different structures, dynamics and costs, the users' performance with the two master devices are comparable. A reason for this could be found in the fact that the tasks studied weren't complex enough to stress the capabilities of each master device.

The results of the correlation analysis showed that different users adopted different strategies to limit the positional and orientational error, both for T_{2D} and T_{3D}. On the other hand, looking at the correlations between mean R_v and mean d, it seems that, regardless of the master device used, when users showed the maximal redundancy exploitation, they also committed the smallest positional errors. The same ability to increase the ratio between TIM and TRM without deteriorating task performance was observed also in expert stone knappers [148], music players [149] and golfers [150]. This trend, which is particularly evident in T_{2D}, is absent in T_{3D}. In this case, the lack of variation in R_v, as well as in the performance metrics may have limited the capabilities of finding correlations. Moreover, the mixed positional and orientational constraint introduced in T_{3D} may have influenced the strategies that users adopted during teleoperation, leading to more complex relations between the task space performance metrics and the redundancy exploitation.

The strong correlation between performance and arm redundancy exploitation is a clear sign of the importance of this motor property: advantageous master devices should not limit or modify arm kinematics. On the other hand, modern teleoperation consoles, such as the one adopted in the Da Vinci Robot, employ arm rests to increase user comfort and reduce muscular fatigue. While laying the forearm on the armrest, surgeons might limit their capabilities in finding the arm configuration that would allow for the maximization of the ratio between task unrelated and task related variability. Future studies are needed to consider the possible tradeoffs in using armrests, including fixed and dynamic support [151]

2.4.3 Limitations and future work

An important limitation of the UCM approach is the coordinate sensitivity of the computational procedures that define the task relevant and irrelevant manifolds [121]. The structure of the observed variability is defined in a coordinate space which is arbitrarily selected by the researcher among multiple others. For example, in arm joint variability, choosing absolute or relative angles to describe the joints can yield to different results. When the structure of variability is evaluated in the result space defined by the task, i.e. using the TNC analysis, a sensitivity to changes in the coordinates frame exists, but is far less severe [121].

To solve these issues, a coordinate-independent formulation of the UCM analysis was recently proposed [122]. Campolo et al. exploited a particular type of kinetic energy metric originally proposed in [152] to study the level of redundancy exploitation during a static pointing task performed with an hand-handled tool. The choice of a left-invariant metric, which is independent from the frames used to describe the tool kinematics, allowed to estimate a coordinate-independent level of redundancy exploitation in a static task. This successful extension of the UCM analysis was applied to date to static tasks only, and future studies are needed to adopt this promising framework to the analysis of dynamic tasks such as following a path (tracing) or a trajectory (tracking).

In the present work, we performed a comparative analysis of different tasks and conditions, with the aim of underling the effects of different master interfaces and tasks constraints rather than striving to obtain absolute estimations of the level of redundancy exploitation. We, focused on expanding the existing literature regarding the effects of mixed positional/orientational constraints over arm redundancy, exploiting analytical techniques that have been already employed for non-static tasks [153, 154]. While coordinate-dependency still represents a non-negligible limitation of the present work, the comparative nature of the analysis should make it less sensitive to changes in the joints reference frames. Future studies are needed to develop a coordinate-independent metric similar to [122] that would be appropriate for our current task and for future studies with surgical tasks.

Another limitation of our study is its power. The number of users that took part in the experiments was small which reduced the statistical power of some of the analysis conducted. Further studies should therefore focus on extending the analysis to a higher number of participants. Moreover, the reduced number of subjects limits the strength of the analysis against the effect of human factors during the experiment: the differences in users' patience and personalities, as well as their different levels of stress or tiredness might significantly affect the data.

The absence of differences in terms of both performance and redundancy exploitation between the master devices tested should be further analyzed. First, in order to study how users cope with substantially different kinematics, ergonomics and workspaces, it would be interesting to extend the analysis to other master devices (i.e. the Da Vinci master console). Moreover, it would be interesting to evaluate how the use of an arm rest would affect users capability of exploiting arm redundancy. Secondly, the introduction of more complex tasks, characterized by higher task space dimensions, would allow to stress the effects of the different kinematic and dynamic characteristics on the motor strategies adopted by the users. The methods adopted in the present work could also be used to estimate how the additional task space dimensions would modify the users' redundancy exploitation.

Additionally, in the present work, no differences were found among users, who were all novice teleoperators. Previous studies showed how experienced and novice users adopt different arm redundancy exploitation strategies. Therefore, it would be interesting to study how users with different levels of familiarity and skills in teleoperation would cope with differences in the task constraint and task space dimensions. Moreover, the possibility of having multiple experimental sessions for each user, would allow to apply the UCM analysis to study how the level of redundancy exploitation changes throughout the learning process.

2.5 Conclusion

We used the UCM analysis to explore the differences induced by diverse task space dimensions and constraints and two master devices on teleoperators capabilities on the exploitation of the arm redundancy. We validated different algorithms to estimate the Jacobian matrix associated with the motion, and found significant differences between different tasks space dimensions. We found that users maximized the ratio between task irrelevant and task relevant variability especially in the more complex task, characterized by positional and rotational task space variables, regardless of the mechanical differences in the type of master device. Moreover, during the execution of the 2D task, users showed the lowest positional error while maximizing their arm redundancy, showing a positive correlation between performance and redundancy exploitation.

The present work represents a first step towards an in depth understanding of the mechanisms that regulate motor control during the execution of complex teleoperation tasks. The results showed how, for the tasks studied, substantially different master devices led to similar outcomes both in terms of performance and arm redundancy exploitation and how teleoperators can take advance of an additional portion of arm redundancy during mixed positional-orientational tasks.

Acknowledgment

This project has received funding from the European Union's Horizon 2020 research and innovation programme under grant agreement No. H2020-ICT-2016-732515 and from the Helmsley Charitable Trust through the ABC Robotics Initiative, by the Marcus Endowment Fund both at Ben-Gurion University of the Negev, and the ISF grant number 823/15

Chapter 3

Analysis of joint and hand impedance during teleoperation and free-hand task execution

In this chapter the estimation of hand stiffness modulation during the execution of a simulated suturing task is presented. Two different master devices, and free-hand movements are studied and compared. Kinematic data of eight right-handed users are acquired, using electromagnetic and optical tracking systems, and analyzed using a musculoskeletal model. Through inverse dynamics, muscular activation are computed and used to obtain joint torques and stiffness, leading to end-point stiffness estimation. The maximal stiffness value and its angular displacement with respect to the trajectory tangent was computed. The results show that there is a difference in how the main stiffness axis was modulated by using the two master devices with respect to free-hand, with higher values and variability for the serial link manipulator. Moreover, a directional modulation of the hand stiffness through the trajectory was found, showing that the users were aligning the direction of the main stiffness axis perpendicularly to the trajectory.

This work has been published as: Buzzi, J., Gatti, C., Ferrigno, G., & De Momi, E. (2017). "Analysis of joint and hand impedance during teleoperation and free-hand task execution", *IEEE Robotics and Automation Letters*, 2(3), 1733-1739.

3.1 Introduction

Robot-Assisted Surgery (RAS) is achieving great outcomes and feedbacks [155]. Thanks to its advantages, such as augmented precision due to movement and force scaling, hand tremor and chopstick effect compensation [6], this technology has widely spread in the last decade. During teleoperated robotic surgery, the user interacts with a master controller that detects the position and motion of his/her hand and sends it to the slave robot. In comparison with traditional laparoscopic surgery, in which the tools usually have rigid shafts constrained to approach the surgery area from the direction of the incision, thus limiting the surgery tool mobility, the mechanical characteristics of the tools developed for robotic surgery allows for the reproduction of the human wrist mobility. These mechanical differences are reflected in substantial kinematic and motor control differences that lead to limited correlation between laparoscopic expertise and robotic surgery skills [156].

To be able to fully exploit the potential of this technique [157] and take advantage of the tools high dexterity (the capability of changing the position and orientation of the manipulated objects to every arbitrary chosen pose), surgeons have to undergo a long and intensive training phase [158]. During this process, teleoperators have to familiarize with the new environment, by means of, for example, compensating for the absence of haptic feedback [159] or learning how to fully exploit the 3D visualization. Researchers are trying to restore the lack of force feedback from the tool tip to the surgeon hand using different strategies [160, 161], involving kinesthetic feedback [162], generating guiding forces [163] and actively changing the manipulator characteristics to help the surgeons [100, 93]. While these studies will help in narrowing the gap that exist between free-hand and teleoperated surgery [164], a better understanding of the kinematic and kinetic strategies that define the human interaction with the master controller could potentially suggest new solutions to improve the surgeon's experience.

Teleoperation is a challenging task for the human motor control system, encompassing the management of the intrinsic redundancy of the neuro-muscular-skeletal system. In fact, from a kinematic standpoint, the human arm can be modeled as a seven degrees of freedom (DoF) redundant manipulator, which allows to theoretically assume infinite joint configurations to achieve the same hand position and orientation. Moreover, from a kinetic standpoint, a large set of muscular activations produce the same motion, but involving different levels of arm stiffness. The different ways the central nervous system manages these redundancies are decided by human motor control strategies.

A promising approach in the study of the teleoperators' kinematic redundancy has been recently presented by Nisky et al. [101], [165]. The authors studied the arm joint configuration in repeated reaching tasks performed with the Da Vinci Si surgical system (Intuitive Surgical, Mountain View, California) and in free-hand, comparing not only the task precision performance in terms of end-effector control, but also the arm configuration variability. Through the Uncontrolled Manifold (UCM) analysis the authors were able to distinguish between two joint variability components: one that helped the expert users in hand stabilization and another that captured residual noise. Using the UCM analysis, the authors were able to weight the users' joint variability into task relevant and irrelevant manifolds, showing that experienced surgeons were able to maximize the ratio between task-irrelevant and task-relevant variability.

The central nervous system, while handling kinetic redundancy, is able to control the mechanical impedance of the arm also through mechanisms as muscle co-contraction. Teleoperation is usually characterized by slow and precise movements that can be divided in subsequent joint configurations, each characterized by a mechanical impedance dominated by stiffness.

Several studies measured the arm stiffness resulting from small hand displacement in stationary and dynamic conditions [166],[167], underlying the body capabilities of restoring a desired configuration after being subjected to external perturbation. Stiffness is a measure of arm stability against noise and perturbation and its modulation has been studied during the execution of multijoint tasks requiring accuracy [168][169]. Other researches [170] also found that the arm stiffness decreases during multiple executions of the same tasks as far as the users learn. These results suggest that stiffness and, more in general, impedance control is a key factor in the process of learning and mastering the execution of a specific task.

Previous studies obtained the arm end-point stiffness applying known displacements to the subjects hand using robotic handles and acquiring the force exchanged by the hand with the robotic handle [171] [172]. Others evaluated the arm stiffness by analyzing surface EMG activity of antagonist muscles [75]. In our study we propose a comparison between the arm end-point stiffness computed using musculoskeletal models during the execution of a 3D task with different master devices in teleoperation and in free-hand. Using free-hand as a reference of the most natural and transparent controlling strategy, stiffness values and principal direction were compared and correlated with the task execution performance.

3.2 Materials and methods

3.2.1 Task

The task was designed with the aim of recreating the wrist movement performed during suturing, where the needle is inserted through the tissues with a wrist rotation. Users were asked to follow an U-shaped trajectory with a ring-terminating tool and to sweep the ring on the path while keeping the ring centre as more aligned as possible with the trajectory. The shape and length of the path were grossly estimated reaching a compromise between wrist activation and task feasibility.

1. *The Virtual Task*

Fig. 3.1(a) shows the virtual trajectory: the starting point, in the rightmost position of the trajectory, is marked with a green sphere, the user had to reach the red sphere on the left. During the task execution, users were given visual feedback which consisted in a change of the trajectory color based on the distance between the center of the tool ring and the trajectory: from light green, when the trajectory is in the middle of the ring, to red, when a collision was detected.

The virtual task was developed using V-Rep (Coppelia Robotics GmbH, Zürich, Switzerland), a robot simulation program that can be interfaced through the Robotic Operating System (ROS) [173] network with the master devices involved in the test and with the data acquisition framework.

2. *The free-hand Task*

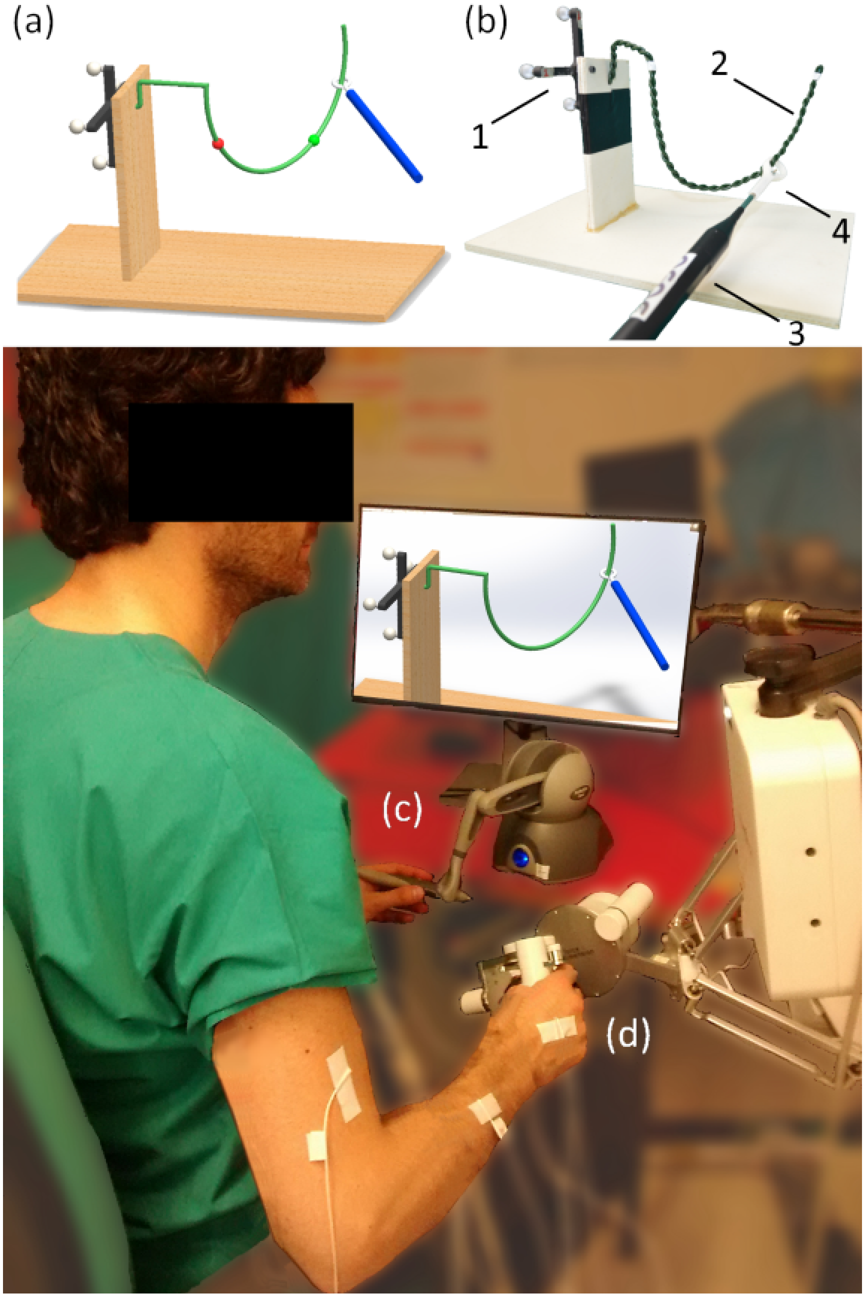

[redacted]

FIGURE 3.1: The complete setup: (a)The virtual reality trajectory. (b) The free-hand task: 1. Base 2. Metal wire trajectory 3. EMT Pointer 4. 3D Printed ring end-effector (c) The serial link master device (SL). (d) The parallel link master device (PL).

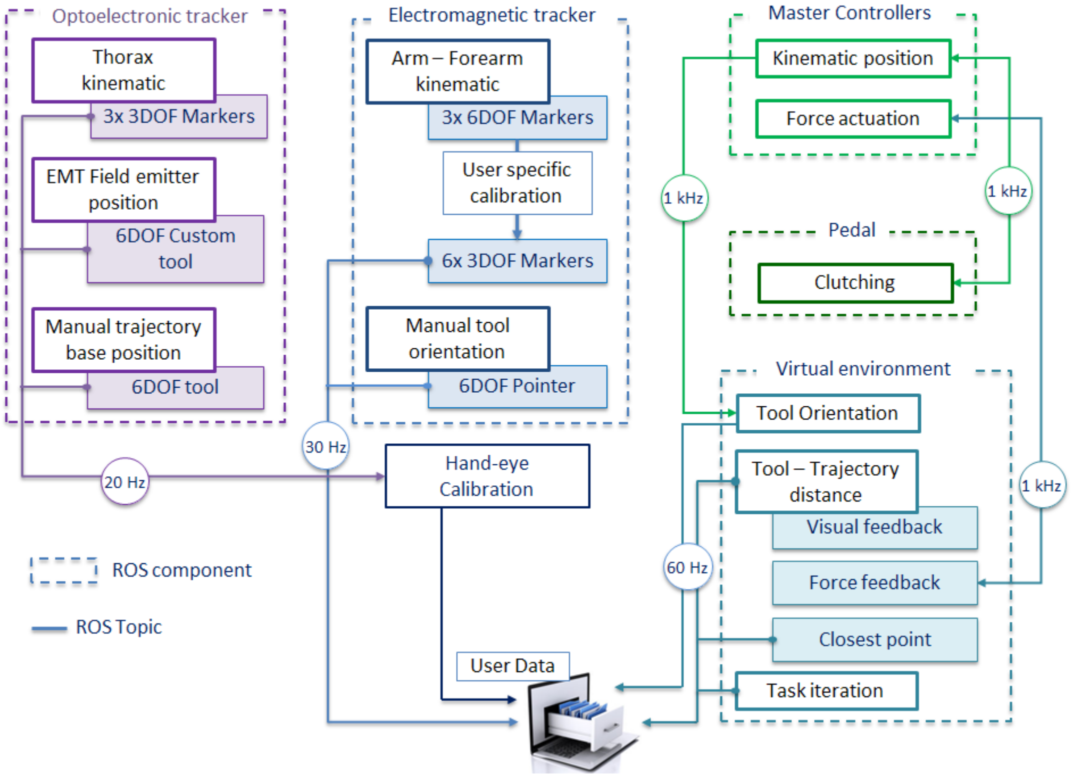
Optoelectronic tracker
Thorax kinematic
3x 3DOF Markers
EMT Field emitter position
6DOF Custom tool
Manual trajectory base position
6DOF tool
Electromagnetic tracker
Arm – Forearm kinematic
3x 6DOF Markers
User specific calibration
6x 3DOF Markers
Manual tool orientation
6DOF Pointer
Master Controllers
Kinematic position
Force actuation
Pedal
Clutching
1 kHz
1 kHz
30 Hz
20 Hz
Hand-eye Calibration
Virtual environment
Tool Orientation
Tool – Trajectory distance
Visual feedback
Force feedback
Closest point
Task iteration
1 kHz
60 Hz
ROS component
ROS Topic
User Data

FIGURE 3.2: The acquisition framework: each hatched box represents a ROS component that is responsible of streaming or monitoring a specific kind of signal. The arrows depict the ROS topic connecting each component and the acquisition frequencies are reported into the overlying circles

In order to recreate the same task for the free-hand movements, the trajectory was realized using a wooden base and coated metal wires that were shaped to assume the same dimensions and shape of the virtual one . The user performed the task using a tracked fast prototyped tool with the same dimensions as the virtual one (see Fig. 3.1(b)).

3.2.2 Experimental protocol

Eight users (3 males, 5 females, 24 ± 1.3 year old) were recruited during the experimental campaign; all of them were right-handed novices with no surgical experience and no previous experience with haptic interfaces or teleoperation. This study was carried out in accordance with the recommendations of our institution with written informed consent from the subjects in accordance with the declaration of Helsinki. Each user performed 10 repetitions of the task with three control modalities:

1. Parallel Link robot (PL)
2. Serial Link robot (SL)
3. Free-hand (FH)

The users were given information about how to control the device and about the visual and haptic feedback that they were going to receive. In PL and SL the users had 5 to 15 minutes to gain a sufficient acquaintance with the control and with the virtual environment. The differences in the initial training time were introduced to account for the slightly different learning curves that users showed: while some users were capable of completing a test repetition without unacceptable errors in a brief time, others required multiple trials to achieve the minimum level of familiarity with the master device. During FH, the initial training time was limited to about 1 minute.

In PL, SL and FH, the users were instructed to find a compromise between task execution time and accuracy.

3.2.3 Master devices

To control the tool position and orientation in the virtual reality, two haptic devices were used. In both cases the use of a clutch was adopted to enlarge the robots' workspace. For both master devices a scaling factor of 0.5 was applied to the hand movement for the reconstruction of the tool position in the virtual scenarios. The Phantom Omni (3D Systems, South Carolina, USA) haptic device (Fig. 3.1(c))(workspace 160x120x70mm) was used as SL. The device is characterized by six DoFs with a stylus end-effector. The device is not gravity compensated and has a resolution of 0.055mm. An external pedal was used as clutch. As a controller, we used a custom developed impedance controller [79] based on the proprietary API. For PL, a gravity compensated Force Dimension Sigma.7 (Force Dimension, Nyon, Switzerland) haptic device (Fig. 3.1(d)) (workspace $\oslash$190x130mm) was used. The robot is characterized by 6+1 DoF delta based parallel kinematics with hand-centered rotation, it has a resolution of 0.0015mm and 0.013deg. An external pedal was used as a clutch. The device used the proprietary impedance controller.

3.2.4 Acquisition architecture

A custom data acquisition framework was developed to acquire, synchronize and record the different signals. Fig. 3.2 shows the ROS based acquisition framework, which allowed to assign a network timestamp at each sampled signal.

The component functionalities were monitored through a simple graphic interface, and they were running on three different computers, all based on Ubuntu 14.

The position of the arm was measured using an electromagnetic tracker (EMT) (Aurora - Northern Digital, Ontario, Canada, 30Hz sampling rate, 0.48mm and 0.3deg position and orientation RMSE, 500mm dome shaped radius workspace). The system tracks four 6 DoF 1.8x9mm sensors.

Due to its limitation in both the maximal number of electromagnetic markers and the field dimension, the EMT system was coupled with an optical localization system (OPT) (Vicra - Northern Digital, Ontario, Canada, 20Hz sampling rate, 0.25mm position RMSE) that was used to acquire the thorax position. Three passive retroreflective markers were attached to the right and left acromions and beside the jugular notch. In order to register the data from the two tracking devices (EMT and OPT) an hand-eye calibration [135] was used. In order to perform the registration, a OPT tool (REF) was attached to the EMT field emitter. The homogeneous matrix that were computed, ${}^{REF}\mathbf{T}_{EMT}$, maps the transformation that brings the EMT reference frame on REF reference frame (see Fig. 3.3).

In the teleoperated tasks (PL and SL), the distance between the tool center and the closest point on the trajectory was computed in the virtual environment. In order to obtain this metric also in FH, an OPT tool (*Base*) was fixed to the wooden base at which the metal trajectory is rigidly connected (see Fig. 3.1(b)-1). 50 Points on the trajectory were acquired using the OPT pointer, and these coordinates were interpolated with a second order polynomial. The tool ring center was recorded using an EMT pointer (see Fig. 3.1(b)-3) directly handled by the user terminating with a 3D printed ring tool (see Fig. 3.1(b)-4).

In order to be able to integrate the markers data with the musculoskeletal modeling software, during patient calibration, we created virtual markers from the the electromagnetic sensors connected to the arm, forearm and hand segments (see Fig. 3.3).

Eq. 3.1 describes the homogeneous transformation matrices that were used during the acquisition.

$$ {}^{Real}\mathbf{T}_{Virt} = ({}^{EMT}\mathbf{T}_{Real})^{-1} \cdot {}^{EMT}\,\mathbf{T}_{Virt} \tag{3.1} $$

$$ {}^{EMT}\mathbf{T}_{Virt} = {}^{EMT}\,\mathbf{T}_{Real} \cdot {}^{Real}\,\mathbf{T}_{Virt} \tag{3.2} $$

where ${}^{Real}\mathbf{T}_{Virt}$ is the transformation matrix that maps the virtual markers in the real markers reference frame, ${}^{EMT}\mathbf{T}_{Real}$ is the transformation matrix that maps the real markers in the EMT reference frame and ${}^{EMT}\mathbf{T}_{Virt}$ is the transformation matrix that maps the virtual markers in the EMT reference frame.

3.2.5 The musculoskeletal model

The subject musculoskeletal model was implemented in OpenSim [139]. The model derives from a 15 DoF model from Holzbaur [138] whose hand grip and fingers kinematic were fixed, simplifying it into a 7 DoF model. Its performance in the dynamic prediction were previously demonstrated. [137]. The model is characterized by 50 Hill-type muscle-tendon actuators, simulating 32 muscle compartments. To fit the data from the different users that participated in the research, the model was scaled accordingly with the anthropometric characteristics, also adapting the different segments mass proprieties.

The inverse kinematic reconstruction was carried on using the markers trajectories filtered with a second order low pass Butterworth filter at 4Hz. The inverse

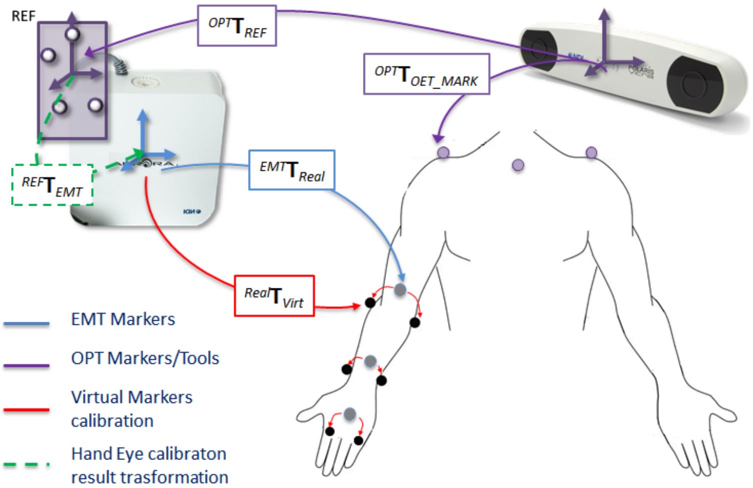

FIGURE 3.3: Markers setup: gray points represent EMT markers position, i.e. arm, forearm and hand; black points are the virtual markers created during the calibration phase during which the EMT pointer tool was used to touch two recognizable bony landmarks on each arm segment, while a custom ROS component acquired the transformation that mapped the touched point in the EMT marker reference frame of the corresponding segment (${}^{Real}\mathbf{T}_{Virt}$). Arm and forearm sensors were connected to lateral and medial repere point of elbow and wrist respectively; the hand virtual sensors were placed on the index and little finger's knuckle.

dynamic reconstruction was performed with the joint kinematic data from the inverse kinematic solution, filtered with the same 4Hz low pass filter. The simulations were performed on an i5 4670k processor, operating at 3.8Ghz with 16Gb of DDR3 memory.

3.2.6 Stiffness computation

Based on the analysis performed with OpenSim, the joint torque matrix **Kj** for each arm configuration during the task execution was computed. The $(k \times k)$ joint stiffness matrix for the i^{th} sample of the acquisition can be defined as follows [174]:

$$\mathbf{Kj}_i = \frac{d\boldsymbol{\tau}_i}{d\mathbf{q}_i} \tag{3.3}$$

$\boldsymbol{\tau}_i$ is the $(k \times 1)$ vector that represents the joint torques for the $\mathbf{q}_i$ vector of joint angles and k is the model's number of joints.

The joint torques vector is defined as:

$$\boldsymbol{\tau_i} = \mathbf{Jm}_i^T \cdot \mathbf{Fm}_i \tag{3.4}$$

$\mathbf{Fm}_i$ is the $(m \times 1)$ vector of the muscle activations (with m number of muscular units in the model) at the i^{th} sample, obtained from the inverse dynamic analysis in OpenSim and $\mathbf{Jm}_i$ is the muscle Jacobian at the i^{th} sample, computed as follows:

$$\mathbf{Jm}_i = \begin{pmatrix} \frac{\partial l_{1,i}}{\partial q_{1,i}} & \frac{\partial l_{1,i}}{\partial q_{2,i}} & \cdot & \frac{\partial l_{1,i}}{\partial q_{k,i}} \\ \frac{\partial l_{2,i}}{\partial q_{1,i}} & \frac{\partial l_{2,i}}{\partial q_{2,i}} & \cdot & \frac{\partial l_{2,i}}{\partial q_{k,i}} \\ \cdot & \cdot & \cdot & \cdot \\ \frac{\partial l_{m,i}}{\partial q_{1,i}} & \frac{\partial l_{2,i}}{\partial q_{2,i}} & \cdot & \frac{\partial l_{m,i}}{\partial q_{k,i}} \end{pmatrix} \tag{3.5}$$

The muscular Jacobian matrix, $\mathbf{Jm}_i$, relates the variations in muscle length $\mathbf{l}_i$ with the variations in joint angular position $\mathbf{q}_i$ and can also be seen as the muscle forces moment arm matrix.

In order to study the stiffness characteristics and to create a graphical representation in the Cartesian space, the joint stiffness matrix at the i^{th} sample was converted into the end-effector stiffness matrix $\mathbf{Ke}_i$ using the corresponding Jacobian matrix $\mathbf{J}_i$ that relates infinitesimal changes in the Cartesian space into infinitesimal changes in the joint space.

$$\mathbf{Ke}_i = \mathbf{J}_i^{-T} \mathbf{Kj}_i \mathbf{J}_i^{-1} \tag{3.6}$$

Note that in Equation 3.6 the non squared 6×7 Jacobian matrix is inverted using the Moore-Penrose pseudoinverse. Due to the arm redundancy, the Jacobian matrix inversion can yield to multiple results: the Moore-Penrose algorithm finds the solution that involves the smallest Δq. This is a suboptimal solution, since different choice of generalized inverses would lead to different projections of the joint stiffness onto the end-effector space. In order to avoid this approximation, solutions have been adopted to estimate the stiffness nullspace which involve calibrations with constrained arm motions and predefined movements [175].

From the singular value decomposition (SVD) of $\mathbf{Ke}_i$ the translational stiffness property of the arm can be obtained at each arm configuration. The matrix $\mathbf{Ke}_i$ has three nonzero singular values that define the ellipsoids main axes dimension while the ellipsoid orientation can be obtained from the (3×3) left singular vectors [174].

3.2.7 Results analysis

Error

As a measure of the task execution performance, in PL and SL the distance (E) between the tool centre at the i^{th} sample ($\mathbf{C}_i$) and the closest point on the trajectory ($\mathbf{CP}_i$) was computed with a sampling frequency of 60Hz (see Eq. 3.7).

$$E_{PL,i} = E_{SL,i} = \|\mathbf{C}_i - \mathbf{CP}_i\| \tag{3.7}$$

where the norm indicates the Euclidean distance. In FH, through the registration procedure described in Section 3.2.4, the tool center position was computed with respect to the trajectory. In order to obtain the coordinate of the closest point on

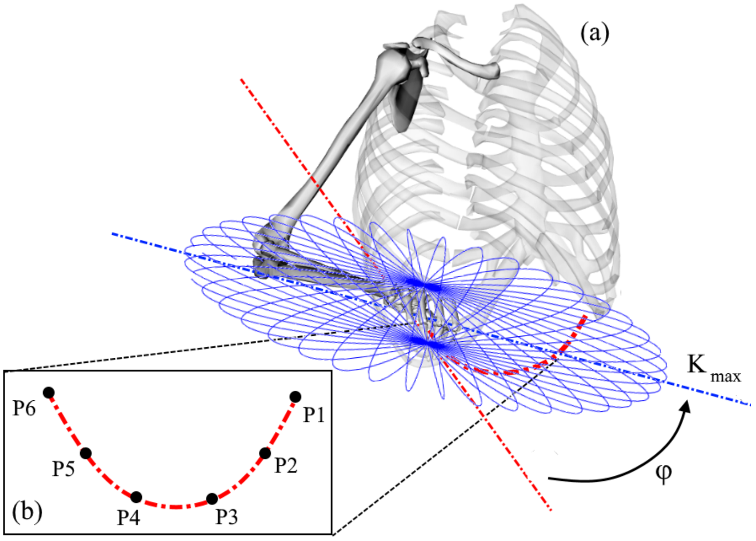

FIGURE 3.4: The computed ellipsoid (in blue) is overlapped to the muscoloskeletal model at a specific point on the trajectory (in red). (a) The main axis dimension K_{max} and its angle with the tangent to the trajectory φ are monitored through the different users task repetitions. (b) The six points along the trajectory

the free hand trajectory ($\mathbf{CPFH}_i$), the Quickhull algorithm [176] was used to find the closest point between the interpolated curve and each tool position $\mathbf{C}_i$ (see Eq.3.8).

$$E_{FH,i} = \|\mathbf{C}_i - \mathbf{CPFH}_i\| \tag{3.8}$$

The data distribution normality was tested using the Lilliefors test with a significance level (α) of 0.01. Since no significant difference was found in the error distribution among users (Kruskal-Wallis H test $\alpha = 0.001$), we grouped all the trials and users for each control modality into a single population. The differences between the three control modalities were evaluated through a post-hoc multivariate analysis using the Willcoxon rank sum test ($\alpha = 0.001$).

Stiffness ellipsoids - Main axis length

Fig. 3.4(a) represents the transactional stiffness ellipsoid obtained in FH task execution. The ellipsoid main axis length (K_{max}) was computed for six points ($P1 \sim P6$) along the trajectory (see Fig. 3.4(b)).

The population normality was tested using the Lilliefors test ($\alpha = 0.01$). Since no statistical difference was found between different users and repetitions (Kruskal-Wallis H test $\alpha = 0.001$), the K_{max} values for each point through the users and repetitions were grouped together. We grouped the data from the six point along the trajectory together, evaluating the statistical differences between the three control modalities using multiple Willcoxon rank sum tests ($\alpha = 0.001$).

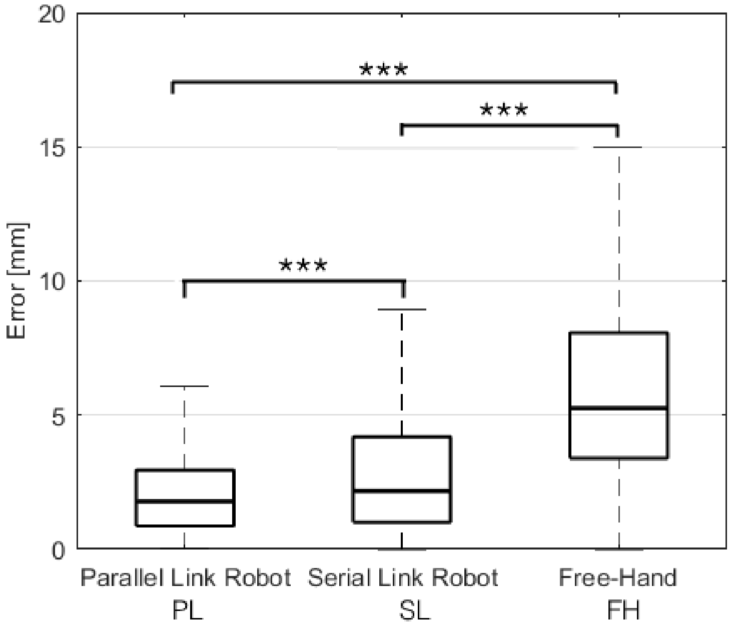

FIGURE 3.5: The error metric in PL, SL, and FH are reported as 25^{th} and 75^{th} percentiles and median values. The statistical difference between the control modalities is reported using horizontal lines. Three stars indicate $p < 0.001$

Stiffness ellipsoids - Angular displacement

The angle between the main axis and the tangent to the trajectory (φ) was computed for the same six points ($P1 \sim P6$). The value was computed obtaining the vector tangent to the desired trajectory in the six points and the vector representing the instantaneous end-effector direction of motion. Since no statistical difference was found between different users and repetitions (Kruskal-Wallis H test $\alpha = 0.001$), the angular displacement φ values for each point through the users and repetitions were grouped together. The existence of possible parabolic trends in the angular displacement through the trajectory was evaluated using a second order polynomial regression.

3.3 Results

3.3.1 Error

Fig. 3.5 shows the error data distribution in the three control modalities (PL, SL and FH). PL median error is statistically lower that SL and FH ($p < 0.001$). In general, teleoperation (PL and SL) allowed the users to execute the task with higher accuracy with respect to free-hand.

3.3.2 Stiffness Ellipsoids - Main axis length

Fig. 3.6 shows the distribution of the maximal end-point stiffness in the six trajectory points and the three controlling modalities. The results obtained show that, during

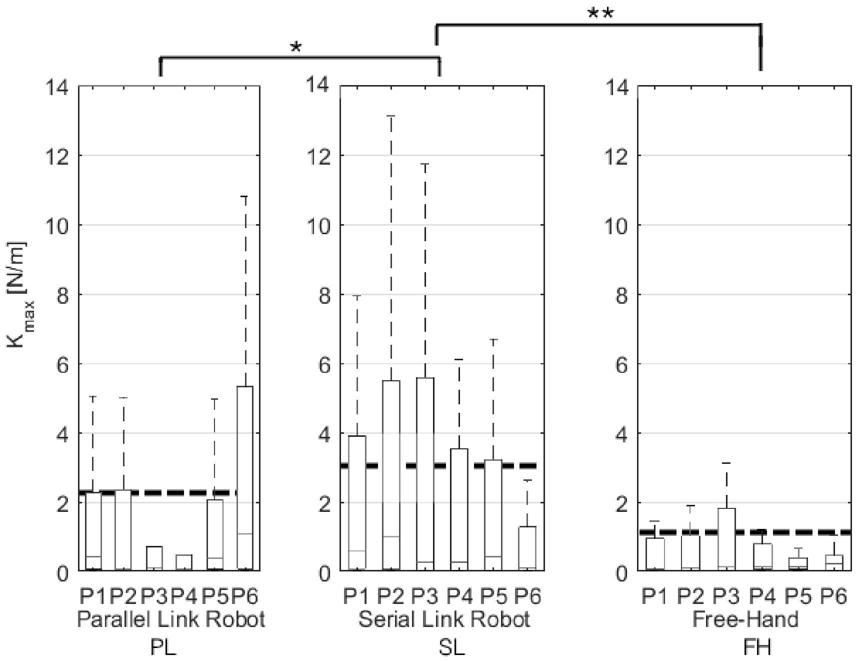

FIGURE 3.6: The maximal hand stiffness in the six points of the trajectory for the parallel link robot, for the serial link robot and for free-hand. Boxes indicate the 25^{th} and 75^{th} percentiles, vertical dashed lines indicate the maximal values and the horizontal dashed lines represent the median values of the three populations. The horizontal lines at the top of the graph describe the statistical difference between the control modalities when all the six points are considered together, as in Table I. One star correspond to $p < 0.05$, two stars to $p < 0.01$

tasks execution, a parabolic trend could be seen in all the control modalities: while for SL and FH the maximal values seems to be occurring for the central point of the trajectory (P3 and P4), this trend is opposite in PL, where at the central points of the trajectory correspond the smallest values of maximal stiffness.

Table 3.1 reports the stiffness maximal values K_{max} distributions for the six points grouped in the three control modalities. The median values are also reported as dashed lines in Fig. 3.6 (PL = 0.21 N/m, SL = 0.32 N/m, FH = 0.12 N/m).

The results show that SL maximal stiffness values are statistically higher from both PL (with a $p < 0.05$) and FH ($p < 0.01$).

3.3.3 Stiffness Ellipsoids - Angular displacement

Fig. 3.7 shows the evolution of the angle φ in the six points of the trajectory for the three control modalities. Analyzing the angular displacement results, a parabolic trend can be found in the median values obtained through the six points on the trajectory. The R-square indexes obtained for PL, SL and FH are respectively 0.32, 0.43 and 0.66 (Fig. 3.7 - dotted lines).

This behavior, which is particularly clear in the free-hand control, tends to align the stiffness main axis in order to make it perpendicular to the desired direction of motion in correspondence to P3 and P4, the central points of the trajectory.

TABLE 3.1: Maximal stiffness K_{max} in the three control modalities

	Parallel Link Robot **PL**	**Serial Link Robot** **SL**	**Free-hand** **FH**
Min:	0.00 N/m	0.00 N/m	0.00 N/m
25^{th} p.:	0.04 N/m	0.04 N/m	0.04 N/m
Median:	0.21 N/m	0.32 N/m	0.12 N/m
75^{th} p.:	3.60 N/m	4.00 N/m	0.71 N/m
Max:	5.55 N/m	8.73 N/m	1.45 N/m

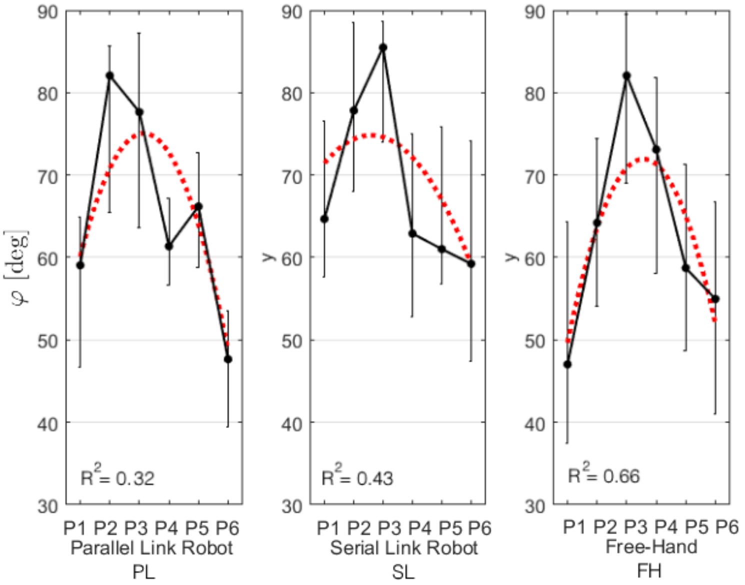

FIGURE 3.7: The angle between the maximal hand stiffness direction and the tangent to the desired trajectory in the six points for the three control modalities. The points represent the median values, while the vertical lines represent the 25^{th} and 75^{th} percentiles. The dotted line represents the second order polynomial regression, with the corresponding R^2 values associated.

3.4 Discussion

In this work we studied the arm end-point stiffness as a measure of the impedance control strategies adopted by the central nervous system to stabilize the hand movement in three tasks, in teleoperation, executed with two master devices, and in free-hand. A task mimicking suturing was realized in a virtual and real environment.

As expected, we found that the error metric results reflect the strength of the teleoperation scenario in reducing the influence of the hand control variability: the tasks error are smaller in teleoperation with respect to free-hand thanks to the motion scaling and the color feedback that was used to finely adjust the tool position.

By analyzing the results obtained in the K_{max} modulation, there are significant differences between the control modalities. In SL control modality only, the users were exploiting the pivoting stylus to execute the trajectory. In PL, instead, the rotations were hand centered, as in FH, where the dimensions of the tool and its weight discouraged the users from executing the task mainly activating the wrist joints. It is possible that the presence of this "*lever*" in SL forced the users to increase the arm stiffness to achieve good performance. This result suggests that hand-centered rotations in the manipulator allow the users to achieve statistically higher kinematic performances while eliciting lower arm stiffness. Since lower arm stiffness values are obtained with lower levels of muscular activation, hand-centered rotating master devices could reduce the users' muscular fatigue and should therefore be preferred. In order to further analyze this hypothesis, and understand how the use of a stylus end-effector might change the arm's dynamic, future work should try to isolate the differences between the studied master devices. In fact, substituting the existing stylus end-effector with a custom built replica of the hybrid parallel-serial gripper, it would be possible to study the effect of the differences in the master devices' dynamic only.

Regarding φ modulation, in FH the regression curve obtained is partially able to fit the data, suggesting the possible existence of a parabolic behavior. This behavior could be the result of a motor strategy that aims at maximizing the hand resistance to external perturbation that would directly influence the task execution while maintaining minimal stiffness in the direction of motion. The maximal values of φ are achieved in P3 and P4, where the users had to change their wrist configuration to follow the trajectory curvature; from this result it seems that the users were relying on the directional control of stiffness in particular in the most challenging part of the trajectory. If this evidence would be confirmed by more in depth researches, it would be possible to actively use the master devices' force feedback to increase the stiffness on the directions perpendicular to the motion, reducing the total muscular activation requested to the arm. Future works will also test the hypothesis of stiffness regulation with respect to motion direction in order to understand how the master devices design could influence the possibility of putting this motor strategy into practice.

The first limit of this work can be found in the high variability of the data related to the stiffness ellipsoids. Both the maximal stiffness K_{max} and the angular displacement φ suffer from high interquartile dispersion inter and intra users. A reason for this behavior could be found in the complexity of the tasks, that represents a difficult precision task, and presents different challenges for each user. In spite of the task being simplified from a previous set of acquisition, this variability, even though reduced, still persist. Further analysis should, therefore, focus on easier, more limited tasks that would force users to achieve and maintain similar kinematic strategies through their execution. For example, further studies should first analyze simple, non surgical, tasks such as reaching or tracing planar movements.

An other limitation can be found in the joint stiffness computation, that does not take into consideration possible voluntary muscle co-contractions.

Even though it presents some limitations, this study represent a novel approach to the study of the human robot interaction in teleoperation. The results obtained could be used as an optimization goal for the design of new master devices.

3.5 Future developments

Starting from this results, it would be desirable to extend the analysis to more subjects and more trajectories, creating task on different planes to test the users capability in modulating the hand stiffness orientation.

An interesting future development will be the comparison between the stiffness computation method presented in this work and other methods: for example, during the tasks execution, known external forces could be applied, acting as random perturbations on the users hand; the measured displacement induced in the hand position could be used to directly compute the hand stiffness. Another possible comparison could be done with the methods that use electromyography signals to evaluate the arm stiffness. It would also be interesting to acquire the electromyographic activation of the muscles that control the upper limb movements, performing a co-contraction analysis aimed at finding a physiological correspondence to the analytical stiffness modulation that was found.

3.6 Acknowledgements

This project has received funding from the European Union’s Horizon 2020 research and innovation programme under grant agreement No. H2020-ICT-2016-732515.

Chapter 4

On the value of estimating human arm stiffness during virtual teleoperation with robotic manipulators

In this chapter an extension of the non-disruptive method to study the arm endpoint stiffness is presented. Four users were asked to perform two planar trajectories following virtual tasks using both a serial and a parallel link master device. Users' arm kinematics and muscular activation were acquired and combined with a user-specific musculoskeletal model to estimate the joint stiffness from muscular fibers dynamics. The obtained results are in accordance with the existing literature in human motor control and show, throughout the tested trajectory, a modulation of the arm endpoint stiffness that is affected by task characteristics and hand speed and acceleration.

This works has been published as: Buzzi, J., Ferrigno, G., Jansma, J. M., & De Momi, E. (2017). "On the Value of Estimating Human Arm Stiffness during Virtual Teleoperation with Robotic Manipulators", *Frontiers in neuroscience*, 11, 528.

4.1 Introduction

Teleoperated robotic systems are widely used in several long-short range application fields, from plant decommissioning [177], environment exploration [178], hazardous material handling and surgery [96]. In order to control the remotely operated system, the user interacts with a master interface, a robot whose precise and accurate manipulation allows task execution at the slave side. The design of master interfaces is a fundamental aspect in teleoperation, indeed several studies focused on the master devices physical and control characteristics to achieve control transparency while assuring system stability [179], [180], [102]. In teleoperation, stability of human-robot interaction [181] is guaranteed by closing the control loop with the user sensory and motor systems and, in this context, both the robot and the user are considered as passive elements [182]. Therefore, although the design of master devices architecture relies on the human user to achieve stability, the high variability that characterizes human control strategies are usually neglected. In fact, in human motor control, task stability is achieved by regulating the dynamic proprieties of the limbs through muscular activation. The arm impedance and its components (viscosity, inertia and stiffness) can be modified to adapt to different tasks and desired interactions by tuning muscle contractions and varying joint angular position, . As the most predominant component, the arm stiffness also directly depends on the joint angular velocity, reflex modulation and the presence of expected perturbations [132]. Previous studies [183] demonstrated the existence of control strategies employed to achieve stability through the regulation of the arm endpoint stiffness in terms of maximal value and orientation. Other studies showed the importance of stiffness regulation during complex tasks execution and motor learning [184, 185, 105].

Up to now, the dynamic proprieties of the human arm have not been fully considered in the control and optimization design of the master interfaces [186, 187]. Through robust and continuous estimation of arm stiffness, it would be possible to implement a master controller able to adapt and regulate the physical interaction between the robot and the human [90, 39] in order to achieve better performance, higher resistance to external perturbations, and possibly reducing muscular fatigue [188].

In order to estimate the human arm stiffness, several methods and devices have been proposed in literature: Flash and colleagues [132] as well as Gomi et al. [172] used planar robotized handles fitted with force sensors to record the interaction forces between the subjects' hand and the robot when known displacements were applied. Force and displacement variations were used to compute hand stiffness in multiple directions. While these methods produce a measurement of the stiffness during postural maintenance, they cannot be applied to the study of stiffness during movement and task execution without interfering with arm kinematics. To overcome this limitation, microscopic displacements combined with a time frequency analysis were used to estimate the mechanical proprieties of the arm during a single reaching movement [189]. Following an electromyography (EMG) based approach, recent works [171, 75, 76], estimated the arm endpoint stiffness using simplified planar musculoskeletal models and recorded surface muscle activations from couples of shoulder and arm antagonist muscles. Muscular models were used to estimate the force direction and arm of muscular units, while force intensities were obtained through calibration from the recorded EMG signals and the maximal voluntary contractions. Although the simplified musculoskeletal models showed the ability to estimate the arm endpoint stiffness during task execution and without applying perturbations to the user kinematics, stiffness computation was limited to specific planes and directions thus neglecting the effects of other couples of muscles, such as the wrist flexor/extensors.

In this work, we present a non-disruptive method for the computation of the arm endpoint stiffness based on a user specific 7 degrees of freedom (DoF) musculoskeletal model of the upper limb [139]. The dynamic characteristics of the model as well as the activation dynamics of muscle units are used in conjunction with joint kinematics and EMG signals to obtain a continuous estimation of the arm stiffness [190].

The aim of this work is to evaluate how different master devices and tasks influence the regulation of arm endpoint stiffness and its relation with task performance, hand speed and acceleration. We developed two planar tasks consisting in the position and orientation control of a virtual tool. The two task variations were intended to trigger the use of different biomechanical DoFs to demonstrate the influence of such constraints on the estimation of end-effector stiffness. We compared a parallel link (PL) and a serial link (SL) master device, to test how the differences between the two manipulators would elicit different levels of arm end-point stiffness during virtual teleoperation. During task performance, arm kinematics and EMG signals were acquired using an optical and a magnetic tracking systems).

Our primary hypothesis is that end-effector stiffness would be modulated according to both the mechanical features of the master device and the task characteristics. In particular, we expect the users to generate higher overall end-point stiffness when teleoperating with the serial link master device, characterized by lower structural stiffness and apparent mass. We also expect the users to increase arm stiffness while performing the second task; due to the increased complexity of simultaneously controlling position and orientation of the virtual tool. Our second hypothesis is that end-point stiffness would be modulated accordingly to curvature variations throughout the trajectory. More specifically, we believe that high curvature can be associated with higher complexity in executing the task, leading to higher values of arm end point stiffness. As third and final hypothesis, we expect a correlation between the hand speed and acceleration and arm end-point stiffness so that the users would generate the maximal levels of stiffness during slow and non accelerated movements.

4.2 Materials and methods

In order to analyze the stiffness regulation during virtual tele-operated tasks, we created a simple teleoperation scenario in which the users interacted with master devices to control virtual tools used to perform specific tasks.

4.2.1 Tasks design

Simple repeatable and cyclical planar virtual tasks were developed to challenge the users with different levels of complexity without requiring any surgical expertise.

1. *Half Cloverleaf (HC)*
   Figure 4.1.1 shows the first virtual trajectory which represents half the cloverleaf motion as presented by [134]. A virtual stylus shaped tool was manipulated in the simulated environment to follow the trajectory, starting from the initial position (green dot in Fig.4.1.1) and moving first counter-clockwise,

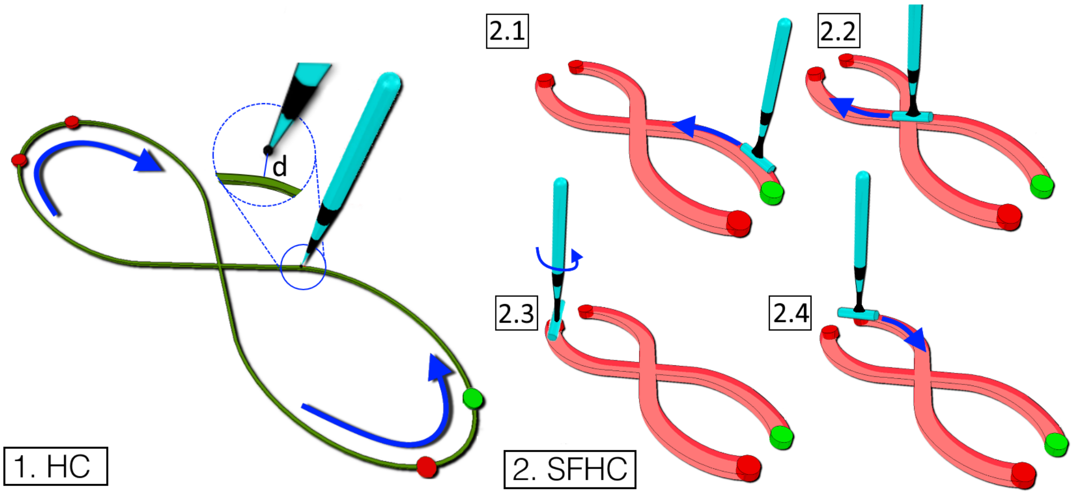

FIGURE 4.1: The figure represents the two trajectories designed. Task 1. A line following task shaped as an half cloverleaf (HC). The aim to to finely follow the trajectory starting from the green dot and moving anti-clockwise. Task 2. In the task, shaped as a thicker half cloverleaf (SFHC), the users have to orient the tool's cylindrical end-effector along the trajectory (2.1 to 2.4)

then straight crossing the intersection in the middle, finally in a clock-wise direction to return to the starting position. In order to make the subject perform the task approximately in the x-y plane of a three-dimensional Cartesian reference frame, a visual cue was provided in the form of the path color which turned green when the tool-tip of the stylus was in the said plane ($-1mm < z < 1mm$), red otherwise.

2. *Shape Fitted Half Cloverleaf (SFHC)*
   The second task was designed to include wrist rotation as the subjects were asked to navigate a virtual cylindrical shaped tool tip along the path, as shown in Fig. 4.1.2. The trajectory that the users were requested to follow was identical to the one of the previous task, with the added complexity of following the trajectory silhouette using the tool end-effector. Starting from the green dot (4.1.2), the users were asked to slide the tool end-effector over the shape fitted trajectory (see Fig. 4.1.2.1) . In order to follow the first portion of the trajectory, the users needed to flex the wrist until the central intersection was reached (see Fig. 4.1.2.2) and then to extend it to reach the top left. At the trajectory upper end (red dot in Fig. 4.1.2.2), the users had to flex the wrist and abduct the shoulder to reposition the tool end-effector on the shape fitted trajectory (see Fig. 4.1.2.3). Similarly, the users had to reach the lower open end (see Fig. 4.1.2.4) to complete the task. As in the previous task, the visual feedback consisted in the change of the path color to green when the tool tip lied in the desired plane.

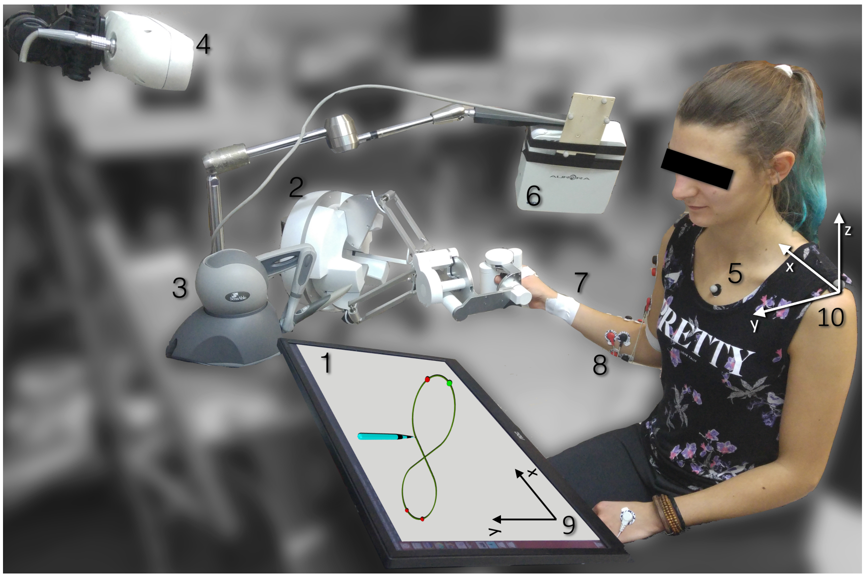

FIGURE 4.2: Experimental setup: the user performs the task looking at a monitor laid flat on a table (1) while teleoperating using either a parallel link haptic device PL (2) or a serial link haptic device SL (3) while the thorax and arm kinematic are acquired with an optical camera (4) and reflective markers (5) and with electromagnetic tracker (6) and markers (7). The EMG activation is also acquired with bipolar electrodes (8).The virtual reference frame (9) and the shoulder reference frame (10) are grossly aligned in the setup phase.

4.2.2 Experimental setup

Master devices

The subjects were controlling the virtual tool's position and orientation using two different master devices: a 7 DoFs parallel links haptic interface (PL) and a 6 DoFs serial links haptic interface (SL). A Force Dimension Sigma7 (Force Dimension, Nyon, Switzerland) was used as PL (see Fig. 4.2.2). The master device, gravity compensated, is characterized by 6 DoFs plus a grip control, has a resolution of 0.0015 mm and 0.013 deg and an elliptical dome workspace with radiuses of approximately 190x130 mm . Thanks to its design, the translational and rotational degrees of freedom are completely decoupled, and the grasping unit has an apparent mass of 259 g ([191]). The parallel-link structure also contributes to produce a system stiffness of approximately 14 N/mm.

A Phantom Omni (3D Systems, South Carolina, USA) was used as SL (see Fig. 4.2.3). The device is characterized by a 0.055 mm resolution, a 160x120x70 mm workspace and it's controlled through a stylus end-effector. Even though the device is not gravity compensated, which means that the tele-operator had to sustain the stylus and part of the links weight when manipulating it, it is characterized by an apparent mass at the tip of 45 g. Due to its design, the system stiffness components are not constant in the three axes, ranging from 1.02 N/mm to 2.31 N/mm.

Such differences in the master devices dynamic proprieties, both in terms of apparent mass of the end-effector and system stiffness, contribute to create a higher sense of stability while teleoperating with PL.

For both the SL and PL master devices custom impedance controllers were developed using the proprietary API. In both master devices, the users hand movements were downscaled with a factor of 2. The described tasks were designed to fit within the workspaces of both devices in order to avoid the necessity of using the devices clutching option. If used, the clutching would allow to decouple the virtual tool position from the master device end-effector position, allowing to reconfigure the arm when hitting the workspace limits. This option was excluded from the experiments since it would have caused significant kinematic variability during task execution.

Acquisition framework

The user's thorax and arm position and configuration were acquired using two localization devices calibrated to the same reference frame with a hand eye calibration approach [135]. The thorax position was acquired using an optical localization system (see Fig. 4.2.4)(Vicra, Northern Digital, Ontario, Canada, 20Hz sampling rate, 0.25mm position Root Mean Squared Error (RMSE)) using three passive retroreflective markers attached to the right and left acromions and next to the jugular notch.

The arm configuration was measured using an electromagnetic localization system (see Fig. 4.2.6) (Aurora, Northern Digital, Ontario, Canada, 30Hz sampling rate, 0.48 mm and 0.3deg position and orientation RMSE, dome shaped field with a radius of approximately 500mm) and three 6-DoF 1.8x9 mm electromagnetic sensors (see Fig. 4.2.7) that were used to generate 6 corresponding virtual markers calibrated on the users' recognizable bony landmark on elbow, wrist and hand.

EMG signals were recorded through a TMSi Porti device (Twente Medical Systems International, Oldenzaal, Nederland, 32 channel acquisition system, 2048Hz sampling rate) using 10 bi-polar electrodes (see Fig. 4.2.8). Three couples of electrodes were used to acquire the electromyographic signals from the anterior, lateral and posterior deltoid fiber bands (Fig. 4.3.1-2-3). Two couples of electrodes were used to acquire the long and lateral triceps brachii heads (Fig. 4.3.4-5) and a single couple was used to acquire the biceps muscle (Fig. 4.3.6). Four electrode couples were used on the forearm to measure the activation of the brachioradialis, flexor carpi ulnaris and radialis and extensor digitorum (Fig. 4.3.7-8-9-10). The monopolar electrode used as reference was attached to the users' left hand. The muscular maximal voluntary contraction (MVC) was recorded right before the experiments: each subject was asked to perform a set of different isometric contractions against static resistance with different joint configurations [192]. The different movements were designed to elicit the activation of the muscles responsible for the same kinematic function: for instance, the biceps' MVC was recorded by asking the users to push the hand palm against a tabletop bottom while flexing the elbow; similarly, the forearm flexors' MVC were acquired during isometric wrist flexions against static objects. The contractions lasted for about 5 seconds and were followed by a second trial after 30 seconds, to avoid muscular fatigue. The mean of the two maximal

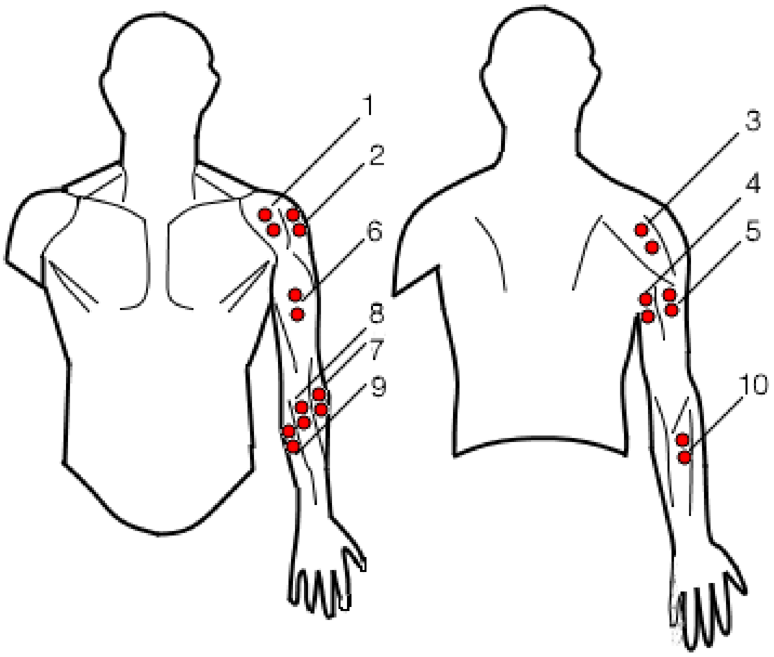

FIGURE 4.3: Surface electromyography electrodes placement: 1-2-3 for the anterior, lateral and posterior deltoids, 4-5 for the long and lateral trisceps brachii, 6 for the biceps, 7-8-9 for the brachioradialis, flexor carpi radialis and ulnaris respectively and 10 for extensor digitorum

absolute values registered during the two repeated movements was extracted from the conditioned signals for each muscle. The MVC signals were processed with the same procedure as the EMG signals recorded during the experiments. The acquired and processed MVC signals were used within the musculoskeletal model to scale the recorded EMG signals with respect to the maximal contraction: in this way, the EMG recordings values were unified and expressed as fraction of the maximal muscle capabilities.

Retroreflective and electromagnetic markers movements and EMG signals were acquired, recorded and synchronized using custom developed software based on the Robotic Operating System (ROS, http://www.ros.org/).

Experimental Protocol

We recruited 4 healthy subjects (2 female and 2 male, mean age 23±1.5) who provided informed written consent, in accordance with the recommendations of Politecnico di Milano Ethical committee Board and the Declaration of Helsinki.

The subjects were sitting in a comfortable chair without arm rests, in front of a 2D monitor screen where the virtual tasks were displayed (Fig. 4.2.1) . The chair position was adjusted in order to allow an easy interfacing between the subjects and the tasks. The monitor was laid as flat as possible on the table to be approximately

TABLE 4.1: Experiments list and description

Experiment acronym	Master device	Task	Number of trials
PL1	PL	HC	10
PL2	PL	SFHC	10
SL1	SL	HC	10
SL2	SL	SFHC	10

parallel to the plane in which the tasks were performed, allowing for the most intuitive control, in which the users hand movement directly corresponded to the virtual tool movement.

Each user was asked to perform ten trials of every task while trying to maintain the hand movement on a constant plane, exploiting visual color feedback as explained in Sec. 4.2.1. Subjects were instructed to perform HC and SFHC tasks finding a personal trade-off between precision and execution speed. Table 4.1 describes the four experiments performed: for each subject the experiment order was randomized so that users performed the 10 repetitions of a randomly selected condition before moving on the next randomly selected one.

4.2.3 Stiffness computation

The kinematic and dynamic characteristics of the user arm movements, as well as their muscular activations were obtained and elaborated to compute the arm endpoint stiffness during task execution.

Kinematic Analysis

The arm and thorax spatial configuration were reconstructed using the experimental markers data and the musculoskeletal model implemented in OpenSim [139]. The model, whose capabilities in predicting the arm dynamics were previously assessed [137], is derived from Holzbaur's model [138] and composed by seven DoFs activated by 32 muscle compartments. The model was scaled to fit the anthropometric characteristics of each subject and its virtual markers were displaced to the average real markers position acquired during a static pose.

The markers position data were filtered by applying an IIR second order Butterworth filter twice, reversing the time in the second filtering in order to cancel the non linear phase shift. Filter cutoff frequency was set to 4Hz (- 6dB) and the filtered data were used as input for the inverse kinematics. The inverse kinematic algorithm solves the minimization problem in (4.1) for each set of marker coordinates.

$$\min_{\mathbf{q}}[\sum_{k \in N = \textit{number of markers}} w_k \|\mathbf{x}_k^{exp} - x_k(\mathbf{q})\|^2] \tag{4.1}$$

Where $\mathbf{q}$ is the vector of joint angles, $\mathbf{x}_k^{exp}$ is the experimental 3D position of the k^{th} marker, acquired using the optical or the magnetic tracking device, $\mathbf{x}_k(\mathbf{q})$ is the position of the corresponding virtual marker on the model that depends on the vector of joint angles $\mathbf{q}$, and w_k is the k^{th} marker weight thorough which is possible to account for the uncertainty related to each marker position detection. For each set of marker coordinates, the algorithm finds the best joint vector $\mathbf{q}$ that minimizes the error between the experimental marker position vector $\mathbf{x}^{exp}$ and the virtual markers position vector $x(\mathbf{q})$, which is a function of the fixed model geometry and joint vector, $\boldsymbol{q}$.

In order to define the correct weighting vector $\mathbf{w} = [w_1, .., w_k, .., w_N]$ with N = number of markers, we analyzed the markers positions during a static recording. The ratio between the standard deviations from optical markers and electromagnetic markers is comparable with the ratio between the RMSE characteristics of each device. We therefore weighted the thorax optical markers with a coefficient of 1, while the arm, forearm and hand electromagnetic markers with a coefficient of 0.52 (obtained from the ratio between the nominal RMSE for the optical tracker, 0.25mm and the electromagnetic tracking device RMSE, 0.48mm).

Dynamic Analysis

The obtained joint angles were filtered with an IIR second order Butterworth filter (cutoff frequency 4Hz) twice, compensating the nonlinear phase shift. The filtered data were used as input for the inverse dynamic reconstruction, along with the model dynamic characteristics (masses and inertial proprieties of each model segment). Equation 4.2 shows the dynamic equation when no external forces are applied to the arm; $\boldsymbol{\tau}$ is the unknown (7x1) vector of joint torques, $\mathbf{M}$ is the system mass matrix, $\mathbf{C}$ is the vector of Coriolis and centrifugal forces, $\mathbf{G}$ is the vector of gravitational forces, while $\boldsymbol{q}$, $\dot{\boldsymbol{q}}$, $\ddot{\boldsymbol{q}}$ are the vectors of joint position, velocities and accelerations respectively.

$$\boldsymbol{\tau} = \boldsymbol{M}(\mathbf{q})\ddot{\mathbf{q}} - \boldsymbol{C}(\mathbf{q}, \dot{\mathbf{q}}) - \boldsymbol{G}(\mathbf{q}) \tag{4.2}$$

EMG-informed torque estimation

A refined estimation of the joint torques was obtained using the Calibrated EMG-informed Neuro-Musculoskeletal (CEINMS) modelling toolbox in which the musculotendon unit (MTU) force arms obtained with the inverse kinematics are used with the joint torques estimated by the inverse dynamics and the recorded EMG signals.

The tool firstly calibrates the experimental muscle excitations derived from the surface EMG acquisition with the muscle activation patters, obtained from the inverse dynamic algorithm [193, 194]. The resultant calibrated model is then used to predict MTU forces, joint moments, and muscle activations solving a set of differential equations that relates the muscle excitation with the electrical activity recorded [195]. To be used as an input to the EMG-informed inverse dynamic algorithm, the EMG data was previously high pass filtered at 30Hz, full wave rectified and filtered with a zero-lag second order Butterworth filter (6Hz cutoff frequency) [193]. The experimental muscle excitations were normalized using each user's maximal voluntary contractions (MVC).

Stiffness computation

For each fiber within the musculoskeletal model, the $(\mathbf{32} \times \mathbf{32})$ diagonal muscular stiffness $\mathbf{K}_m$ was estimated from the variation of muscular forces $\mathbf{F}m$ and corresponding fiber lengths $\mathbf{l}$ at the i^{th} time frame [196]:

$$\mathbf{K}_m(i) = \frac{d\mathbf{F}_m(i)}{d\mathbf{l}(i)} \tag{4.3}$$

To map the muscular force matrix $\mathbf{K}_m$ in the joint space, obtaining the $(\mathbf{7} \times \mathbf{7})$ joint stiffness matrix $\mathbf{K}_\mathrm{j}$, the muscle Jacobian matrix $\mathbf{J}_m$ is used:

$$\mathbf{K}_\mathrm{j}(i) = \mathbf{J}_m^T(i)\mathbf{K}_m(i)\mathbf{J}_m(i) + \frac{\partial \mathbf{J}_m^T(i)}{\partial q(i)}\mathbf{F}_m(i) \tag{4.4}$$

where the $(\mathbf{32} \times \mathbf{7})$ muscle Jacobian matrix $\mathbf{J}_m$ represents the matrix of the muscle force arms and relates small changes in the muscle's fiber lengths ∂l to small changes in joint angles ∂q.

$$\mathbf{J}_m(i) = \begin{pmatrix} \frac{\partial l_1(i)}{\partial q_1(i)} & \frac{\partial l_1(i)}{\partial q_2(i)} & \cdot & \frac{\partial l_1(i)}{\partial q_7(i)} \\ \frac{\partial l_2(i)}{\partial q_1(i)} & \frac{\partial l_2(i)}{\partial q_2(i)} & \cdot & \frac{\partial l_2(i)}{\partial q_7(i)} \\ \cdot & \cdot & \cdot & \cdot \\ \frac{\partial l_{32}(i)}{\partial q_1(i)} & \frac{\partial l_{32}(i)}{\partial q_2(i)} & \cdot & \frac{\partial l_{32}(i)}{\partial q_7(i)} \end{pmatrix} \tag{4.5}$$

In order to obtain the Cartesian representation of the arm stiffness, the arm endpoint Cartesian stiffness $(\mathbf{K}_\mathbf{e})$ has been obtained using the arm kinematic Jacobian $\mathbf{J}$ $(\mathbf{7} \times \mathbf{6})$, as follows:

$$\mathbf{K}_\mathbf{e}(i) = (\mathbf{J}^{-1})^T(i)\mathbf{K}_\mathrm{j}(i)\mathbf{J}^{-1}(i) \tag{4.6}$$

Through the Singular Value Decomposition (SVD), the left singular vectors and non-zero singular values of $\mathbf{K}_\mathbf{e}$ were obtained to draw the end-point stiffness ellipsoid orientation and dimensions that are used as a way of visually represent the stiffness [174]. The maximal singular value of $\mathbf{K_e}$ is the maximal stiffness value ($K_{max}(i)$) in the i^{th} time instant.

4.2.4 Metrics and statistical analysis

The following performance-related parameters were evaluated:

- 2D distance from the trajectory at the i^{th} time frame, d_i: the distance is computed from the tool tip to the closest point on the trajectory center on the task plane (see Fig. 4.1); it is calculated as shown in (4.7).

$$d(i) = \sqrt[2]{(x_{target}(i) - x_{tool}(i))^2 + (y_{target}(i) - y_{tool}(i))^2} \tag{4.7}$$

  Where $(x, y)_{target}$ are the tool tip's 2D coordinates and $(x, y)_{tool}$ are the 2D coordinates of the closest point on the trajectory. The z-component of the displacement from the trajectory was excluded from the distance metric computation due to the significant differences that the color visual feedback could introduce with respect to the other two dimensions.

- Maximal stiffness K_{max}: the end-point stiffness ellipsoid main axis was computed in 29 (for HC) and 23 (for SFHC) equally spaced points along the task trajectory (for SFHC, the points corresponding to the open ends were excluded from the analysis). For each task trial and for each point selected, the three closest virtual tool positions were searched and the corresponding maximal stiffness ($K_{max}(j)$, $K_{max}(j+1)$ and $K_{max}(j-1)$) were averaged to obtain the mean maximal stiffness estimation as in (4.8)

$$\overline{K}_{max} = \frac{1}{3}(K_{max}(j-1) + K_{max}(j) + K_{max}(j+1)) \tag{4.8}$$

  With $j = 1...M - 1$ number of points along the trajectory.

- Curvature *C*: In both tasks, the trajectory was created to fit the same Bernulli's Lemniscate function. The generic function of a Bernulli Lemniscate curve in a planar x-y plane with the main axis oriented along the x axis is

$$(x^2 + y^2)^2 = 2a^2(x^2 - y^2) \tag{4.9}$$

  Where *a* is the parameter that defines the position of the curve foci. The task trajectory curvature (*C*) can be computed in polar coordinates using:

$$C(t) = \frac{3\sqrt{2}cos(t)}{\sqrt{3 - cos(2t)}} \tag{4.10}$$

  with *t* that spans from 0 to 2π. For each 3D point of the trajectory selected for the stiffness analysis, the corresponding curvature was computed.

- Hand speed and acceleration: the position and orientation of the hand in the shoulder reference frame (see Fig. 4.2.10) was computed. The speed was obtained performing numerical differentiation on the x-y-z coordinates, smoothing the signal with a second order Butterworth filter with cutoff frequency of 4Hz twice forward and backward. Acceleration was computed and filtered from hand speed following the same procedure previously described.

For all the metrics, the statistical distribution normality was tested for each user in the four experiments PL1, PL2, SL1, SL2 (see Table 4.1) using a one-sample Kolmogorov-Smirnov test with 1% significance level. The arm stiffness data resulted to be non-normal, therefore, using the natural logarithm function (as in [197]), the data was normalized: the same Kolmogorov-Smirnov test was performed for each user, repetition and experiment, identifying as normal the 97% of the distributions. The distance metric, as well as the hand speed and acceleration had a normal distribution (Kolmogorov-Smirnov $\alpha = 0.01$).

Analysis performed and hypothesis tested

All the inferential statistic analysis that will be presented were conducted with the Statistics and Machine Learning Toolbox for Matlab 2016b (Mathworks, Natick, Massachusetts, US).

1. Maximal stiffness through the trajectory - The stiffness maximal values $\boldsymbol{K_{max}}$ were first of all studied as a function of the task type and controller. The distributions of the normalized stiffness data were compared between users and repetition, since no significant differences were found, the users data were grouped together for each experiment

   Hypothesis 1 & 2: To analyze whether the task and master device types, as well as level of trajectory curvature affected the maximal values of stiffness, the data from the 29 (HC) and 23 (SFHC) points on the trajectory for each experiment were grouped. The mean values of maximal stiffness for each region of curvature and repetition were extracted and a three-way ANOVA was performed on the log-normalized data (task, master device type and curvature region as fixed factors, user number as random-effect factor). To further test the effects of the different factors on the end-point stiffness, the same ANOVA model was also applied to the stiffness variability in the various regions and repetitions. To test the presence of possible correlations between stiffness and curvature the Pearson rank test ($\alpha = 0.05$) was adopted.

2. Stiffness against hand speed and acceleration - Using two separate two-ways ANOVAs (task and master device type as fixed factors, user number as random-effect factor) the hand speed and acceleration distributions in the four experiments were analyzed. Hypothesis 3: we tested the hypothesis that a relation between hand speed and acceleration with respect to maximal stiffness could

exist. For each of the ten trajectory repetitions, 4 levels of hand speed and acceleration were obtained in the four experiments and for the 4 users. Two separated three-way ANOVAs were performed on the corresponding values of stiffness (task, master device type and level of speed/acceleration as fixed factors and user number as random effect factor).

3. Distance metric - The difference between different trials of the same experiment for each user was tested using a one-way ANOVA test ($\alpha = 0.05$). Since no statistical difference emerged, the mean values of distance throughout each repetition and user were extracted. The four experiments' performance distributions were then modeled with a two-way ANOVA statistical model, where task and master device type were considered as fixed factors, while user number was considered as random effect factor.

4.3 Results

4.3.1 Maximal Stiffness through the trajectory

Figure 4.4 shows the results obtained when the mean stiffness values through the trajectory among users and trials for each experiment are grouped together. The stiffness values below a threshold of 0.1 N/m were removed from the analysis: the threshold was obtained from previous arm end-point stiffness estimations [172, 90] and the percentage of values discarded was less than 1% of the total dataset. The results of the three-way ANOVA analysis showed no significant interaction between the factors, and a statistical difference between tasks (HC and SFHC) (F(1,624) = 10.06, $p < 0.005$) while no significant difference was found between the master devices (F(1,624) = 0.14, $p = 0.70$). Overall, users elicited significantly higher arm stiffness when performing the HC task with respect to SFHC.

Figure 4.5 shows the end-point stiffness variability in the four experiments. The three-way ANOVA test showed no significant interactions among factors and statistical difference between both tasks (F(1,624) = 7.75, $p < 0.01$) and master devices (F(1,624) = 7.64, $p < 0.01$). Interestingly while the stiffness variance increases in the SFHC task when teleoperating with PL, when teleoperating with the SL master device, instead, users decreased the arm stiffness variance when performing SFHC with respect to HC. Overall, users explored the highest range of end-point stiffness in HC when teleoperating with SL and showed the lowest variance with the same master device in the SFHC task.

To further analyze stiffness modulation through the 29 (for HC) and 23 (for SFHC) points along the trajectory while teleoperating with the PL and SL master devices, Fig. 4.6 shows the median values obtained for each experiment. The results are presented as a tri-dimensional graph where each point mean K_{max} value is represented as a colored column (see Fig. 4.6). No evident trends can be found in stiffness maximal values modulation through the trajectory points.

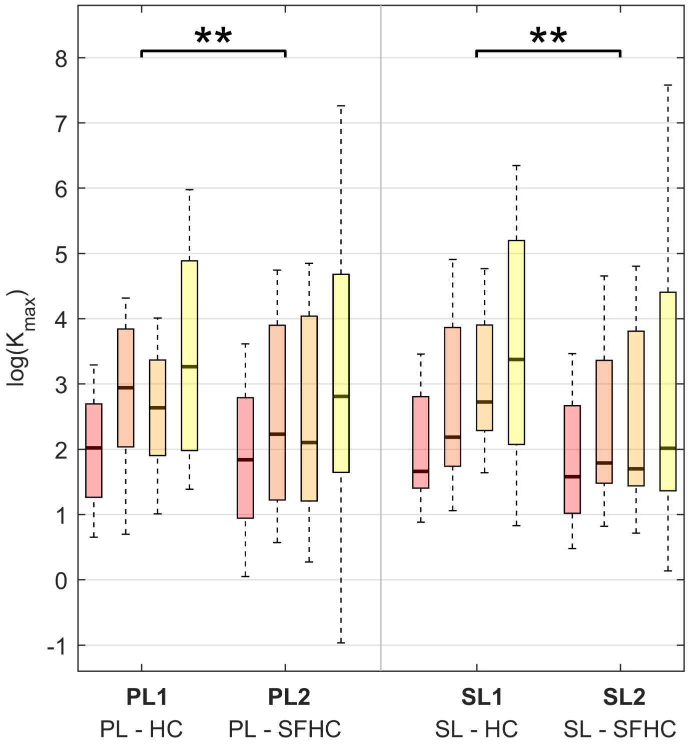

FIGURE 4.4: Maximal stiffness ($\boldsymbol{K_{max}}$) distribution in the four experiments for the four increasing levels of curvature. The results are presented using boxplot indicating median, first and third quartile, minimal and maximal values. Horizontal lines over the boxes indicate statistical difference while the number of stars indicate different levels of significance (** = $p<0.01$)

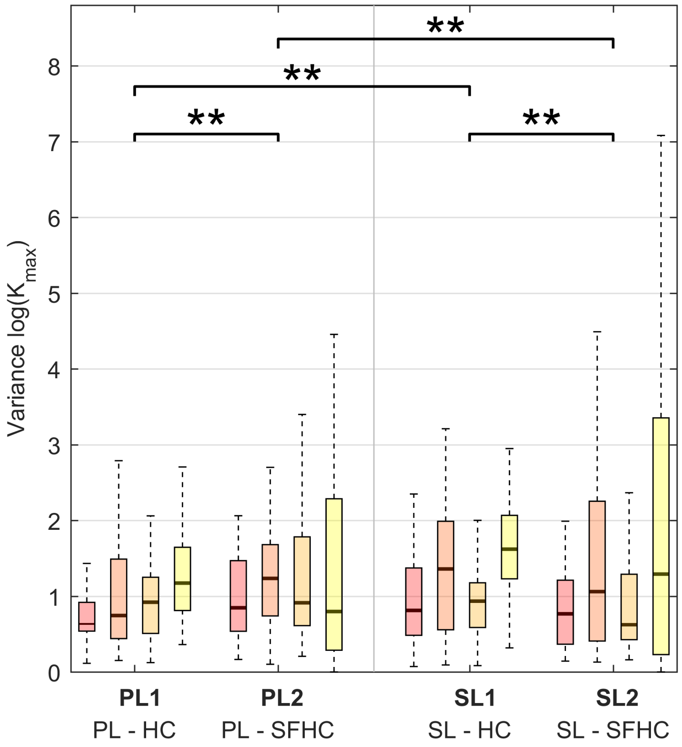

FIGURE 4.5: Variance of maximal stiffness (K_{max}) in the four experiments for the four increasing levels of curvature. Horizontal lines over the boxes indicate statistical difference while the number of stars indicate different levels of significance (** = p<0.01)

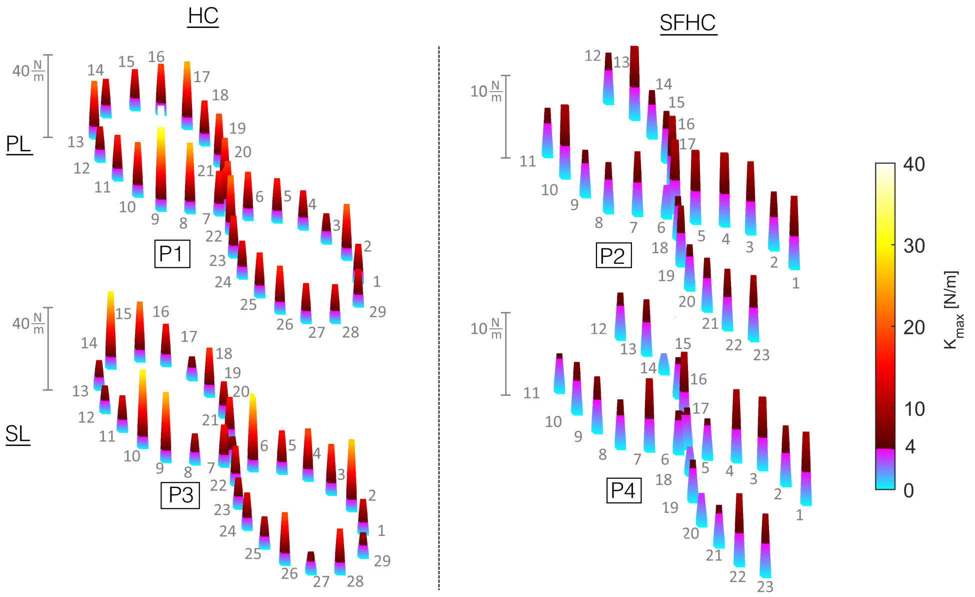

FIGURE 4.6: Maximal stiffness K_{max} from all the users and trials in each point along the trajectory is presented: the height and color of each column indicates the corresponding point median. To account for the difference in terms of median values from experiments PL1 and SL1 compared with PL2 and SL2, a custom colormap was designed. K_{max} values from 0 to 4 N/m are plotted with colors from light blue to purple, while K_{max} values from 4 to 40 N/m range from a dark red to bright yellow.

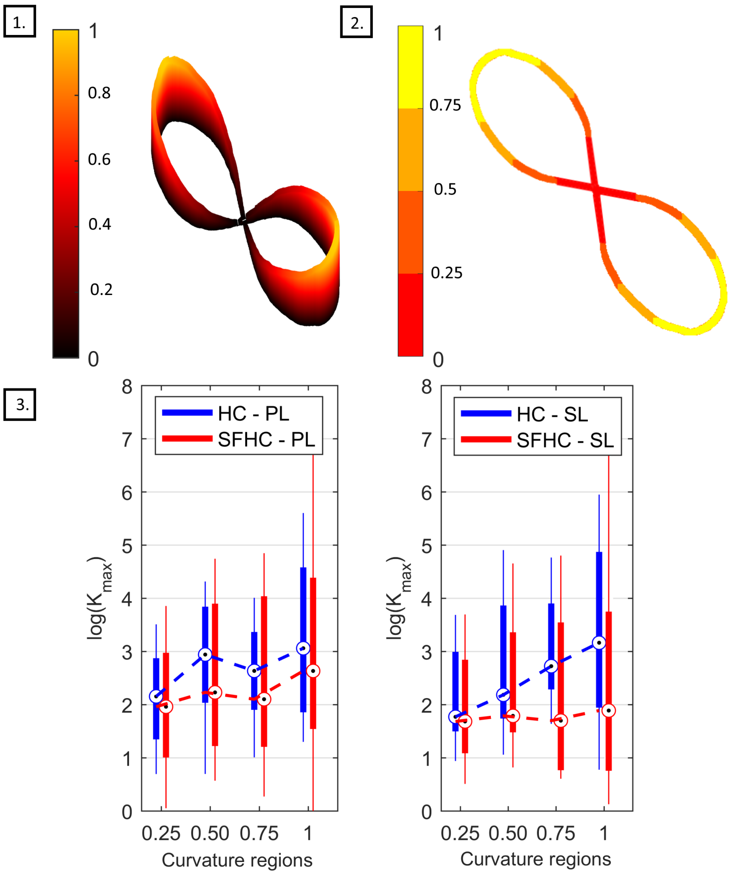

FIGURE 4.7: Stiffness with respect to curvature analysis. 1. Normalized curvature through the trajectory. 2. Definition of the four regions of normalized curvature. 3. Box-plot comparing the maximal stiffness value K_{max} for the PL master device, on the left, and for the SL master device on the right. The boxes represent the first and third quartile, while the whiskers represent the minimal and maximal values.

Regarding the end-point stiffness mean values relation with curvature, the three-way ANOVA showed significant difference (F(3,624) = 28.19, p<0.0001) between the four different levels of curvature. The box-plots in Fig. 4.7.3 show the maximal stiffness distribution as function of four levels of trajectory curvature for PL and for SL. Although characterized by high interquartile distances, the similar behavior can be observed for PL and SL and in the two tasks: the smallest K_{max} mean values are registered where the normalized curvature is $< \mathbf{0.25}$ while the maximal values appear in the range between 0.75 and 1. Interestingly, while for the hybrid parallel-serial link master device (PL) the end-point stiffness behavior in HC and SFCH shows the same trend, with an apparent plateau in the middle curvature zones, different behaviors can be seen with SL. In this case, HC shows a clear increase in the mean value of maximal stiffness with increasing levels of curvature, while in SFHC users were eliciting very small variations of arm end-point stiffness. Due to the high variance in the data, Pearson correlation analysis showed non-significant ($p > \mathbf{0.05}$) correlations for all the experiments. Furthermore, regarding the stiffness variability in the four regions of curvature, the three-way ANOVA test showed no significant

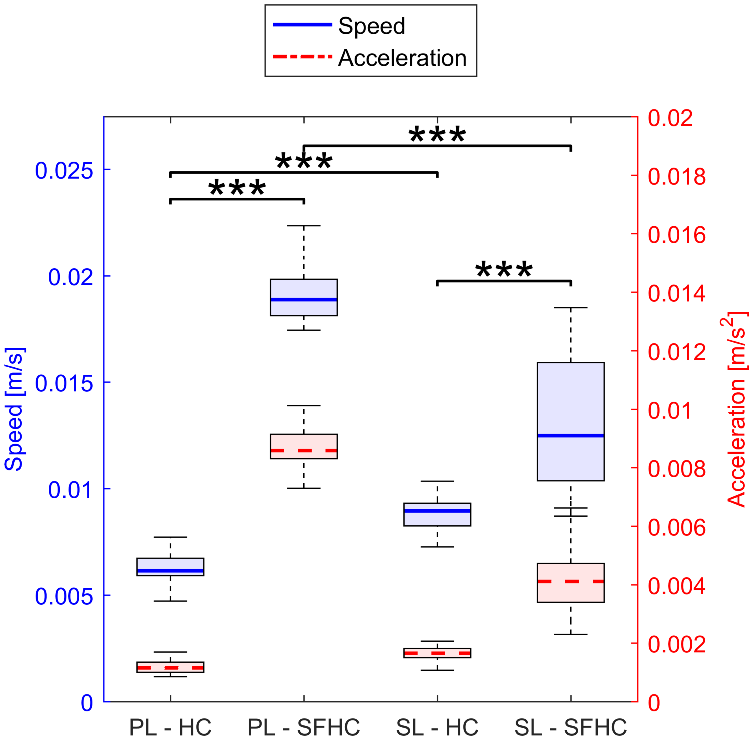

FIGURE 4.8: Distribution of speed (in blue, solid line) and acceleration (in red, dashed line) in the four experiments. Horizontal lines over the boxes indicate statistical difference while the number of stars indicate different levels of significance (*** = p<0.0001)

differences (F(3,624) = 1.54, p = 0.20).

4.3.2 Stiffness against hand speed and acceleration

Figure 4.8 shows the speed and acceleration distribution in the four experiments; the two separated two-ways ANOVAs showed significant differences in tasks and master devices in both speed (F(1,156) = 998 $p < 0.0001$ and F(1,156) = 36 $p < 0.0001$ respectively) and acceleration (F(1,156) = 1300 $p < 0.0001$, F(1,624) = 180 $p < 0.0001$ respectively). The two separate three-way ANOVAs showed no significant interaction among task, master device type and level of speed or acceleration; a main significant effect was found for the task type (F(1,624) = 10.23, $p < 0.005$ when the data was grouped in levels of speed and F(1,624) = 10.23, $p < 0.005$ for levels of acceleration) while no significant effects were found for the master device type and the levels of speed or acceleration. Figure 4.9 shows the end-point stiffness distribution with respect to increasing levels of speed and acceleration for the four experiments. To emphasize the differences in the stiffness distribution, the non-normalized stiffness values are presented. The Pearson correlation tests between the log-normalized data and the hand speed and acceleration in the four experiments showed low ($|p|$ ranging from 0.1 to 0.3) non significant ($\rho > 0.1$) negative correlations.

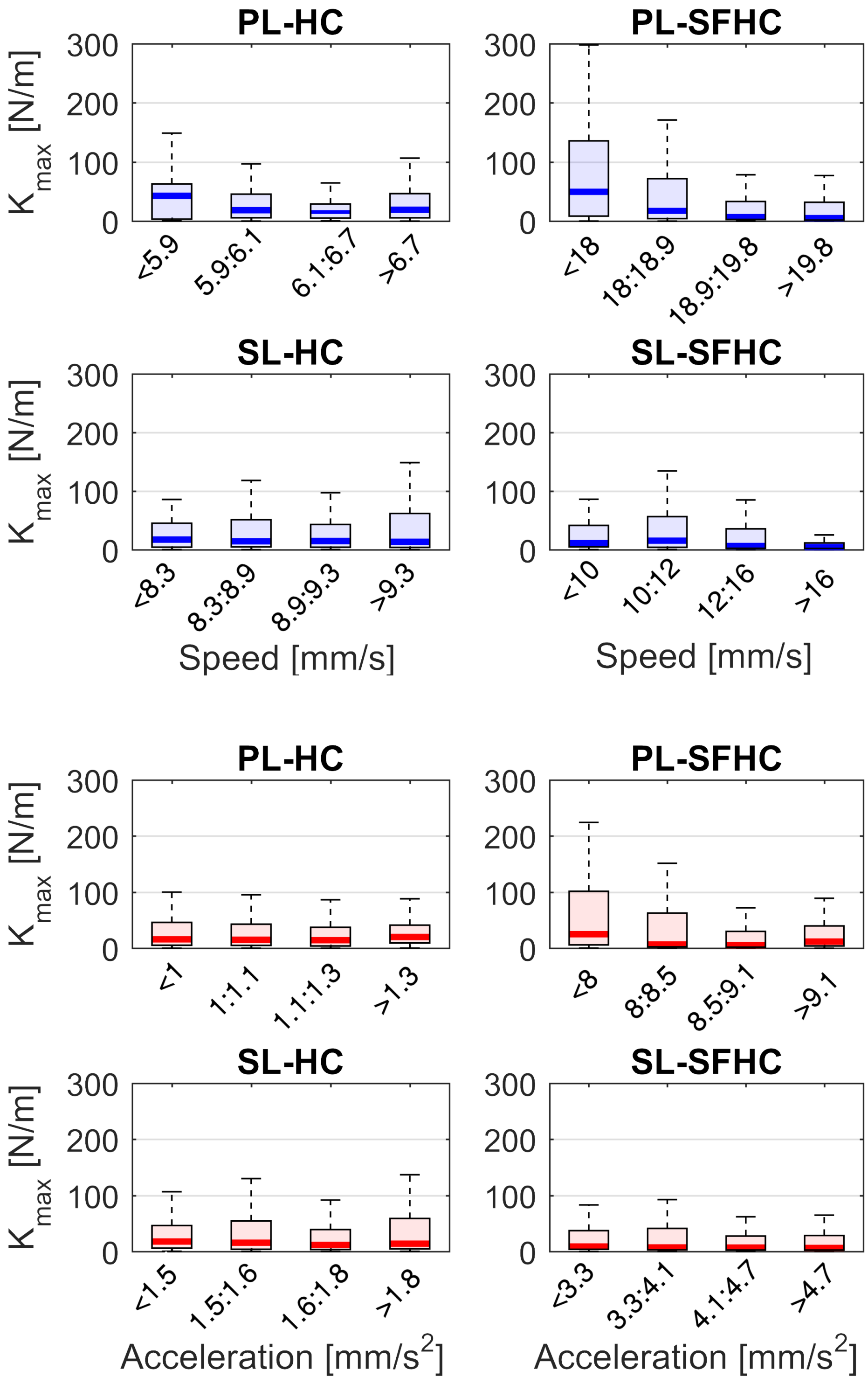

FIGURE 4.9: End-point stiffness distribution with respect to four increasing levels of hand speed (in blue) and acceleration (red). The levels of speed and acceleration correspond to each experiment distribution quartiles.

4.3.3 Distance metric

The mean distance value for each repetition was obtained for each of the 10 repetitions and users and the obtained data sets were grouped in the four experiments. The results of the two-way ANOVA with subjects' number as random-effect parameter showed a difference between HC and SFHC (F(1,156) = 548 $\boldsymbol{p < 0.0001}$) and no difference between PL and SL (F(1,156) = 2.43 $\boldsymbol{p = 0.1214}$). The users were capable of achieving the best performances, testified by lower distances, with the parallel link master device (PL) and in the first task (HC). Similarly as seen with the maximal stiffness values (see Fig. 4.4), the interquartile distances for SFHC are significantly higher than in HC.

4.4 Discussion

We evaluated the arm end-point stiffness modulation adopted by novice teleoperators in performing two tasks with two different master devices as a reflection of the control strategies adopted by the central nervous system to increase the hand resistance to internal and external noise. Using kinematic and muscular parameters, we estimated the stiffness and its relation with the trajectory characteristics and the hand speed and acceleration.

The difference in maximal stiffness values between the different task types (as presented in Fig. 4.4) proves that the users were adapting their stiffness modulation strategies to the different task characteristics. We were expecting higher values of end-point stiffness during the execution of the SFHC task, due to the increased complexity added by the requests to orient the tool; instead, the stiffness is significantly higher in the HC tasks. A possible explanation to this result may be that the users were discouraged to increase the arm stiffness in order to comfortably activate the wrist joint. In fact, to increase the overall arm stiffness, it would be necessary to increase the level of co-contraction also for the wrist flexor-extensors, potentially impairing the free rotation of the wrist. Therefore, this significant difference in stiffness values between HC and SFHC may be explained by the different levels of wrist flexion-extension activations that were registered in the two tasks. As an example, Fig. 4.10 shows the wrist flexion-extension patterns found during the execution of HC and SFHC for a single user with the PL master device. The same significant difference can be seen in all the acquired users. The fact that users were eliciting similar values of stiffness when teleoperating with the two master devices seems to suggest that users can compensate for the significant differences in the master devices mechanical proprieties assuring the same overall dynamic performances.

Users showed the highest end-point stiffness variability when teleoperating with the serial link robot during the execution of the HC task, possibly hinting that for that specific task, the SL master device's characteristics offered a less stable and reliable interaction with respect to PL. Interestingly, while for the PL master device the request to orient the tool along the trajectory introduced higher variability in the

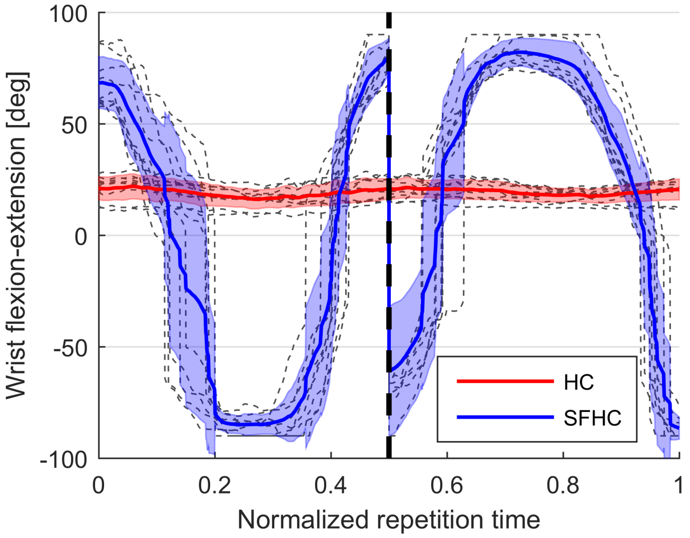

FIGURE 4.10: Wrist flexion-extension patterns during the execution of HC and SFHC for a single user: in gray the single normalized task repetitions, red and blue lines represent the mean joint angle signal for HC and SFHC, while red and blue areas represent the standard deviation interval.

elicited stiffness, the opposite can be seen for SL. This discrepancy could be caused by the significant differences in the master device structural construction: in PL the hand rotations are completely decoupled from translations while in SL rotations are less hand-centered. This finding would therefore endorse the hypothesis that different kind of tasks may require different master device mechanical characteristics.

The statistical difference in arm stiffness mean values between different regions of curvature could suggest a relation between trajectory curvature and stiffness maximal values: in fact, the users were generally generating the lowest stiffness in the low-curvature portion of the trajectory. Under the hypothesis that straight trajectories are easier to follow than highly curved ones, it is possible that the users were relying on higher stiffness to increase their performance in the most difficult parts of the trajectory. On the other hand, this modulation seems particularly affected by the task and master device characteristics. By looking at the stiffness distributions in Fig. 4.7, it seems that while the PL master device offers a rather consistent interface for both tasks, allowing more or less the same modulation in HC and SFHC, the SL master device showed different behaviors in the two tasks. Specifically, while an increase in the mean stiffness at high curvature can be seen for the HC task, arm end-point stiffness was almost constant for SFHC. This discrepancy may suggest that, during the SFHC task performance, when teleoperating with the SL master device, users weren't able or didn't felt the necessity to adopt the same kinetic strategy that they used otherwise.

The disparity in the speed and acceleration distributions between the two tasks could lie in the differences in the task graphical representation: in order to make the SFHC task more clear, the trajectory thickness is increased with respect to the HC.

In the same way, the tool-tip changes from a small point (in HC) to a cylinder (in SFHC). These differences could have decreased the users perception of the distance from the target trajectory thus reducing the feedback on their actual performance. Consequently the users performed the task with higher speed. This explanation seems to be endorsed by the statistically higher mean distances recorded in SFHC with both master devices. The differences in mean speed and acceleration between the master devices are affected by the task request: during HC users where slower using PL while significantly faster using SL. On the contrary, the maximal speed for SFHC was obtained with PL, showing how different tasks may require different types of master devices in order to be efficiently executed. No statistical difference was found between the arm stiffness at different levels of speed and acceleration, but the higher end-point stiffness values and variability that were seen for some experiments, suggest that, in those experiments, high stiffness is more likely to occur at lower speed and accelerations. On the other hand, it appears that, even though joint speed and acceleration are fundamental components in the joint stiffness computation, their relation with arm end-point stiffness can't be modeled with simple correlations.

A limitation of this work can be found, first of all, in the small number of subjects; the number of trials for each task may not have been enough to account for the high variability that characterizes human motor control. Another limitation lies in the described differences between the two tasks; the SFHC task, in fact, differs from HC not only for the necessity or re-orienting the tool end-effector, but also in terms of trajectory thickness and tool-tip dimension.

In conclusion, the results obtained suggest that the users tend to modulate the arm endpoint stiffness with respect to different tasks and interfaces and that this modulation is influenced by both the trajectory characteristics and the users' hand kinematics. The users were coping with the difference in task design and master device by adapting their arm stiffness modulation both in terms of central tendencies and variability. Although affected by some limitations, these findings prove that the arm dynamic proprieties are highly variable and that there could be significant benefits from the estimation of the kinetic proprieties of the users' arm during teleoperation. For instance, knowing how the users modulate their stiffness would allow to develop master devices able to match and to enhance this modulation, potentially reducing the energetic cost of the teleoperators while maintaining high precision. The results obtained could also be used to improve human-robot interactions during cooperative tasks, as in [93] and [161].

4.4.1 Future developments

Future studies should focus on further trying to asses the effects of different tasks on the dynamic proprieties of the arm. In order to do so, sets of multiple tasks that require different skills and kinematic solutions should be developed. It would be interesting, for example, to test tasks that focus on rotational movements only, in which the user controls only the tool orientation while different movements and trajectories are imposed. Developing tasks in which rotations on different axis as well as movements on different directions are requested, would allow to test the efficiency of different master devices. Moreover, since actual teleoperated tasks are usually composed of different types of movements, complex, multi-purpose tasks should be developed and assembled to test realistic applications.

An interesting possible future development would be the inclusion in the research of a higher number of subjects as well as expert teleoperators, in order to study and compare the stiffness modulation strategies that they may have developed with expertise. To further understand which are the characteristics and parameters that play a fundamental role in the human-robot interaction, it would also be advisable to study how stiffness relates to other dynamic parameters such as damping and inertia whose relation to human-robot system stability have been recently investigated [198]. These studies proved that the human arm behavior can change from passive to active based on the task performed and on the magnitude of the force perturbation applied.

Disclosure/Conflict-of-Interest Statement

The authors declare that the research was conducted in the absence of any commercial or financial relationships that could be construed as a potential conflict of interest.

Chapter 5

Biomimetic adaptive impedance control in physical Human Robot Interaction

In this chapter a novel impedance controller to regulate the master device's dynamic proprieties based on the estimation of user's arm stiffness is proposed with the aim of improving task performance. A virtual planar reaching task was developed, and the arm end-point stiffness's main axis changes in magnitude and direction was evaluated with the algorithm presented in Chapter 4. Based on the stiffness modulation, the biomimetic variable impedance controller was designed to adapt the master device's damping matrix, creating two different damping fields. In one case the direction of maximal damping was aligned with the estimated direction of maximal stiffness (*Enhancing* field), in the other, maximal damping was generated on the perpendicular to the stiffness main axis (*Isotropic* field). The task performances under the effects of the biomimetic impedance controllers were tested and compared with the *Null* damping condition. The results showed an increase in task performance, in terms of positional error and overshoots, with both biomimetic controllers. The analysis proved the potentiality of the biomimetic impedance modulation controller in terms of execution accuracy.

This work is under submission as: Buzzi, J., Passoni, A., Mantoan, G., Mollura, M. & De Momi, E. "Biomimetic adaptive impedance control in physical Human Robot Interaction", *IEEE International Conference on Biomedical Robotics and Biomechatronics (Biorob)*, 2018.

5.1 Introduction

In the last years, a growing number of applications have showcased the great potentiality of introducing robotic assistances, from manufacturing to automotive, entertainment and health-care. Depending on the application, users and robots interact, sharing mutual information about intentions and internal states. This information can be conveyed through different means of communication, comprising, among the others, visual and audio clues [199, 200], gestures [201], forces and torques [202, 203, 204].

When humans and robots physically interact (Physical Human-Robot Interaction or pHRI), two dynamically and kinematically different entities are coupled, creating a complex system. The effect of the interaction forces on the coupled system's state depend on the relation between the human's dynamic characteristics and the robot's mechanical proprieties. While the first are controlled by the Central Nervous System (CNS) and change with respect to muscular co-contraction and joint configuration [205], based on specific motor control strategies, robot's dynamic behavior is defined by its design and by the type of control adopted. Therefore, when analyzing a pHRI system, along with a complete control over the robot dynamics, a deep understanding of the users motor strategies adopted during the execution of the task is of paramount importance.

Based on the nature of the physical interaction with the robot, different types of pHRI can be identified: firstly, users and robots can interact while performing a common shared task. In this case, users don't hold the robot directly, but forces are exchanged while working on the same shared task i.e. during lifting and handling of heavy objects [206] or when cooperating to assemble parts within an industrial process [207].

Moreover, a rigid connection can be established between human's limbs and robots: this is the case of rehabilitative robotics, where robots are used to help neurological patients in regaining motor capabilities [208] [209].

Users can also interact with robots' end-effectors using handles or directly moving the robots' links, as in teleoperation or shared control. Among the others, in teleoperation, users interact with robots specifically designed to follow and acquire hand movements, functioning as masters to control remotely placed slaves arms [210]. In order to preserve the user's free-hand manipulative skills, master robots shouldn't, first of all, limit the natural dexterity of the arm and should allow for the most intuitive kinematic and dynamic coupling. Many studies focused on the design of master devices to improve user-master robot interaction with the final aim of achieving higher level of dexterity, larger workspaces and higher position/orientation accuracy [179] [211] [212]. Some authors have given emphasis to the ergonomic aspects and user's posture while teleoperating [48] [49], while others have paid attention to the master device handle design [50]. More recently, the effects on the arm kinematics and dynamics induced by different master devices architectures have been studied in order to define which are the characteristics that might effect human motor control strategies [106, 213].

Traditionally, robots are controlled using two main paradigms: admittance and impedance control, reflecting the control over position or forces [214]. While in the first case the robot reaches a desired position and orientation regardless of the forces generated, in impedance control the robot-environment's force exchange is monitored and can be used to modify robots' dynamic proprieties, such as its compliance or damping. In order to assure teleoperation stability while implementing force reflection, high damping coefficients are usually applied to the master device, impairing the possibility of conveying small interaction forces to the user arm [102]. To overcome this limitation, adaptive impedance control was introduced [84, 85]:

a time-varying position-dependent dynamic model of the environment is obtained and used to adapt the master robot impedance. When facing with compliant environments, which are less prone to generate high interaction forces and cause system instability, the master device's damping coefficient is reduced.

While these solutions allowed adaptations to different environments, master devices are, still, completely *unaware* of the continuous dynamic and kinematic changes that users undergo while performing the task. As a promising step toward the possibility of including models of the arm dynamic changes within robot control, biomimetic impedance regulation has been recently proposed [86, 39, 215]. In this control paradigm, dynamic characteristics of the human arm (i.e. arm stiffness) are estimated through the acquisition of bio-signals (such as muscular activations with surface electromyography signals) and are used to modify the slave robot parameters.

In other studies [90, 91], the estimated model of the arm impedance, was used to modify the robot's damping coefficient in cooperative pHRI. In these works, humans interacted with a robotic handle's whose damping coefficient was modulated to match the users arm's stiffness, evaluated using the derivative of the force exchanged by the user and the handle. These works, as well as other similar studies [92, 93], proved the potentiality of creating dynamic models of the human arm to implement controllers that improve task performance in terms of targeting accuracy and reduction of overshoots.

We present the development of a model-based stiffness-mimicking adaptive impedance controller for adjusting the dynamic proprieties of a master device to increase accuracy in a virtual targeting task. Using an off-line musculoskeletal model algorithm based on kinematic and dynamic data, the cartesian hand stiffness modulation was evaluated [105]. The proposed biomimetic controller accounts for the changes in the arm stiffness while performing the task, adapting the master device's damping coefficient in order to reflect the natural, anisotropic, stiffness characteristics. Through experimental acquisitions, we test our main hypothesis that the introduction of the impedance controller will increase users' performance in terms of positional error and overshoots from the targets.

5.2 Materials and Methods

In the experiment users performed a virtual teleoperation targeting task manipulating a 7DoFs master device. Joint angles and surface EMG signals were used to obtain an offline computation of human impedance. From this estimation, the variable impedance controller's damping coefficient modules of the master interface were defined.

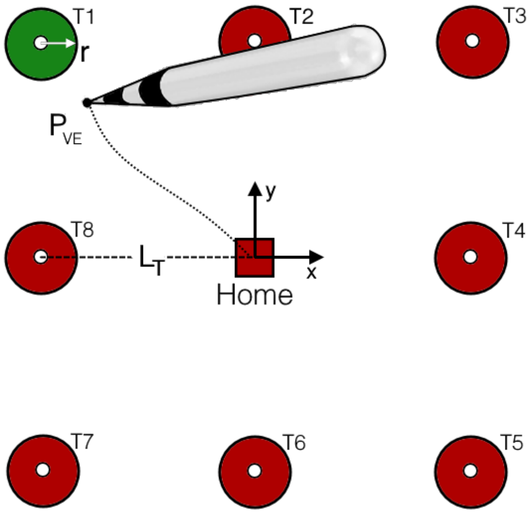

FIGURE 5.1: Starting from the central Home, the user has to reach every single target point T_i (arranged along the sides of a square), positioning the end effector point ($\mathbf{P}_{VE}$) as precisely as possible in the center of the target for *1s* and come back to the Home. Circular targets with a radius $r = 50$mm are are distributed on a square with semi-side $L_T = 300$mm. The virtual reference frame (x-y) is centered on the Home position.

5.2.1 Task design

In the targeting task each user interacted with the master device to move a virtual stylus shaped end effector tool on eight target points ($T_1, T_i, ..., T_T$ with T = 8, see Fig. 5.1). These targets lie on a plane and they are distributed to form a square whose semi-side length L_T is 300mm . Starting from the center of the square, every user was asked to reach each target point (*reaching phase*) and, after having kept the position for 1s (*targeting phase*), to come back to the central "Home" position (see Fig. 5.1). During the task execution, one circle at a time changed color from red to green, guiding the user towards the correct target. Once the target's outer circle ($r = 50$mm) was crossed, users had to place the tool's end effector in the inner circle (white dots in Fig. 5.1) as precisely as possible, while a counter measured *1s* before indicating users to go back to the home position and moving to the next target.

The virtual task was developed using V–Rep (Coppelia Robotics GmbH, Zurich, Switzerland), a robot simulation program that can be interfaced through the Robotic Operating System (ROS) [216] network with the master device and with the data acquisition framework.

5.2.2 Master Device

Users performed the targeting task using the Sigma7 interface (Force Dimension, Nyon, Switzerland), a hybrid parallel/serial link master device, gravity compensated and characterized by 6 DoFs plus 1 grip control, with a resolution of 0.0015mm and 0.013deg and an elliptical dome workspace with radiuses of approximately 190x130mm. The task was designed to fit within the master device workspace in such a way as not to use the device clutching option which decouples the virtual tool position from the master device end effector position.

5.2.3 Stiffness Estimation

The offline stiffness estimation algorithm follows the steps presented in [105]. The users' arm and thorax kinematics are measured using optoelectronic cameras (Vicra – Northern Digital, Ontario, Canada, 20 Hz sampling rate) and electromagnetic sensors (Aurora – Northern Digital, Ontario, 30 Hz sampling rate) and 10 surface EMG signals are acquired using a multichannel ADC (TMSi Porti - Twente Medical Systems International, Oldenzaal, Nederland, 2048Hz sampling rate).

Exploiting an already validated musculoskeletal model [217] developed in OpenSim (see Fig. 5.2), the arm joint angles variations ϑ are computed from the marker movements through inverse kinematics. Using an EMG informed inverse dynamic toolbox [190] the muscle stiffness can be estimated and projected in the joint space using the muscle Jacobian. From the joint stiffness matrix, using the geometric Jacobian, the Cartesian stiffness at the hand has been obtained. To geometrically represent the Cartesian stiffness, using the Singular Value Decomposition (SVD), the left singular vectors and values are extracted. The first singular vector represents the direction and magnitude of the stiffness main axis.

The modulation in the stiffness main axis dimension ($\boldsymbol{K_{max,i}(d)}$) with respect to the x-y distance ($\boldsymbol{d = \sqrt{(P_{x,VE} - T_{x,i})^2 + (P_{y,VE} - T_{y,i})^2}}$) between the target position ($\boldsymbol{T_i}$) and the tool end-effector position ($\mathbf{P}_{\boldsymbol{VE}}$) during task execution was evaluated for the $\boldsymbol{i^{th}}$ target. In the same way, the angle between the main stiffness axis and the x axis from the task reference frame ($\boldsymbol{\hat{\theta}_i}$) for the $\boldsymbol{i^{th}}$ target was projected on the x-y plane and used as indication of the stiffness ellipsoid's direction.

5.2.4 Biomimetic adaptive impedance controller

The estimated changes in the arm stiffness are used to tune the master device's damping matrix (see Fig. 5.2). Humans increase arm stiffness in order to achieve high precision during the execution of targeting tasks, increasing stability against internal and external noise. The proposed biomimetic impedance controller correspondingly increases the master device's damping coefficients, increasing the forces needed to maneuver the robot's handle thus reducing the effects of unwanted hand movements.

The force generated by the master device ($\mathbf{F}(\boldsymbol{t})$) at the $\boldsymbol{t^{th}}$ time frame can be expressed as sum of elastic, damping and inertial components:

$$\mathbf{F}(t) = \mathbf{K} \cdot \mathbf{P}_{MD}(t) + \mathbf{D} \cdot \dot{\mathbf{P}}_{MD}(t) + \mathbf{I} \cdot \ddot{\mathbf{P}}_{MD}(t) \tag{5.1}$$

Where **K** is the elastic coefficient matrix, **D** is the robot's damping matrix, **I** is the robot's matrix of inertia (see Fig. 5.2), $\mathbf{P}_{MD}(t)$ and $\ddot{\mathbf{P}}_{MD}(t)$ are the Master Device (MD) end-effector position and acceleration in the MD reference frame.

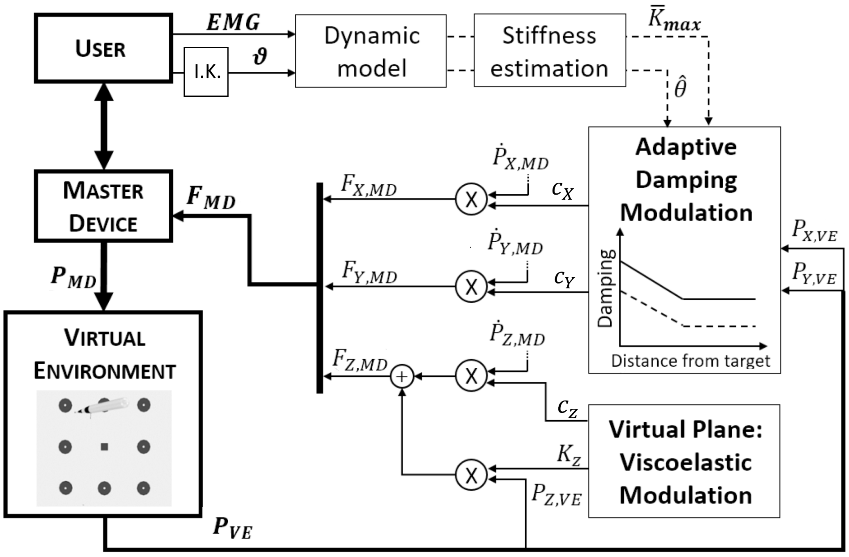
USER
EMG
I.K.
ϑ
Dynamic model
Stiffness estimation
$\bar{K}_{max}$
$\hat{\theta}$
Adaptive Damping Modulation
Damping
Distance from target
MASTER DEVICE
F_{MD}
P_{MD}
VIRTUAL ENVIRONMENT
$\dot{P}_{X,MD}$
$F_{X,MD}$
c_X
$\dot{P}_{Y,MD}$
$F_{Y,MD}$
c_Y
$\dot{P}_{Z,MD}$
$F_{Z,MD}$
c_Z
K_Z
$P_{Z,VE}$
$P_{X,VE}$
$P_{Y,VE}$
Virtual Plane: Viscoelastic Modulation
P_{VE}

FIGURE 5.2: Schematic of the biomimetic adaptive impedance controller: using joint angles (ϑ) and EMG signals combined with an EMG informed inverse dynamic algorithm, users' stiffness is estimated. Mean stiffness modulation ($\bar{K}_{max}$) and orientation ($\hat{\theta}$, with respect to the virtual plane x axis) are used to generate the adaptive damping modulation (c_x, c_y). The master device's speeds on the x-y plane ($\dot{P}_{x,MD}$,$\dot{P}_{y,MD}$) are used to compute the corresponding damping forces ($F_{x,C}$,$F_{y,C}$). Similarly, a viscoelastic virtual plane produces forces along the Z axis ($F_{z,MD}$) obtained from the sum of the elastic (k_z) and damping (c_z components)

The damping component of the forces generated by the adaptive impedance controller ($\mathbf{F}_C(d,t) = \mathbf{D} \cdot \dot{\mathbf{P}}_{MD}(t)$) as a function of the distance from the target d and the t time frame can be obtained as follows:

$$\mathbf{F}_C(d,t) = \mathbf{C}(d) \cdot \dot{\mathbf{P}}_{MD}(t) \cdot \mathbf{R}_z(\psi_i) \tag{5.2}$$

where $\mathbf{C}(d)$ is the damping coefficients matrix, $\dot{\mathbf{P}}_{MD}(t)$ is the MD end-effector speed and $\mathbf{R}_z(\psi_i)$ is the 3x3 rotation matrix around the z-axis that is used to rotate the damping coefficients direction on the x-y plane (see Fig. 5.3B).

The same equation can be also expressed as:

$$\begin{bmatrix} F_{x,C}(d,t) \\ F_{y,C}(d,t) \\ F_{z,C}(d,t) \end{bmatrix} = \begin{bmatrix} c_{min}(d) & 0 & 0 \\ 0 & c_{max}(d) & 0 \\ 0 & 0 & c_z \end{bmatrix} \cdot \begin{bmatrix} \cos(\psi_i) & -\sin(\psi_i) & 0 \\ \sin(\psi_i) & \cos(\psi_i) & 0 \\ 0 & 0 & 1 \end{bmatrix} \cdot \begin{bmatrix} \dot{P}_{x,MD}(t) \\ \dot{P}_{y,MD}(t) \\ \dot{P}_{z,MD}(t) \end{bmatrix} \tag{5.3}$$

where $c_{min}(d)$ and $c_{max}(d)$ represent the adaptation of the module of the two axes of damping (along x and y) with respect to changes in the target-tool distance d. In order to reflect arm stiffness' anisotropy, we generated a non-isotropic elliptical damping field, whose axis dimensions (c_{min} and c_{max}) are tuned to match the changes in the mean arm stiffness module $\bar{K}_{max}$ when approaching targets. c_z represents the constant damping coefficient that we used to avoid possible instability caused by the elastic virtual plane (see 5.2.5).

At d^{th} distance from the target, c_{min} and c_{max} are defined as follows:

$$c_{min}(d) = \begin{cases} c_{min,1} & d \geq L_T/2 \\ c_{min,0} - \frac{(c_{min,0} - c_{min,1}) \cdot d(t)}{L_T/2} & d < L_T/2 \end{cases} \tag{5.4}$$

$$c_{max}(d) = \begin{cases} c_{max,1} & d \geq L_T/2 \\ c_{max,0} - \frac{(c_{max,0} - c_{max,1}) \cdot d(t)}{L_T/2} & d < L_T/2 \end{cases} \tag{5.5}$$

Where $c_{min,0}$ and $c_{max,0}$ are respectively the maximal and minimal values of c (when $d = 0$) and $c_{min,1}$ and $c_{max,1}$ are the minimal and maximal values of c (when $d = L_T$).

The maximal damping variation ($\Delta c_{max} = c_{max,0} - c_{max,1}$) was obtained from the estimated variation of maximal stiffness $\Delta K_{max} = K_{max,0} - K_{max,1}$ as follows:

$$\Delta c_{max} = \Delta K_{max} \cdot s_{max} \tag{5.6}$$

Where $s_{max} = \frac{3}{2} \frac{s}{m^2}$ is the scaling coefficient that converts the arm stiffness modulation into the master device's damping modulation. In the same way, for Δc_{min}, a scaling factor $s_{min} = \frac{3}{4} \frac{s}{m^2}$ was used.

The resulting variation of maximum and minimum components of the damping coefficient as a function of d is shown in Fig. 5.3.A.

Two different damping fields were generated:

Enhancing damping field

In the first case, the maximal damping coefficient is directed along the axis of maximal stiffness. This can be achieved imposing $\psi = \bar{\theta}_i$ in Eq. 5.3 , therefore applying rotations around the z axis equal to the displacement between the main axis of stiffness and the x axis ($\bar{\theta}_i$) for each of the eight targets (see Fig. 5.3.B, green ellipse) . The effects of this damping field enhance the natural stiffness directionality, increasing the effect of the stiffness ellipsoid anisotropy.

Isotropic damping field

In the second case, the maximal damping coefficient is directed along the perpendicular to the stiffness main axis, imposing $\psi = \bar{\theta}_i + \pi/2$ (see Fig. 5.3.B, blue ellipse).

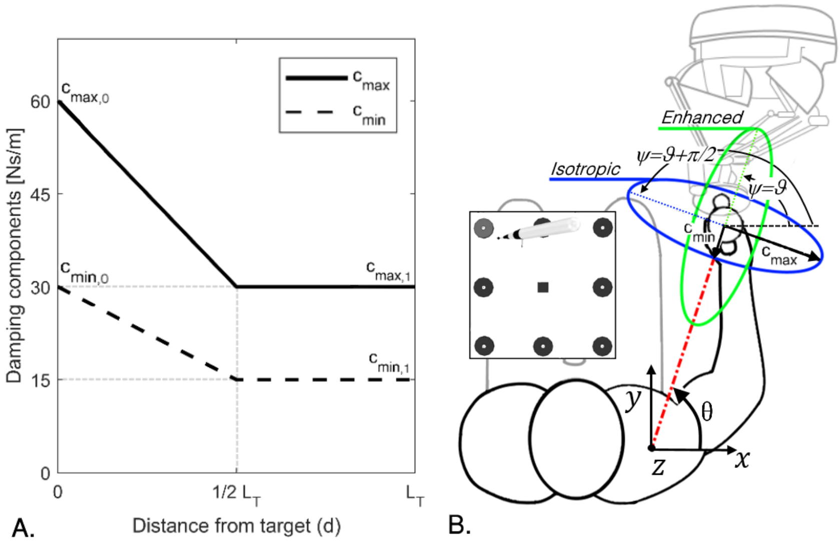

FIGURE 5.3: **A**. c_{max} and c_{min} as function of d. **B**. Subject posture during task execution. The main axis of the stiffness ellipse (red dash-dot line), corresponds to the shoulder-hand direction. In green: the *Enhancing* damping coefficient field, in blue, the *Isotropic* one.

In this case, we aim at obtaining a more isotropic workspace for the user hand by summing the effects of the natural impedance control with the controller generated damping forces.

5.2.5 Visco-elastic Plane

Perpendicularly to the virtual plane of the task (*x*-*y*), a viscoelastic force is applied in order to help the user to steady the tool-tip $P_{z,MD}$ on the z dimension. This solution was introduced to compensate for the lack of 3D perception that users suffered while performing the tasks on a flat bi-dimensional screen. The elastic component of the force generated by the master device $\mathbf{F}_{K,MD}$ can be expressed as follows:

$$\mathbf{F}_{K,MD} = \begin{bmatrix} 0 & 0 & 0 \\ 0 & 0 & 0 \\ 0 & 0 & k_z \end{bmatrix} \cdot \begin{bmatrix} P_{x,MD} \\ P_{y,MD} \\ P_{z,MD} \end{bmatrix} \tag{5.7}$$

Where k_z is the elastic coefficient whose value was experimentally defined. Therefore, the total force along the z axis that is generated in each time frame to create the virtual plane, comprises a damping and an elastic component as follows:

$$F_{Z,MD}(t) = k \cdot P_{z,MD}(t) + c_z \cdot \dot{P}_{Z,MD}(t) \tag{5.8}$$

5.2.6 Experimental protocol

Since an off-line method for the estimation of the arm end-point stiffness was adopted, the biomimetic adaptive impedance controller's effects were evaluated on a successive experimental session.

Arm stiffness estimation

For the stiffness characterization, we recruited 7 healthy subjects (4 female and 3 male, mean age *23* ± *1.5*y.o) Each user was seated in a comfortable chair in front of a monitor and, after having been instructed about the task he/she was going to perform, he/her was asked to execute 10 trials while trying to maintain the hand movement on a constant plane. The monitor was put as flat as possible to make it parallel to the pane in which the task was performed.

Variable impedance controller

For testing the performance of the stiffness-based variable impedance controller, we recruited 12 right-handed subjects (4 females and 8 males, mean age 24 ± 2.8y.o.) who had no experience with the master controller. Each subject performed 10 trials of the same virtual task under 3 different force conditions (30 overall repetitions): no impedance regulation (*Null*), *Enhancing* damping field and *Isotropic* damping field. The execution order was randomized, assuring to have the three different conditions tested an equal overall number of times.

All the involved subjects provided informed written consent, in accordance with the recommendations of Politecnico di Milano Ethical committee Board. All subjects gave written informed consent in accordance with the Declaration of Helsinki.

5.2.7 Performance Indexes

To assess each subject's performance during task execution, the following indexes were evaluated for each damping field condition:

- Maximal Error ($E_{max,i}$): Maximal distance from the i^{th} target during the *targeting* phase.

  $$E_{max,i} = \max_{[t_c:t_{off}]} d(t) \tag{5.9}$$

  Where t_c and t_{off} are, respectively, the time frames when the *targeting* phase starts and ends.

- Integral Error ($E_{int,i}$): Error computed as integral of the distance from the i^{th} target normalized by the duration of the resting phase.

  $$E_{int,i} = \frac{\int_{t_c}^{t_{off}} d(t)dt}{t_{off} - t_c} \tag{5.10}$$

- Unacceptable Error ($E_{u,i}$): Error computed as for E$_{int,i}$, but considering only the distances from the i^{th} target higher than the radius of the target *r*.

$$E_{u,i} = \frac{\int_{t_c}^{t_{off}} d(t)dt}{t_{off} - t_c} \quad d(t) > r \tag{5.11}$$

- Overshoots (*O*): Number of times that the subjects went out from the i^{th} target during the resting phase.

- Normalized Traveled Length (*NTL*): Normalized length of the path traveled by the subjects during each reaching phase; it is expressed as:

$$NTL_i = 1 - \frac{\sum_{k=1}^{N}\sqrt{\Delta P_{x,VE,i}^2 + \Delta P_{y,VE,i}^2}}{L_T} \tag{5.12}$$

  Where N is the number of sampled positions of the virtual tool tip during the *reaching* phase, $\Delta P_{x,VE,i}$ and $\Delta P_{y,VE,i}$ represent the variation in the x and y components of the tool's end-effector position in the virtual environment reference frame (VE) with respect to the previous $(k-1)^{th}$ sample.

- Reaching Time ($t_{R,i}$): Time needed to reach the i^{th} target from the center position.

$$t_{R,i} = t_c - t_{on} \tag{5.13}$$

  Where t$_{on}$ and t$_c$ are, respectively, the time frames when the *reaching* phase and the *targeting* phase starts.

5.2.8 Results analysis

Stiffness Estimation

The *reaching* and *targeting* phases of the task were extracted for each subject, repetition and i^{th} target. The stiffness ellipsoid's main axis dimension $K_{max}(d)$ and direction $\hat{\theta}(d)$ were extracted and, for each subject, their distribution normality between different repetitions was evaluated (Lilliefors test, $\alpha = 0.05$). Since the data, for all the subjects, was normally distributed, the mean stiffness main axis dimension for each target throughout the normalized time was obtained $\bar{K}_{max,i}(d)$ as well as the mean direction of stiffness for each target $\bar{\theta}_i(d)$.

Since the same stiffness modulation was observed for all the targets, a single modulation $\bar{K}_{max}(d)$ was obtained from the mean through the eight targets directions. Linear regression was used to describe the $\bar{K}_{max}(d)$ modulation. No significant changes in the $\bar{\theta}_i(d)$ were seen throughout the task progression, with the data appearing normally distributed (Lilliefors test, $\alpha = 0.05$), therefore, a single mean value of $\bar{\theta}_i$ was extracted for each target.

Variable impedance control performances

The first experimental session, for each subject, regardless of the force condition (*Null*, *Enhancing* or *Isotropic*) was considered as a training phase during which users had time to familiarize with the master device and with the task. For this reason, the first experimental session was excluded from the analysis.

For each index, within the same subject and force condition, the data distribution through the 10 repetitions was evaluated (one-way ANOVA, $\alpha = 0.05$). Since in some cases the first repetition of each force condition was found to be significantly different from the others (Tukey's range test $\alpha = 0.05$) nine task repetitions (2:10) were considered for the analysis.

For each user and each of the eight targets, the statistical distribution for the nine considered repetitions of the aforementioned indexes was evaluated using a normality test (Lilliefors $\alpha = 0.05$). Since the data distribution was normal, and no significant differences were found between different targets, the mean value for each subject and force was extracted. The differences between the three force conditions for each index were evaluated using a one-way ANOVA test (α = 0.05), followed by post-hoc analysis (Tukey's honestly significant difference procedure $\alpha = 0.05$).

The effects of hand speed over the task performance in the three damping conditions was also analyzed. The mean hand speed for each user over the ten repetitions of each experiment was compared against the performance evaluated with the different indexes. Anyway, no significant interaction between speed and performance was found in any of the experiments for all the indexes considered, this analysis, was, therefore, discarded.

All the inferential statistic analysis were conducted with the Statistics and Machine Learning Toolbox for Matlab 2017b (Mathworks, Natick, Massachusetts, US)

5.3 Results

5.3.1 Stiffness Estimation

The mean stiffness modulation profile $\bar{K}_{max}(d)$ with respect to d, as well as the first and third quartiles, are shown in Fig 5.4. While in the first part of the movement, (from 0 to $\frac{1}{2}L_T$) $\bar{K}_{max}$ is constant in both mean and interquartile range, an ascending trend can be observed in the second half of the movement and a linear regression approximates this part of task ($\rho = 0.887, p = 0.0003$ see red line in Fig. 5.4).

The stiffness ellipsoids orientations were found to be normally distributed (Lilliefors test, $\alpha = 0.05$), therefore, the mean orientation was extracted for each target. $\bar{\theta}_i$ (angle between the stiffness main axis and the x axis in the task's reference frame) ranges between 50 and 60 deg (see Fig. 5.4.B), grossly overlapping with the shoulder-hand direction.

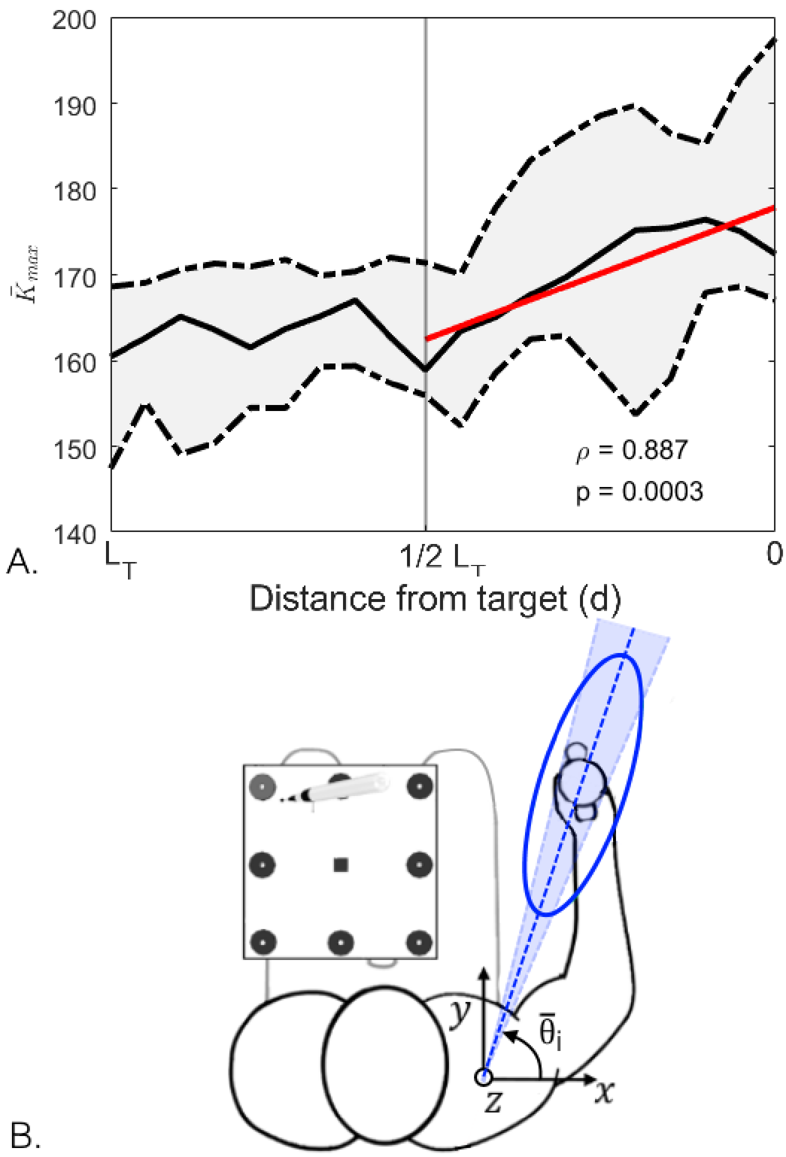

FIGURE 5.4: Mean stiffness modulation profile and stiffness ellipsoid orientation. **A.** the solid black line represents the mean stiffness $\bar{K}_{max}$(d) over the different targets, while the dashed black lines represent the first and third quantiles. The solid red line shows the linear regression, whose significance (p) and ρ values are also reported. **B.** The main axis of the mean stiffness ellipsoid is represented with a dashed line along the shoulder-hand direction. $\bar{\theta}$ is the angle between the task's x-axis and the direction of maximal stiffness. The shaded area represents $\bar{\theta}$ variability around the mean

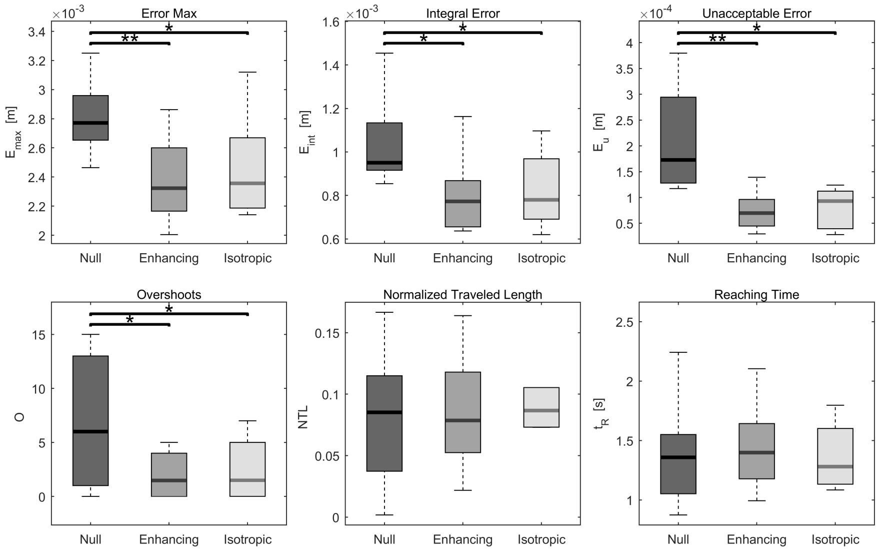

FIGURE 5.5: Statistical distributions for the three force conditions throughout the six indexes analyzed. Statistical significance (evaluated with one way-ANOVAs and post-hoc tests) is indicated with lines and stars (* for $p < 0.05$, ** for $p < 0.01$)

5.3.2 Variable impedance control performances

Figure 5.5 shows the inter subjects variability for each index's mean value. The *Null* damping condition shows worst results in terms of Maximal Error (E_{max}) with respect to the *Enhancing* (*p = 0.006*) and the *Isotropic* (*p = 0.026*) damping fields. Under the *Null* damping condition users showed a median E_{max} of *2.78*mm while targeting the center of the *30*mm circular target. While performing the task with the biomimetic variable impedance controllers, this error was reduced to less than *2.35*mm (corresponding to a 15.5% increase in targeting accuracy).

Similar results can be seen in the Integral Error (E_{int}) (*p = 0.022* with respect to *Enhancing* and *p = 0.045* with respect to *Isotropic* damping field) and in the Unacceptable Error (E_u) (*p = 0.004* with respect to *Enhancing* and *p = 0.024* with respect to *Isotropic* damping field). For the E_u, the *Null* condition is characterized by a larger interquartile distance. A very similar trend is seen in the Overshoots index (O), where the *Null* damping condition shows significant worse performance with respect to the *Enhancing* (*p = 0.013*) and *Isotropic* (*p = 0.043*) conditions and larger interquartile distance. While users overshot targets around one time under the effects of the biomimetic variable damping controllers, when no damping was applied users surpassed the target around six times during task repetitions.

On the other hand, no differences were found in terms of Normalized Tool movement Length (NTL) and target reaching time (t_R) although, for the *Isotropic* damping condition, the NTL interquartile range is significantly smaller.

No significant differences between the *Enhancing* and *Isometric* damping fields were found. A very small, non significant trend can be seen in E_{max}, E_u and for the Overshoots, where the median and mean index values for the *Isotropic* damping field are slightly higher with respect to the *Enhancing* condition. On the contrary, for the reaching time t_r, the minimal mean value was achieved under the *Isotropic* force condition.

5.4 Discussion

The arm stiffness modulation was evaluated in terms of maximal value and main axis direction during the execution of a teleoperated targeting tasks. The results showed an increase in the arm stiffness when approaching the targets, while a rather constant main axis direction was maintained through the different targets. From the results it can be inferred that in the first part of the reaching task the maximal stiffness exerted by the users is almost constant: users are still relatively far from the target, producing a fast movement rather than a precise one. While approaching the target, maximal stiffness increases, reflecting, as expected, the necessity of increasing the hand stability against internal and external noise, to achieve greater precision.

Regarding the stiffness main axis direction, the results showed no significant differences in the ellipsoids mean orientation among different targets because of the very slight changes in the joint configuration of the arm required by the task in reaching the different target points. The direction along which subjects exerted the maximal stiffness modulation was the shoulder-hand one in accordance with previous studies [218, 132, 219, 172].

From this modulation, a biomimetic variable impedance controller for the master device was developed and tested. The results showed that the biomimetic impedance modulation increased users targeting performances. The damping positively influenced users performance, both in terms of maximal displacement from the task goal, as well as in their capability of finely finding the center of the targets' circle during the given time.

The mean number of overshoots per experiment shows that the variable impedance control allows users to perform significantly better while introducing no significant differences in terms of end effector's traveled length nor reaching time: users were therefore facilitated in finding an advantageous kinematic and dynamic matching with the master device.

The results obtained are in accordance with previous experiments: in [93], Beretta et al., showed that the introduction of a variable impedance controller increased expert and naive users performance during a human-robot cooperative point targeting task. In the aforementioned analysis, a robotic arm damping matrix was modulated isotropically based on an a priori knowledge of the task performed, which requested an increased precision in its final line-following part. Coherently, a similar study from Duchaine and Gosselin showed how the introduction of an arm stiffness based adaptation of a robotic handle damping factor led to significant improvements in terms of overshoots reduction in a cooperative drawing task [91].

No significant differences between the *Enhancing* and *Isotropic* force conditions was found: users behaved similarly when facing an augmentation of the natural arm stiffness (achieved when the maximal damping was aligned with the direction of maximal stiffness) and when the same damping was directed along the perpendicular to the stiffness main axis. This results may be interpreted in different ways: first of all it is possible that the difference between the damping coefficient's magnitude in the two directions is too small to introduce significant effects in the arm and hand dynamics. It is, therefore, possible that higher damping coefficients would lead to different results. Another possible reason may be found in the capability of the human arm to cope with different robot's dynamics while achieving similar results: with both force fields, users seemed to benefit from the overall increase in damping regardless of its anisotropy and orientation. Lastly, differences between the *Isotropic* and *Enhancing* damping fields might be seen when different hand velocities are considered. In the analysis presented, limited differences in the hand velocities profiles have been registered and no significant behaviors were seen in the comparison between the slower and faster movements. Anyway, it is possible that, imposing different velocities profiles to the users, introducing, for example, tracking or cursor-chasing tasks, more differences would be found in the two proposed implementations of the damping fields.

A limitation of the present work can be found in the absence of a real-time estimation of the arm stiffness during the execution of the task. In fact, due to the offline nature of the arm's stiffness estimation adopted, two separated subsequent experiments had to be conducted, involving different subjects. This solution implies the necessity of approximating the diverse dynamic modulations that different users might exhibit to a common trend, which defines the changes in the damping coefficients presented. The adoption of an online stiffness estimation method (as in [76]), could, instead, preserve and take into consideration inter subjects' dynamic variability, possibly magnifying the effects of the biomimetic impedance controllers.

Future work should, therefore, focus on the development and implementation of real-time algorithms to estimate arm stiffness during task execution: a machine learning approach could be, for example, explored. A subject specific initial phase of calibration could be implemented using traditional frequency-based analyses to estimate the arm dynamic proprieties. The use of a force sensor to record arm-robot interaction forces, coupled with the application of known hand displacements, would allow to generate the ground truth that can be used to train the on-line stiffness estimation algorithm. This approach would allow to acquire different kind of signals, ranging from the arm joint angles to multiple EMG recordings that could be used to infer the arm stiffness during task execution.

The real-time stiffness estimation would also allow to develop biomimetic controllers that can adapt the master device dynamics to unknown, unplanned tasks or to those activities where limited a-priori knowledge of the task environment is available. This is the case, for example, of surgical teleoperation procedures, where it's hard to define predetermined tools trajectories and sub-task due to the natural differences between patients as well as due to the numerous possible complications that can occur through the surgery. The control of the robot's dynamic proprieties could also be extended to the inertia: in redundant robots it would be possible to match the user's inertia changing the robots configuration.

5.5 Conclusions

In the present work we developed and tested two implementations of an adaptive impedance controller in HRI during the execution of a virtual planar targeting task. The arm stiffness modulation main axis dimension and direction were evaluated through a musculoskeletal model approach based on acquired kinematic and dynamic data. In a follow-up experiment, the stiffness modulation was matched with corresponding changes in the master device's impedance parameters, creating two damping fields: one directed along the estimated stiffness main axis, the other perpendicular to it. In accordance with previous literature, the results showed that users benefited from the variable impedance controller in terms of positional error and overshoots but no significant difference was found between its two implementations.

Regarding the possibility of finding differences between the two biomimetic impedance regulation strategies presented, the results suggest that further analysis should be conducted, involving higher values of damping coefficients, increasing the damping fields eccentricity or studying more complex tasks.

Chapter 6

Conclusions

This PhD thesis investigated physical human robot interaction in teleoperation, with the aim of exploring the motor control strategies that teleoperators adopt, comparing different master device's designs and developing novel control architectures to enhance this interaction.

Recently, the remarkable growth of teleoperation applications in many different fields, has increased the necessity of improving the interaction between human arm and robotic master devices. While multiple studies focused on the optimization of the master device's mechanical characteristics to achieve large workspaces and high precision, limited researches explored the effects of the hand-robot physical interaction over the users' motor skills. Despite being designed to preserve the natural hand motion, as well as to be as intuitive as possible, some researches [126, 127] demonstrated that expert teleoperators have to develop new motor skills in order to achieve proficiency in the execution of teleoperated tasks. These findings proved the existence of a gap between natural, free-hand task execution and teleoperation performed through the interaction with the master device. In order to improve the effectiveness of teleoperation, and, therefore, facilitate its development in even more applications, master devices should not only preserve the natural motor control strategies, but, also, enhance them. To do so, master devices should achieve higher levels of *awareness* with respect to the kinematic and dynamic changes that humans' arm undergo while performing a complex task.

To this end, in Chapter 2, the analysis firstly demonstrates the effects of the different tasks types over the possibility of fully exploiting arm's kinematic redundancy. The analysis also presents the effects of different master device's designs over the level of redundancy exploitation that can be achieved, suggesting that different designs may be suitable for different application. In Chapter 3 and 4 the dynamic aspects of human motor control are analyzed, studying arm stiffness variations during the execution of different tridimensional and bidimensional tasks. The results show that arm stiffness is modulated with respect to the task characteristics, both in terms of magnitude and main axis direction. Moreover, based on the type of task, different master device's kinematic and dynamic proprieties may influence the level of arm stiffness that users exerted. In Chapter 6, the acquired knowledge over the arm stiffness modulation is used to design a biomimetic controller to improve performances in a virtual targeting task, proving the feasibility of enhancing HRI through the obtainment of an in depth knowledge of the users' arm internal state.

6.1 Thesis Contributions

This PhD research focuses on the analysis of the kinematic and dynamic aspects of motor control that are involved in teleoperation. The effect of different master devices and tasks over the arm joint configurations and end-point stiffness modulations are studied, drawing suggestions over master devices' design and control.

To study the kinematic motor control strategies, we used the UCM analysis to explore the differences induced by diverse task space dimensions and constraints and by two master devices on teleoperators' capabilities to exploit arm redundancy. In order to study the different task spaces, we validated different algorithms to estimate the Jacobian matrix associated with the motion, enabling the possibility of studying tasks which involve mixed position/orientation constraints. The analysis underlines the importance of the arm redundancy exploitation motor strategy, which must be preserved to achieve a functional human-master robot interaction. In fact, especially during mixed position-orientation manipulations, users rely on this motor strategy, exploiting arm redundancy to a greater extent in order to perform the task. The conservation of the redundancy exploitation motor strategy would also increase task performance as the correlation between task performance and the level of arm redundancy exploitation in position-only tasks demonstrates. Moreover, the analysis showcased the capability of the human motor control system to adapt to different master device designs; the overall level of redundancy exploitation is, in fact, unaffected by the mechanical characteristics of the master devices. On the other hand, looking at the two tasks separately, the analysis shows that serial link master devices with a stylus shaped end-effector might allow for maximal redundancy exploitation for position only tasks, while hybrid parallel-serial link devices, characterized by hand centered rotations, are more effective in mixed position-orientation task. In fact, due to the stylus shaped end effector, in the serial link master device the decoupling of position and orientation is less intuitive, with rotations that are not centered in the hand. The stylus end-effector, on the other hand, allows a grip usually adopted while holding a pen, therefore, it grants an easier control over position with respect to the handle adopted in the hybrid parallel-serial link master devices.

In Chapters 3 and 4, the study of the dynamic motor strategy that modulates arm impedance is performed for two different tasks with different control strategies. Through a musculoskeletal model approach, an offline estimation of arm stiffness is presented. Both the analysis prove that tasks characteristics have an impact not only on the arm impedance control, but also on how human motor control is able to compensate for dynamic differences between different master devices. In particular, when performing complex tridimensional tasks, as in the case of the stitching mimicking virtual task presented in Chapter 3, users rely on an increase of arm stiffness when teleoperating with the serial link master device, compensating for its low inertia and low mechanical stiffness. On the other hand, the hybrid parallel-serial link master device, which shows higher mechanical stiffness and apparent mass, allows for the same arm dynamic modulation as in the free-hand task execution, while increasing task accuracy at the same time. A reason to explain this difference may lie in the orientational nature of the stitching task that favors the hand-centered rotations allowed by the hybrid parallel-serial link master device. In Chapter 4, the stiffness analysis is applied to an eight-shaped bidimensional position only line following task and to a position-orientation bidimensional line following task. Contrary to what found in the tridimensional stitching mimicking task, when dealing with bidimensional tasks, the differences in the master device's dynamic and kinematic proprieties doesn't affect stiffness modulation. Human motor control is therefore capable of compensating for mechanical and design differences between master devices, but this adaptability is reduced when dealing with strict task requirements. Moreover, the results confirm the tight relation between task characteristics and arm end-point stiffness modulation: coherently with the literature, users increase stiffness when facing complex, high curvature portion of the trajectory, on the other hand, the necessity of rotating the wrist, as requested by the position-orientation task, reduces the possibility of increasing arm stiffness. Due to this, tasks that require high dexterity, and complex writs movements are more likely to be affected by external and internal noise.

In Chapter 5, a stiffness based biomimetic adaptive impedance controller for master devices is presented. In this section, the informations achieved in the previous chapters are combined to create a controller that increases users' performance in a virtual targeting task. The arm stiffness modulation is estimated using the non disruptive offline method presented in Chapter 4. Coherently with the existing literature, the results show that users increased the arm stiffness when approaching targets, in order to achieve the high positional accuracy requested by the task. The evaluated stiffness modulation is used to define two different approaches to the biomimetic impedance controller: in the first case, a variable damping field is oriented in the same direction as the main axis of stiffness, while in the second case, the damping field is perpendicular to the stiffness main axis direction. In both cases, following the arm stiffness modulation, the module of the damping coefficients is increased while approaching the targets. The great potentiality of biomimetic controllers is underlined by the increased performances in the targeting task execution: the positional errors, as well as the overshoots, are significantly reduced with both damping fields. Contrary to the use of high, isotropic damping factors, the reaching time as well as the normalized tool movement length remain unchanged with respect to the absence of damping fields. Users benefited from the overall increase in the damping factor without preferring either of the two biomimetic impedance controllers proposed. This result may imply that the two approaches to damping modulation are equally feasible or that the differences between the two damping fields generated are too small to affect arm motion, pointing out the necessity of further researches.

The overall results highlight the benefit of achieving an in-depth knowledge of the arm's control strategies adopted during teleoperation and, more in general, in HRI. Studying the task requirements and its constraints, it would be possible to suggest the master robot design that best fits the application. Moreover, the incorporation of human motor control principles into the design of robot controllers would lead to an effective human-in-the-loop control, which would improve the human-master robot interaction, its intuitiveness and, thus, task performances.

6.2 Future Perspective

In the near future, robots will most likely blend with humans in an increasing number of everyday life applications. This trend, that can be already observed in industry [220] as well as in healthcare [221], is justified by robots' great capabilities in supporting and augmenting users' physical capabilities. With the growth of possible applications, and the development of technological advancements that will fix current technical limitations, the research will focus on understanding the social, behavioral and physical human-robot interaction dynamics.

In this perspective, the proposed work represents a portion of a wider framework that aims at developing a new generation of robotic interfaces capable of being *aware* of all the motor control strategies that undergo the execution of a complex task. In order to achieve this goal, in my opinion, new metrics are required to objectively estimate the level of intuitiveness, transparency, and, more in general, interaction performance that users reach with a master device in the execution of a specific task. In this sense, the UCM analysis presented in Chapter 2 is one of the possible tools that could be used to estimate how well a master device preserve kinematic strategies.

Some considerations must be taken regarding OpenSim, the musculoskeletal model simulator that has been used throughout the analysis to obtain estimations of arm's dynamic proprieties. Although this platform represents a powerful tool to explore the arm's behavior in different conditions, it is also affected by clear limitations. First of all, although mitigated by the scaling tool, the software capabilities in accounting for the natural variability that characterizes human motor control are limited: the muscle activation patterns, as well as the muscle fibres parameters are normalized to standard values, which might be different from the subjects characteristics. Moreover, OpenSim analysis require an intense computational phase, which can't be easily adapted for real-time estimations. Therefore, for these reasons, new ways of estimating the arm's dynamic parameters must be adopted: through calibration phases, the arm configuration as well as the muscular activity should be related to the arm stiffness, estimated with traditional techniques. It would be possible, i.e., to train machine learning algorithms to infer arm stiffness from a variety of biological signals acquired during task execution.

In this sense, the recent introduction of robust realtime estimations of the arm's dynamics [76], and the encouraging results obtained with the adoption of biomimetic impedance controllers [222, 223, 224], motivates the necessity of exploring the possibilities offered by non-traditional control schemes. In fact, inferring the dynamic characteristics of human movements will allow robots to generate a more specific and advantageous assistance, possibly increasing comfort and task performances while reducing users' muscular effort. Since this assistance is based on users' motor control adaptations, it doesn't require any a priori knowledge of the task, showcasing the viability of this approach to complex, unplanned tasks as the one often encountered in surgery.

Bibliography

[1] Satoshi Hoshino, Hiroya Seki, and Yuji Naka. “Development of a flexible and agile multi-robot manufacturing system”. In: *IFAC Proceedings Volumes* 41.2 (2008), pp. 15786–15791.

[2] Joost Broekens, Marcel Heerink, Henk Rosendal, et al. “Assistive social robots in elderly care: a review”. In: *Gerontechnology* 8.2 (2009), pp. 94–103.

[3] Greg Chance et al. “a Quantitative analysis of Dressing Dynamics for robotic Dressing assistance”. In: *Frontiers in Robotics and AI* 4 (2017), p. 13.

[4] Daniel Göhring et al. “Semi-autonomous car control using brain computer interfaces”. In: *Intelligent Autonomous Systems 12* (2013), pp. 393–408.

[5] Maria Nani et al. “MOBISERV: an integrated intelligent home environment for the provision of health, nutrition and mobility services to the elderly”. In: (2010).

[6] Anthony R Lanfranco et al. “Robotic surgery: a current perspective”. In: *Annals of surgery* 239.1 (2004), pp. 14–21.

[7] Kazuhiro Kosuge and Yasuhisa Hirata. “Human-robot interaction”. In: *Robotics and Biomimetics, 2004. ROBIO 2004. IEEE International Conference on*. IEEE. 2004, pp. 8–11.

[8] Holly A Yanco and Jill Drury. “Classifying human-robot interaction: an updated taxonomy”. In: *Systems, Man and Cybernetics, 2004 IEEE International Conference on*. Vol. 3. IEEE. 2004, pp. 2841–2846.

[9] Thomas B Sheridan. “Human–robot interaction: status and challenges”. In: *Human factors* 58.4 (2016), pp. 525–532.

[10] B Howard Cary and C Scott. “Helzer”. In: *Modern Welding Technology, Upper Saddle River, New* (2005).

[11] KM Haugan. “Spray painting robots: advanced paint shop automation”. In: *Industrial Robot: An International Journal* 1.6 (1974), pp. 270–272.

[12] Lanson Y Shum. *Pick and place robot*. US Patent 4,398,863. 1983.

[13] Zhangfeng Ju, Chenguang Yang, and Hongbin Ma. “Kinematics modeling and experimental verification of baxter robot”. In: *Control Conference (CCC), 2014 33rd Chinese*. IEEE. 2014, pp. 8518–8523.

[14] Ronald Wilcox, Stefanos Nikolaidis, and Julie Shah. “Optimization of temporal dynamics for adaptive human-robot interaction in assembly manufacturing”. In: *Robotics Science and Systems VIII* (2012), pp. 441–448.

[15] Noriaki Mitsunaga et al. “What makes people accept a robot in a social environment-discussion from six-week study in an office”. In: *Intelligent Robots and Systems, 2008. IROS 2008. IEEE/RSJ International Conference on*. IEEE. 2008, pp. 3336–3343.

[16] Cynthia Breazeal and Brian Scassellati. “How to build robots that make friends and influence people”. In: *Intelligent Robots and Systems, 1999. IROS'99. Proceedings. 1999 IEEE/RSJ International Conference on*. Vol. 2. IEEE. 1999, pp. 858–863.

[17] Allison Bruce, Illah Nourbakhsh, and Reid Simmons. “The role of expressiveness and attention in human-robot interaction”. In: *Robotics and Automation, 2002. Proceedings. ICRA'02. IEEE International Conference on*. Vol. 4. IEEE. 2002, pp. 4138–4142.

[18] Terrence Fong, Illah Nourbakhsh, and Kerstin Dautenhahn. “A survey of socially interactive robots”. In: *Robotics and autonomous systems* 42.3-4 (2003), pp. 143–166.

[19] Takayuki Kanda et al. “Interactive robots as social partners and peer tutors for children: A field trial”. In: *Human-computer interaction* 19.1 (2004), pp. 61–84.

[20] Rachel Gockley Allison et al. “Designing robots for long-term social interaction”. In: (2005).

[21] Daniel J Ricks and Mark B Colton. “Trends and considerations in robot-assisted autism therapy”. In: *Robotics and Automation (ICRA), 2010 IEEE International Conference on*. IEEE. 2010, pp. 4354–4359.

[22] Paola Pennisi et al. “Autism and social robotics: A systematic review”. In: *Autism Research* 9.2 (2016), pp. 165–183.

[23] Adriana Tapus, Cristian Ţăpuş, and Maja J Matarić. “User—robot personality matching and assistive robot behavior adaptation for post-stroke rehabilitation therapy”. In: *Intelligent Service Robotics* 1.2 (2008), p. 169.

[24] Adriana Tapus and Maja J Mataric. “Socially Assistive Robots: The Link between Personality, Empathy, Physiological Signals, and Task Performance.” In: *AAAI spring symposium: emotion, personality, and social behavior*. 2008, pp. 133–140.

[25] Joshua J Diehl et al. “The clinical use of robots for individuals with autism spectrum disorders: A critical review”. In: *Research in autism spectrum disorders* 6.1 (2012), pp. 249–262.

[26] W Bradley Knox, Peter Stone, and Cynthia Breazeal. "Training a robot via human feedback: A case study". In: *International Conference on Social Robotics*. Springer. 2013, pp. 460–470.

[27] Victoria Groom et al. "Responses to robot social roles and social role framing". In: *Collaboration Technologies and Systems (CTS), 2011 International Conference on*. IEEE. 2011, pp. 194–203.

[28] Juan Fasola and Maja Mataric. "A socially assistive robot exercise coach for the elderly". In: *Journal of Human-Robot Interaction* 2.2 (2013), pp. 3–32.

[29] Hillary Abraham et al. "Autonomous vehicles, trust, and driving alternatives: A survey of consumer preferences". In: *Transportation Research Board 96th Annual Meeting, Washington, DC*. 2017, pp. 8–12.

[30] Mica R Endsley. "Autonomous driving systems: A preliminary naturalistic study of the Tesla model S". In: *Journal of Cognitive Engineering and Decision Making* 11.3 (2017), pp. 225–238.

[31] Sebastian Hergeth et al. "Keep your scanners peeled: Gaze behavior as a measure of automation trust during highly automated driving". In: *Human factors* 58.3 (2016), pp. 509–519.

[32] Mica R Endsley. "From here to autonomy: lessons learned from human–automation research". In: *Human factors* 59.1 (2017), pp. 5–27.

[33] US Air Force. "Autonomous horizons". In: *Washington, DC: US Air Force Office of the Chief Scientist* (2015).

[34] Joelle Pineau et al. "Towards robotic assistants in nursing homes: Challenges and results". In: *Robotics and autonomous systems* 42.3-4 (2003), pp. 271–281.

[35] William Bluethmann et al. "Robonaut: A robot designed to work with humans in space". In: *Autonomous robots* 14.2-3 (2003), pp. 179–197.

[36] Rachid Alami et al. "Safe and dependable physical human-robot interaction in anthropic domains: State of the art and challenges". In: *Intelligent Robots and Systems, 2006 IEEE/RSJ International Conference on*. IEEE. 2006, pp. 1–16.

[37] Kerstin Dautenhahn et al. "How may I serve you?: a robot companion approaching a seated person in a helping context". In: *Proceedings of the 1st ACM SIGCHI/SIGART conference on Human-robot interaction*. ACM. 2006, pp. 172–179.

[38] Andrea Bauer, Dirk Wollherr, and Martin Buss. "Human–robot collaboration: a survey". In: *International Journal of Humanoid Robotics* 5.01 (2008), pp. 47–66.

[39] Arash Ajoudani, Nikos Tsagarakis, and Antonio Bicchi. "Tele-impedance: Teleoperation with impedance regulation using a body–machine interface". In: *The International Journal of Robotics Research* 31.13 (), pp. 1642–1656.

[40] Antal Haans and Wijnand A Ijsselsteijn. "Embodiment and telepresence: Toward a comprehensive theoretical framework". In: *Interacting with Computers* 24.4 (2012), pp. 211–218.

[41] Thomas B Sheridan. "Musings on telepresence and virtual presence". In: *Presence: Teleoperators & Virtual Environments* 1.1 (1992), pp. 120–126.

[42] Robert F Fogle. "The use of teleoperators in hostile environment applications". In: *Robotics and Automation, 1992. Proceedings., 1992 IEEE International Conference on*. IEEE. 1992, pp. 61–66.

[43] Karan A Manocha, Norali Pernalete, and Rajiv V Dubey. "Variable position mapping based assistance in teleoperation for nuclear cleanup". In: *Robotics and Automation, 2001. Proceedings 2001 ICRA. IEEE International Conference on*. Vol. 1. IEEE. 2001, pp. 374–379.

[44] W Randolph Chitwood and L Nifong. "Minimally Invasive Videloscopic Mitral Valve Surgery: The Current Role of Surgical Robotics". In: *Journal of cardiac surgery* 15.1 (2000), pp. 61–75.

[45] Xavier Lamy et al. "Achieving efficient and stable comanipulation through adaptation to changes in human arm impedance". In: *Robotics and Automation, 2009. ICRA'09. IEEE International Conference on*. IEEE. 2009, pp. 265–271.

[46] Allison M Okamura. "Methods for haptic feedback in teleoperated robot-assisted surgery". In: *Industrial Robot: An International Journal* 31.6 (2004), pp. 499–508.

[47] Allison M Okamura. "Haptic feedback in robot-assisted minimally invasive surgery". In: *Current opinion in urology* 19.1 (2009), p. 102.

[48] EC Lee et al. "Ergonomics and human factors in endoscopic surgery: a comparison of manual vs telerobotic simulation systems". In: *Surgical endoscopy and other interventional techniques* 19.8 (2005), pp. 1064–1070.

[49] Elise H Lawson et al. "Postural ergonomics during robotic and laparoscopic gastric bypass surgery: a pilot project". In: *Journal of robotic surgery* 1.1 (2007), pp. 61–67.

[50] Laura Santos-Carreras et al. "Survey on surgical instrument handle design: ergonomics and acceptance". In: *Surgical innovation* 19.1 (2012), pp. 50–59.

[51] Thomas B Sheridan. "Eight ultimate challenges of human-robot communication". In: *Robot and Human Communication, 1997. RO-MAN'97. Proceedings., 6th IEEE International Workshop on*. IEEE. 1997, pp. 9–14.

[52] Peter Ford Dominey, Anthony Mallet, and Eiichi Yoshida. "Real-time cooperative behavior acquisition by a humanoid apprentice". In: *Humanoid Robots, 2007 7th IEEE-RAS International Conference on*. IEEE. 2007, pp. 270–275.

[53] Peter Ford Dominey and Felix Warneken. “The basis of shared intentions in human and robot cognition”. In: *New Ideas in Psychology* 29.3 (2011), pp. 260–274.

[54] Stephane Lallée et al. “Towards a platform-independent cooperative human-robot interaction system: Ii. perception, execution and imitation of goal directed actions”. In: *Intelligent Robots and Systems (IROS), 2011 IEEE/RSJ International Conference on*. IEEE. 2011, pp. 2895–2902.

[55] MM Sobhani et al. “Towards model-based robot behaviour adaptation: Successful human-robot collaboration in tense and stressful situations”. In: *Electrical Engineering (ICEE), 2015 23rd Iranian Conference on*. IEEE. 2015, pp. 922–927.

[56] Peter Ford Dominey et al. “Anticipation and initiative in human-humanoid interaction”. In: *Humanoid Robots, 2008. Humanoids 2008. 8th IEEE-RAS International Conference on*. IEEE. 2008, pp. 693–699.

[57] Kai Nickel and Rainer Stiefelhagen. “Visual recognition of pointing gestures for human–robot interaction”. In: *Image and Vision Computing* 25.12 (2007), pp. 1875–1884.

[58] Stefan Waldherr, Roseli Romero, and Sebastian Thrun. “A gesture based interface for human-robot interaction”. In: *Autonomous Robots* 9.2 (2000), pp. 151–173.

[59] Stéphane Lallée et al. “Cooperative human robot interaction systems: IV. Communication of shared plans with Naïve humans using gaze and speech”. In: *Intelligent Robots and Systems (IROS), 2013 IEEE/RSJ International Conference on*. IEEE. 2013, pp. 129–136.

[60] Zhe Li et al. “Hierarchical modeling and recognition of manipulative gesture”. In: *Proc. of the Workshop on Modeling People and Human Interaction at the IEEE Int. Conf. on Computer Vision*. Vol. 77. 2005.

[61] Ali Ghadirzadeh et al. “A sensorimotor reinforcement learning framework for physical human-robot interaction”. In: *Intelligent Robots and Systems (IROS), 2016 IEEE/RSJ International Conference on*. IEEE. 2016, pp. 2682–2688.

[62] Serena Ivaldi et al. “Object learning through active exploration”. In: *IEEE Transactions on Autonomous Mental Development* 6.1 (2014), pp. 56–72.

[63] Tom Williams et al. “Is robot telepathy acceptable? Investigating effects of nonverbal robot-robot communication on human-robot interaction”. In: *Robot and Human Interactive Communication, 2014 RO-MAN: The 23rd IEEE International Symposium on*. IEEE. 2014, pp. 886–891.

[64] Kazuhiro Kosuge and Norihide Kazamura. “Control of a robot handling an object in cooperation with a human”. In: *Robot and Human Communication, 1997. RO-MAN’97. Proceedings., 6th IEEE International Workshop on*. IEEE. 1997, pp. 142–147.

[65] Jörg Krüger, Terje K Lien, and Alexander Verl. “Cooperation of human and machines in assembly lines”. In: *CIRP Annals-Manufacturing Technology* 58.2 (2009), pp. 628–646.

[66] Jens Hölldampf, Angelika Peer, and Martin Buss. “Synthesis of an interactive haptic dancing partner”. In: *RO-MAN, 2010 IEEE*. IEEE. 2010, pp. 527–532.

[67] Diego Felipe Paez Granados et al. “Guiding human motions in physical human-robot interaction through COM motion control of a dance teaching robot”. In: *Humanoid Robots (Humanoids), 2016 IEEE-RAS 16th International Conference on*. IEEE. 2016, pp. 279–285.

[68] Cynthia Breazeal et al. “Effects of nonverbal communication on efficiency and robustness in human-robot teamwork”. In: *Intelligent Robots and Systems, 2005.(IROS 2005). 2005 IEEE/RSJ International Conference on*. IEEE. 2005, pp. 708–713.

[69] John V Draper and Linda M Blair. “Workload, flow, and telepresence during teleoperation”. In: *Robotics and Automation, 1996. Proceedings., 1996 IEEE International Conference on*. Vol. 2. IEEE. 1996, pp. 1030–1035.

[70] David B Kaber, Emrah Onal, and Mica R Endsley. “Design of automation for telerobots and the effect on performance, operator situation awareness, and subjective workload”. In: *Human Factors and Ergonomics in Manufacturing* 10.4 (2000), pp. 409–430.

[71] Ilaria Strazzulla et al. “Online bimanual manipulation using surface electromyography and incremental learning”. In: *IEEE Transactions on Neural Systems and Rehabilitation Engineering* 25.3 (2017), pp. 227–234.

[72] Luka Peternel et al. “Adaptation of robot physical behaviour to human fatigue in human-robot co-manipulation”. In: *Humanoid Robots (Humanoids), 2016 IEEE-RAS 16th International Conference on*. IEEE. 2016, pp. 489–494.

[73] Christian Fleischer and Günter Hommel. “A human–exoskeleton interface utilizing electromyography”. In: *IEEE Transactions on Robotics* 24.4 (2008), pp. 872–882.

[74] Osamu Fukuda et al. “A human-assisting manipulator teleoperated by EMG signals and arm motions”. In: *IEEE Transactions on Robotics and Automation* 19.2 (2003), pp. 210–222.

[75] Duk Shin, Jaehyo Kim, and Yasuharu Koike. “A myokinetic arm model for estimating joint torque and stiffness from EMG signals during maintained posture”. In: *Journal of neurophysiology* 101.1 (2009), pp. 387–401.

[76] Arash Ajoudani et al. “A reduced-complexity description of arm endpoint stiffness with applications to teleimpedance control”. In: *Intelligent Robots and Systems (IROS), 2015 IEEE/RSJ International Conference on*. IEEE. 2015, pp. 1017–1023.

[77] Marc H Raibert and John J Craig. “Hybrid position/force control of manipulators”. In: *Journal of Dynamic Systems, Measurement, and Control* 103.2 (1981), pp. 126–133.

[78] Christian Ott, Ranjan Mukherjee, and Yoshihiko Nakamura. “Unified impedance and admittance control”. In: *Robotics and Automation (ICRA), 2010 IEEE International Conference on*. IEEE. 2010, pp. 554–561.

[79] Neville Hogan. “Impedance control: An approach to manipulation”. In: *American Control Conference, 1984*. IEEE. 1984, pp. 304–313.

[80] Neville Hogan. “Stable execution of contact tasks using impedance control”. In: *Robotics and Automation. Proceedings. 1987 IEEE International Conference on*. Vol. 4. IEEE. 1987, pp. 1047–1054.

[81] Gill A Pratt and Matthew M Williamson. “Series elastic actuators”. In: *Intelligent Robots and Systems 95.'Human Robot Interaction and Cooperative Robots', Proceedings. 1995 IEEE/RSJ International Conference on*. Vol. 1. IEEE. 1995, pp. 399–406.

[82] Eric J Perreault, Robert F Kirsch, and Patrick E Crago. “Voluntary control of static endpoint stiffness during force regulation tasks”. In: *Journal of neurophysiology* 87.6 (2002), pp. 2808–2816.

[83] Daniel Liberzon and A Stephen Morse. “Basic problems in stability and design of switched systems”. In: *IEEE Control systems* 19.5 (1999), pp. 59–70.

[84] Dale A Lawrence. “Stability and transparency in bilateral teleoperation”. In: *IEEE transactions on robotics and automation* 9.5 (1993), pp. 624–637.

[85] Lonnie J Love and Wayne J Book. “Force reflecting teleoperation with adaptive impedance control”. In: *IEEE Transactions on Systems, Man, and Cybernetics, Part B (Cybernetics)* 34.1 (2004), pp. 159–165.

[86] Arash Ajoudani. *Transferring human impedance regulation skills to robots*. Vol. 110. Springer, 2016.

[87] Luka Peternel and Arash Ajoudani. “Robots learning from robots: A proof of concept study for co-manipulation tasks”. In: *Humanoid Robotics (Humanoids), 2017 IEEE-RAS 17th International Conference on*. IEEE. 2017, pp. 484–490.

[88] A Albu-Schaffer et al. “Soft robotics: what cartesian stiffness can obtain with passively compliant, uncoupled joints?” In: *Intelligent Robots and Systems, 2004.(IROS 2004). Proceedings. 2004 IEEE/RSJ International Conference on*. Vol. 4. IEEE. 2004, pp. 3295–3301.

[89] William Owen, Elizabeth Croft, and Beno Benhabib. “Stiffness optimization for two-armed robotic sculpting”. In: *Industrial Robot: An International Journal* 35.1 (2008), pp. 46–57.

[90] Toru Tsumugiwa, Ryuichi Yokogawa, and Kei Hara. “Variable impedance control based on estimation of human arm stiffness for human-robot cooperative calligraphic task”. In: *Robotics and Automation, 2002. Proceedings. ICRA'02. IEEE International Conference on*. Vol. 1. IEEE. 2002, pp. 644–650.

[91] Vincent Duchaine and Clément Gosselin. “Safe, stable and intuitive control for physical human-robot interaction”. In: *Robotics and Automation, 2009. ICRA'09. IEEE International Conference on*. IEEE. 2009, pp. 3383–3388.

[92] Nathanaël Jarrassé et al. “How can human motion prediction increase transparency?” In: *Robotics and Automation, 2008. ICRA 2008. IEEE International Conference on*. IEEE. 2008, pp. 2134–2139.

[93] Elisa Beretta et al. “Adaptive hands-on control for reaching and targeting tasks in surgery”. In: *International Journal of Advanced Robotic Systems* 12.5 (2015), p. 50.

[94] Yen-Yi Juo et al. “Diffusion of robotic-assisted laparoscopic technology across specialties: a national study from 2008 to 2013”. In: *Surgical Endoscopy* (2017), pp. 1–9.

[95] Robert D Howe and Yoky Matsuoka. “Robotics for surgery”. In: *Annual Review of Biomedical Engineering* 1.1 (1999), pp. 211–240.

[96] Bijoy Johnson and G Somu. “Robotic Telesurgery: Benefits Beyond Barriers”. In: *BMH Medical Journal* 3.2 (2016).

[97] Nima Enayati, Giancarlo Ferrigno, and Elena De Momi. “Performance metrics for guidance active constraints in surgical robotics”. In: *The International Journal of Medical Robotics and Computer Assisted Surgery* 14.1 (2018).

[98] Tian Zhou et al. “A comparative study for telerobotic surgery using free hand gestures”. In: *Journal of Human-Robot Interaction* 5.2 (2016), pp. 1–28.

[99] Hairong Jiang, Bradley S Duerstock, and Juan P Wachs. “User-centered and analytic-based approaches to generate usable gestures for individuals with quadriplegia”. In: *IEEE Transactions on Human-Machine Systems* 46.3 (2016), pp. 460–466.

[100] E. Beretta et al. “Enhanced torque-based impedance control to assist brain targeting during open-skull neurosurgery: a feasibility study”. In: *The International Journal of Medical Robotics and Computer Assisted Surgery* 12.3 (2015), pp. 326–341. DOI: `10.1002/rcs.1690`.

[101] Ilana Nisky, Allison M Okamura, and Michael H Hsieh. “Effects of robotic manipulators on movements of novices and surgeons”. In: *Surgical endoscopy* 28.7 (2014), pp. 2145–2158.

[102] Nima Enayati, Elena De Momi, and Giancarlo Ferrigno. “Haptics in robot-assisted surgery: challenges and benefits”. In: *IEEE reviews in biomedical engineering* 9 (2016), pp. 49–65.

[103] Nima Enayati, Giancarlo Ferrigno, and Elena De Momi. “Skill-based human–robot cooperation in tele-operated path tracking”. In: *Autonomous Robots* (2017), pp. 1–13.

[104] Mark L Latash, John P Scholz, and Gregor Schöner. “Motor control strategies revealed in the structure of motor variability”. In: *Exercise and sport sciences reviews* 30.1 (2002), pp. 26–31.

[105] Jacopo Buzzi et al. “On the value of estimating human arm stiffness during virtual teleoperation with robotic manipulators”. In: *Frontiers in Neuroscience* 11 (2017), p. 528.

[106] Jacopo Buzzi et al. “Analysis of joint and hand impedance during teleoperation and free-hand task execution”. In: *IEEE Robotics and Automation Letters* 2.3 (2017), pp. 1733–1739.

[107] Mark L Latash. “The Bernstein problem: how does the central nervous system make its choices”. In: *Dexterity and its development* (1996), pp. 277–303.

[108] Maeda Kawato et al. “Trajectory formation of arm movement by cascade neural network model based on minimum torque-change criterion”. In: *Biological cybernetics* 62.4 (1990), pp. 275–288.

[109] Paolo Viviani and Tamar Flash. “Minimum-jerk, two-thirds power law, and isochrony: converging approaches to movement planning.” In: *Journal of Experimental Psychology: Human Perception and Performance* 21.1 (1995), p. 32.

[110] Boris I Prilutsky and Vladimir M Zatsiorsky. “Optimization-based models of muscle coordination”. In: *Exercise and sport sciences reviews* 30.1 (2002), p. 32.

[111] Olaf Sporns and Gerald M Edelman. “Solving Bernstein’s problem: A proposal for the development of coordinated movement by selection”. In: *Child development* 64.4 (1993), pp. 960–981.

[112] Emanuel Todorov. “Interpreting motor adaptation results within the framework of optimal feedback control”. In: *Advances in Computational Motor Control* 1 (2002).

[113] Emanuel Todorov and Michael I Jordan. “Optimal feedback control as a theory of motor coordination”. In: *Nature neuroscience* 5.11 (2002), p. 1226.

[114] Israel M Gelfand and Mark L Latash. “On the problem of adequate language in motor control”. In: *Motor control* 2.4 (1998), pp. 306–313.

[115] Mark L Latash. “The bliss (not the problem) of motor abundance (not redundancy)”. In: *Experimental brain research* 217.1 (2012), pp. 1–5.

[116] Hermann Müller and Dagmar Sternad. “Decomposition of variability in the execution of goal-oriented tasks: three components of skill improvement.” In: *Journal of Experimental Psychology: Human Perception and Performance* 30.1 (2004), p. 212.

[117] Joseph P Cusumano and Paola Cesari. “Body-goal variability mapping in an aiming task”. In: *Biological cybernetics* 94.5 (2006), pp. 367–379.

[118] Jonathan B Dingwell, Rachel F Smallwood, and Joseph P Cusumano. “Trial-to-trial dynamics and learning in a generalized, redundant reaching task”. In: *Journal of Neurophysiology* 109.1 (2013), pp. 225–237.

[119] Jeng-Feng Yang, John P Scholz, and Mark L Latash. “The role of kinematic redundancy in adaptation of reaching”. In: *Experimental brain research* 176.1 (2007), pp. 54–69.

[120] Francisco J Valero-Cuevas, Madhusudhan Venkadesan, and Emanuel Todorov. “Structured variability of muscle activations supports the minimal intervention principle of motor control”. In: *Journal of neurophysiology* 102.1 (2009), pp. 59–68.

[121] Dagmar Sternad et al. “Coordinate dependence of variability analysis”. In: *PLoS computational biology* 6.4 (2010), e1000751.

[122] Domenico Campolo et al. “Analysis of accuracy in pointing with redundant hand-held tools: a geometric approach to the uncontrolled manifold method”. In: *PLoS computational biology* 9.4 (2013), e1002978.

[123] Dmitry Domkin et al. “Structure of joint variability in bimanual pointing tasks”. In: *Experimental brain research* 143.1 (2002), pp. 11–23.

[124] Robert Rein, Blandine Bril, and Tetsushi Nonaka. “Coordination strategies used in stone knapping”. In: *American Journal of Physical Anthropology* 150.4 (2013), pp. 539–550.

[125] Mark L Latash et al. “Structure of motor variability in marginally redundant multifinger force production tasks”. In: *Experimental brain research* 141.2 (2001), pp. 153–165.

[126] Ilana Nisky, Michael H Hsieh, and Allison M Okamura. “Uncontrolled manifold analysis of arm joint angle variability during robotic teleoperation and freehand movement of surgeons and novices”. In: *IEEE Transactions on Biomedical Engineering* 61.12 (2014), pp. 2869–2881.

[127] Ilana Nisky et al. “Teleoperated versus open needle driving: Kinematic analysis of experienced surgeons and novice users”. In: *Robotics and Automation (ICRA), 2015 IEEE International Conference on*. IEEE. 2015, pp. 5371–5377.

[128] Y Sharon, T Lendvay, and I Nisky. “Instrument tip angular kinematics in teleoperated needle-driving”. In: *Proc. Hamlyn Symposium on Medical Robotics*. 2016, pp. 96–97.

[129] Yarden Sharon, Thomas Sean Lendvay, and Ilana Nisky. “Instrument Orientation-Based Metrics for Surgical Skill Evaluation in Robot-Assisted and Open Needle Driving”. In: *arXiv preprint arXiv:1709.09452* (2017).

[130] John P Scholz, Gregor Schöner, and Mark L Latash. "Identifying the control structure of multijoint coordination during pistol shooting". In: *Experimental Brain Research* 135.3 (2000), pp. 382–404. ISSN: 1432-1106. DOI: `10.1007/s002210000540`.

[131] A Morrison, D McGrath, and E S Wallace. "Motor abundance and control structure in the golf swing". In: *Human movement science* 46 (2016), pp. 129–147.

[132] T Flash and F Mussa-Ivaldi. "Human arm stiffness characteristics during the maintenance of posture". In: *Experimental Brain Research* 82.2 (1990), pp. 315–326.

[133] Yoichi Iino, Shinsuke Yoshioka, and Senshi Fukashiro. "Uncontrolled manifold analysis of joint angle variability during table tennis forehand". In: *Human movement science* 56 (2017), pp. 98–108.

[134] Nava Levit-Binnun, Edna Schechtman, and Tamar Flash. "On the similarities between the perception and production of elliptical trajectories". In: *Experimental brain research* 172.4 (2006), pp. 533–555.

[135] Radu Horaud and Fadi Dornaika. "Hand-eye calibration". In: *The international journal of Robotics Research* 14.3 (1995), pp. 195–210.

[136] R A Prokopenko et al. "Assessment of the accuracy of a human arm model with seven degrees of freedom". In: *Journal of biomechanics* 34.2 (2001), pp. 177–185.

[137] Katherine R Saul et al. "Benchmarking of dynamic simulation predictions in two software platforms using an upper limb musculoskeletal model". In: *Computer methods in biomechanics and biomedical engineering* 18.13 (2015), pp. 1445–1458.

[138] Katherine R S Holzbaur, Wendy M Murray, and Scott L Delp. "A model of the upper extremity for simulating musculoskeletal surgery and analyzing neuromuscular control". In: *Annals of biomedical engineering* 33.6 (2005), pp. 829–840.

[139] Scott L Delp et al. "OpenSim: open-source software to create and analyze dynamic simulations of movement". In: *IEEE Transactions on Biomedical Engineering* 54.11 (2007), pp. 1940–1950.

[140] John P Scholz and Gregor Schöner. "The uncontrolled manifold concept: identifying control variables for a functional task". In: *Experimental brain research* 126.3 (1999), pp. 289–306.

[141] Mark L Latash, John P Scholz, and Gregor Schöner. "Toward a new theory of motor synergies". In: *Motor control* 11.3 (2007), pp. 276–308.

[142] Sandra Maria Sbeghen Ferreira de Freitas and John Peter Scholz. "A comparison of methods for identifying the Jacobian for uncontrolled manifold variance analysis". In: *Journal of biomechanics* 43.4 (2010), pp. 775–777.

[143] Bert Steenbergen, Ronald G Marteniuk, and Linda E Kalbfleisch. "Achieving coordination in prehension: joint freezing and postural contributions". In: *Journal of motor behavior* 27.4 (1995), pp. 333–348.

[144] Michel Desmurget et al. "Constrained and unconstrained movements involve different control strategies". In: *Journal of neurophysiology* 77.3 (1997), pp. 1644–1650.

[145] Mark H Anshel, Robert Weinberg, and Allen Jackson. "The effect of goal difficulty and task complexity on intrinsic motivation and motor performance". In: *Journal of Sport Behavior* 15.2 (1992), p. 159.

[146] Marios Goudas, Kalliopi Minardou, and Ioannis Kotis. "Feedback regarding goal achievement and intrinsic motivation". In: *Perceptual and Motor Skills* 90.3 (2000), pp. 810–812.

[147] Gary P Latham, Edwin A Locke, and Neil E Fassina. "The high performance cycle: Standing the test of time". In: *Psychological management of individual performance* (2002), pp. 201–228.

[148] Valentine Roux, Blandine Bril, and Gilles Dietrich. "Skills and learning difficulties involved in stone knapping: The case of stone-bead knapping in Khambhat, India". In: *World Archaeology* 27.1 (1995), pp. 63–87.

[149] Julius Verrel et al. "Coordination of degrees of freedom and stabilization of task variables in a complex motor skill: expertise-related differences in cello bowing". In: *Experimental brain research* 224.3 (2013), pp. 323–334.

[150] Paul Glazier. "Movement variability in the golf swing: Theoretical, methodological, and practical issues". In: *Research quarterly for exercise and sport* 82.2 (2011), pp. 157–161.

[151] Mark A Fehlberg et al. "Improved active handrest performance through use of virtual fixtures". In: *IEEE Transactions on Human-Machine Systems* 44.4 (2014), pp. 484–498.

[152] Frank C Park. "Distance metrics on the rigid-body motions with applications to mechanism design". In: *Journal of Mechanical Design* 117.1 (1995), pp. 48–54.

[153] Darcy S Reisman, John P Scholz, and Gregor Schöner. "Differential joint coordination in the tasks of standing up and sitting down". In: *Journal of Electromyography and Kinesiology* 12.6 (2002), pp. 493–505.

[154] Tim Bennett, Chris Low, and Carlton Cooke. "INSTEP SOCCER KICK TECHNIQUE AND PERFORMANCE THROUGH AN ANALYSIS OF MOVEMENT VARlABILlN". In: *ISBS-Conference Proceedings Archive*. Vol. 34. 1. 2016.

[155] MA Talamini et al. "A prospective analysis of 211 robotic-assisted surgical procedures". In: *Surgical Endoscopy and Other Interventional Techniques* 17.10 (2003), pp. 1521–1524.

[156] Ruaidhri McVey et al. "Baseline laparoscopic skill may predict baseline robotic skill and early robotic surgery learning curve". In: *Journal of Endourology* 30.5 (2016), pp. 588–592.

[157] Sanjeev Kaul, Nikhil L Shah, and Mani Menon. "Learning curve using robotic surgery". In: *Current urology reports* 7.2 (2006), pp. 125–129.

[158] JD Hernandez et al. "Qualitative and quantitative analysis of the learning curve of a simulated surgical task on the da Vinci system". In: *Surgical Endoscopy And Other Interventional Techniques* 18.3 (2004), pp. 372–378.

[159] Garth H Ballantyne and Fred Moll. "The da Vinci telerobotic surgical system: the virtual operative field and telepresence surgery". In: *Surgical Clinics of North America* 83.6 (2003), pp. 1293–1304.

[160] Nima Enayati, Elena De Momi, and Giancarlo Ferrigno. "Haptics in Robot-Assisted Surgery: Challenges and Benefits". In: (2016).

[161] Elisa Beretta et al. "Force feedback enhancement for soft tissue interaction tasks in cooperative robotic surgery". In: *Intelligent Robots and Systems (IROS), 2015 IEEE/RSJ International Conference on*. IEEE. 2015, pp. 209–215.

[162] Tobias Ortmaier et al. "Robot assisted force feedback surgery". In: *Advances in telerobotics*. Springer, 2007, pp. 361–379.

[163] Nima Enayati et al. "A dynamic non-energy-storing guidance constraint with motion redirection for robot-assisted surgery". In: *Intelligent Robots and Systems (IROS), 2016 IEEE/RSJ International Conference on*. IEEE. 2016, pp. 4311–4316.

[164] Roland Sigrist et al. "Augmented visual, auditory, haptic, and multimodal feedback in motor learning: a review". In: *Psychonomic bulletin & review* 20.1 (2013), pp. 21–53.

[165] Ilana Nisky, Michael H Hsieh, and Allison M Okamura. "The effect of a robot-assisted surgical system on the kinematics of user movements". In: *2013 35th Annual International Conference of the IEEE Engineering in Medicine and Biology Society (EMBC)* (2013), pp. 6257–6260.

[166] Ferdinando A Mussa-Ivaldi, Neville Hogan, and Emilio Bizzi. "Neural, mechanical, and geometric factors subserving arm posture in humans". In: *The Journal of neuroscience* 5.10 (1985), pp. 2732–2743.

[167] E Burdet et al. "A method for measuring endpoint stiffness during multi-joint arm movements". In: *Journal of biomechanics* 33.12 (2000), pp. 1705–1709.

[168] Paul L Gribble et al. "Role of cocontraction in arm movement accuracy". In: *Journal of neurophysiology* 89.5 (2003), pp. 2396–2405.

[169] Bjarne Laursen, Bente Rona Jensen, and G Sjøgaard. "Effect of speed and precision demands on human shoulder muscle electromyography during a repetitive task". In: *European Journal of Applied Physiology and Occupational Physiology* 78.6 (1998), pp. 544–548.

[170] David W Franklin et al. "Adaptation to stable and unstable dynamics achieved by combined impedance control and inverse dynamics model". In: *Journal of neurophysiology* 90.5 (2003), pp. 3270–3282.

[171] Mohammad Darainy et al. "Learning to control arm stiffness under static conditions". In: *Journal of neurophysiology* 92.6 (2004), pp. 3344–3350.

[172] Hiroaki Gomi and Mitsuo Kawato. "Human arm stiffness and equilibrium-point trajectory during multi-joint movement". In: *Biological cybernetics* 76.3 (1997), pp. 163–171.

[173] Morgan Quigley et al. "ROS: an open-source Robot Operating System". In: *ICRA workshop on open source software*. Vol. 3. 3.2. Kobe. 2009, p. 5.

[174] J McIntyre, F A Mussa-Ivaldi, and E Bizzi. "The control of stable postures in the multijoint arm". In: *Experimental brain research* 110.2 (1996), pp. 248–264.

[175] Cheng Fang et al. "Online Model Based Estimation of Complete Joint Stiffness of Human Arm". In: *IEEE Robotics and Automation Letters* 3.1 (2018), pp. 84–91.

[176] C Bradford Barber, David P Dobkin, and Hannu Huhdanpaa. "The quickhull algorithm for convex hulls". In: *ACM Transactions on Mathematical Software (TOMS)* 22.4 (1996), pp. 469–483.

[177] Liam Cragg and Huosheng Hu. "Application of mobile agents to robust teleoperation of internet robots in nuclear decommissioning". In: *Industrial Technology, 2003 IEEE International Conference on*. Vol. 2. IEEE. 2003, pp. 1214–1219.

[178] Nikos C Mitsou, Spyros V Velanas, and Costas S Tzafestas. "Visuo-haptic interface for teleoperation of mobile robot exploration tasks". In: *ROMAN 2006-The 15th IEEE International Symposium on Robot and Human Interactive Communication*. IEEE. 2006, pp. 157–163.

[179] Patrick Fischer, Ron Daniel, and K V Siva. "Specification and design of input devices for teleoperation". In: *Robotics and Automation, 1990. Proceedings., 1990 IEEE International Conference on*. IEEE. 1990, pp. 540–545.

[180] François Conti, Jaeheung Park, and Oussama Khatib. "Interface design and control strategies for a robot assisted ultrasonic examination system". In: *Experimental Robotics*. Springer. 2014, pp. 97–113.

[181] J E Colgate. "Coupled stability of multiport systems—Theory and experiments". In: *Journal of dynamic systems, measurement, and control* 116.3 (1994), pp. 419–428.

[182] Dongjun Lee and Mark W Spong. "Passive bilateral teleoperation with constant time delay". In: *IEEE Transactions on Robotics* 22.2 (2006), pp. 269–281.

[183] Etienne Burdet et al. "The central nervous system stabilizes unstable dynamics by learning optimal impedance". In: *Nature* 414.6862 (2001), pp. 446–449.

[184] Rieko Osu et al. "Short-and long-term changes in joint co-contraction associated with motor learning as revealed from surface EMG". In: *Journal of Neurophysiology* 88.2 (2002), pp. 991–1004.

[185] Paul L Gribble et al. "Role of cocontraction in arm movement accuracy". In: *Journal of Neurophysiology* 89.5 (2003), pp. 2396–2405.

[186] Tian Qiu, William R Hamel, and Dongjun Lee. "Design and control of a low cost 6 DOF master controller". In: *2014 IEEE International Conference on Robotics and Automation (ICRA)*. IEEE. 2014, pp. 5313–5318.

[187] Mostafa Hadavand et al. "A novel remote center of motion mechanism for the force-reflective master robot of haptic tele-surgery systems". In: *The International Journal of Medical Robotics and Computer Assisted Surgery* 10.2 (2014), pp. 129–139.

[188] Steven F Wiker, Elaine Hershkowitz, and John Zik. "Teleoperator comfort and psychometric stability: Criteria for limiting master-controller forces of operation and feedback during telemanipulation". In: *Proceeding of the NASA Conference on Space Telerobotics* 1 (1989), pp. 99–107.

[189] Davide Piovesan et al. "Experimental measure of arm stiffness during single reaching movements with a time-frequency analysis". In: *Journal of neurophysiology* 110.10 (2013), pp. 2484–2496.

[190] Claudio Pizzolato et al. "CEINMS: A toolbox to investigate the influence of different neural control solutions on the prediction of muscle excitation and joint moments during dynamic motor tasks". In: *Journal of Biomechanics* 48.14 (2015), pp. 3929–3936.

[191] Andreas Tobergte and Patrick Helmer. "A disturbance observer for the sigma. 7 haptic device". In: *Intelligent Robots and Systems (IROS), 2013 IEEE/RSJ International Conference on*. IEEE. 2013, pp. 4964–4969.

[192] Gregory J Lehman and Stuart M McGill. "The importance of normalization in the interpretation of surface electromyography: a proof of principle". In: *Journal of manipulative and physiological therapeutics* 22.7 (1999), pp. 444–446.

[193] David G Lloyd and Thor F Besier. "An EMG-driven musculoskeletal model to estimate muscle forces and knee joint moments in vivo". In: *Journal of biomechanics* 36.6 (2003), pp. 765–776.

[194] Massimo Sartori et al. "EMG-driven forward-dynamic estimation of muscle force and joint moment about multiple degrees of freedom in the human lower extremity". In: *PloS one* 7.12 (2012), e52618.

[195] Qi Shao et al. "An EMG-driven model to estimate muscle forces and joint moments in stroke patients". In: *Computers in biology and medicine* 39.12 (2009), pp. 1083–1088.

[196] Xiao Hu, Wendy M Murray, and Eric J Perreault. "Muscle short-range stiffness can be used to estimate the endpoint stiffness of the human arm". In: *Journal of neurophysiology* 105.4 (2011), pp. 1633–1641.

[197] Edwin B Wilson and Jane Worcester. "The normal logarithmic transform". In: *The Review of Economic Statistics* (1945), pp. 17–22.

[198] Matthew Dyck, Ali Jazayeri, and Mahdi Tavakoli. "Is the human operator in a teleoperation system passive?" In: *World Haptics Conference (WHC), 2013*. IEEE. 2013, pp. 683–688.

[199] Ahmad Rabie and Uwe Handmann. "Fusion of audio-and visual cues for real-life emotional human robot interaction". In: *Joint Pattern Recognition Symposium*. Springer. 2011, pp. 346–355.

[200] Viktor Richter et al. "Are you talking to me?: Improving the Robustness of Dialogue Systems in a Multi Party HRI Scenario by Incorporating Gaze Direction and Lip Movement of Attendees". In: *Proceedings of the Fourth International Conference on Human Agent Interaction*. ACM. 2016, pp. 43–50.

[201] Md Hasanuzzaman et al. "Adaptive visual gesture recognition for human–robot interaction using a knowledge-based software platform". In: *Robotics and Autonomous Systems* 55.8 (2007), pp. 643–657.

[202] Jonas Moll and Eva-Lotta Sallnäs. "Communicative functions of haptic feedback". In: *International Conference on Haptic and Audio Interaction Design*. Springer. 2009, pp. 1–10.

[203] Brenna D Argall and Aude G Billard. "A survey of tactile human–robot interactions". In: *Robotics and autonomous systems* 58.10 (2010), pp. 1159–1176.

[204] David Silvera-Tawil, David Rye, and Mari Velonaki. "Artificial skin and tactile sensing for socially interactive robots: A review". In: *Robotics and Autonomous Systems* 63 (2015), pp. 230–243.

[205] Agostino De Santis et al. "An atlas of physical human–robot interaction". In: *Mechanism and Machine Theory* 43.3 (2008), pp. 253–270.

[206] SM Mizanoor Rahman and Ryojun Ikeura. "Weight-prediction-based predictive optimal position and force controls of a power assist robotic system for object manipulation". In: *IEEE Transactions on Industrial Electronics* 63.9 (2016), pp. 5964–5975.

[207] Panagiota Tsarouchi et al. "On a human-robot collaboration in an assembly cell". In: *International Journal of Computer Integrated Manufacturing* 30.6 (2017), pp. 580–589.

[208] S Bai and S Christensen. "Biomechanical HRI Modeling and Mechatronic Design of Exoskeletons for Assistive Applications". In: *Human Modelling for Bio-Inspired Robotics*. Elsevier, 2016, pp. 251–272.

[209] Syamimi Shamsuddin. "Development of human-robot interaction (HRI) methodology for autism rehabilitation using humanoid robot with a telerehabilitation platform". PhD thesis. Universiti Teknologi MARA, 2015.

[210] George Adamides et al. "Usability guidelines for the design of robot teleoperation: A taxonomy". In: *IEEE Transactions on Human-Machine Systems* 45.2 (2015), pp. 256–262.

[211] AK Bejczy and B Hannaford. "Man-machine interaction in space telerobotics". In: *Proceedings of the International Symposium of Teleoperation and control*. Vol. 1988. 1988.

[212] TW Burgess et al. "Operational experience and design recommendations for teleoperated flight hardware". In: (1988).

[213] Jacopo Buzzi, Elena De Momi, and Ilana Nisky. "An uncontrolled manifold analysis of arm joint variability in virtual planar position and orientation telemanipulation". In: *Transaction on Biomedical Engineering* (Under Review).

[214] Stefano Chiaverini and Lorenzo Sciavicco. "The parallel approach to force/-position control of robotic manipulators". In: *IEEE Transactions on Robotics and Automation* 9.4 (1993), pp. 361–373.

[215] Bo Huang et al. "Coordination control of a dual-arm exoskeleton robot using human impedance transfer skills". In: *IEEE Transactions on Systems, Man, and Cybernetics: Systems* (2017).

[216] Morgan Quigley et al. "ROS: an open-source Robot Operating System". In: *ICRA workshop on open source software*. Vol. 3. 3.2. Kobe, Japan. 2009, p. 5.

[217] Katherine RS Holzbaur, Wendy M Murray, and Scott L Delp. "A model of the upper extremity for simulating musculoskeletal surgery and analyzing neuromuscular control". In: *Annals of biomedical engineering* 33.6 (2005), pp. 829–840.

[218] Ferdinando A Mussa-Ivaldi, Neville Hogan, and Emilio Bizzi. "Neural, mechanical, and geometric factors subserving arm posture in humans". In: *Journal of Neuroscience* 5.10 (1985), pp. 2732–2743.

[219] John M Dolan, Mark B Friedman, and Mark L Nagurka. "Dynamic and loaded impedance components in the maintenance of human arm posture". In: *IEEE Transactions on Systems, Man, and Cybernetics* 23.3 (1993), pp. 698–709.

[220] Aaron M Dollar and Hugh Herr. "Lower extremity exoskeletons and active orthoses: challenges and state-of-the-art". In: *IEEE Transactions on robotics* 24.1 (2008), pp. 144–158.

[221] Michael Windrich et al. “Active lower limb prosthetics: a systematic review of design issues and solutions”. In: *Biomedical engineering online* 15.3 (2016), p. 140.

[222] Alex Smith et al. “Bimanual robotic manipulation with biomimetic joint/-task space hybrid adaptation of force and impedance”. In: *The Proceedings of the 11th IEEE International Conference on Control and Automation to be held in Taichung, Taiwan, June*. 2014, pp. 18–20.

[223] Robert D Gregg and Jonathon W Sensinger. “Towards biomimetic virtual constraint control of a powered prosthetic leg”. In: *IEEE Transactions on Control Systems Technology* 22.1 (2014), pp. 246–254.

[224] Yi Ren et al. “Biomimetic object impedance control for dual-arm cooperative 7-DOF manipulators”. In: *Robotics and Autonomous Systems* 75 (2016), pp. 273–287.

List of Publications

[1] Christian Di Natali et al. "Closed-loop control of local magnetic actuation for robotic surgical instruments". In: *IEEE Transactions on Robotics* 31.1 (2015), pp. 143–156.

[2] Nicolò Garbin et al. "Laparoscopic tissue retractor based on local magnetic actuation". In: *Journal of Medical Devices* 9.1 (2015), p. 011005.

[3] Jacopo Buzzi et al. "Analysis of joint and hand impedance during teleoperation and free-hand task execution". In: *IEEE Robotics and Automation Letters* 2.3 (2017), pp. 1733–1739.

[4] Jacopo Buzzi et al. "On the value of estimating human arm stiffness during virtual teleoperation with robotic manipulators". In: *Frontiers in Neuroscience* 11 (2017), p. 528.

[5] Jacopo Buzzi, Elena De Momi, and Ilana Nisky. "An uncontrolled manifold analysis of arm joint variability in virtual planar position and orientation telemanipulation". In: *Transaction on Biomedical Engineering - Under Second Review* (2018).

[6] Jacopo Buzzi et al. "Biomimetic adaptive impedance control in physical Human Robot Interaction". In: *2018 IEEE International Conference on Biomedical Robotics and Biomechatronics (BioRob) - Under Review*. IEEE. 2018.